Paper-11

Study of Thermal Analytical Characteristics of *Gymnema sylvestre* plant by TGA-DTA technique

Nirmala Kakade[1]*, Shobha Rupanar[2], Rituja Satpute[3]

[1,3]Dadapatil Rajale Art's, Science and Commerce College Adinathnagar, Pathardi, Maharashtra, India

[2]Baburaoji Gholap College, New Sangavi, Maharashtra, India,

ABSTRACT:

A well-known antidiabetic *Gymnema sylvestre* is one of the medicinal plants, whose therapeutic value has been studied in different systems of traditional medication. The plant used for the management of different disease and ailments of human beings. In modern system of herbal medicine, drug standardization is essential in order to assess quality and purity of herbal drug. TGA-DTA thermal analysis technique has employed in order to study physical and chemical changes of various herbal drugs. In this study thermal chemical characteristics of powdered leaves, stem and root of *G. sylvestre* were studied by using TGA-DTA techniques. TGA and DTA curves were taken from the range 35^0C to 700 ^{0}C and shows decomposition pattern of *G. sylvestre* plant material. In DTA curve, Endothermic peak in all samples at 101 °C is due to water loss from surface and pores of the powder. Second weight loss between 350-400 °C is associated to degradation of cellulose and hemicellulose present in plant. In further analysis there is possibility of degradation of lignin between 450-700 °C by further extending the analysis temperature. TGA analysis of powdered leaves, stem and root of provides information about stability and composition of medicinal plant *G. sylvestre*. The result of analysis gives supportive information which can be used for identification and standardization of *G. sylvestre* medicinal plant in herbal drug analysis.

Keywords: Thermal (TGA-DTA) analysis, *Gymnema sylvestre* leaves, stem and root.

INTRODUCTION:

Gymnema sylvestre Wild R.Br belongs to family Apocynaceae (Subfamily: Asclepiadaceae), an herbal Indian medicinal plant used in traditional medicine to treat diabetes[1]. In ancient times, Gymnema was known as '*Gurmar*', which literally means sugar killer. This plant is used by India healers for nearly 2000 years as part of the Ayurvedic traditional system[2].

TGA-DTA analysis is important technique mainly used in standardization of herbal drug in Phytochemistry[3]. Thermal analysis gives qualitative and quantitative information of volatile and non-volatile compounds present in plant material. The overall composition and Thermal stability of plant can also be determined by TGA-DTA technique[4,5]. Recent research articles shows that apart from leaves, stem and root of *G. sylvestre* has medicinally importance and can be used as herbal drug [6,7].

MATERIALS AND METHODS:

Collection and Authentication of plant material: *Gymnema Sylvestre* plant material (5 Kg) was collected from Mulashi, Pune in bulk for research study. The plant was authenticated by Botanical Survey of India, Pune (BSI). The material has been deposited at AHMA herbarium at BSI (Voucher No.SVS-1/783).

Preparation of Sample for TGA-DTA analysis: The leaves, stem & root of *G. sylvestre* were separated and washed thoroughly in water to remove soil, foreign particles and all other contamination adhered to surface. The plant materials are allowed to dry at room temperature. The air-dried plant materials were cut into small pieces and ground into fine powder using grinder. Each plant part powdered sample was sieved through a 0.5 mm diameter sieve. All the three samples are stored in air tight container and used for further analysis as shown in Fig. 1. The sample has to be weighted before the analysis and then placed in TGA device and start to run the experiment.7.0 mg of each powdered sample was used for TGA-DTA studies.

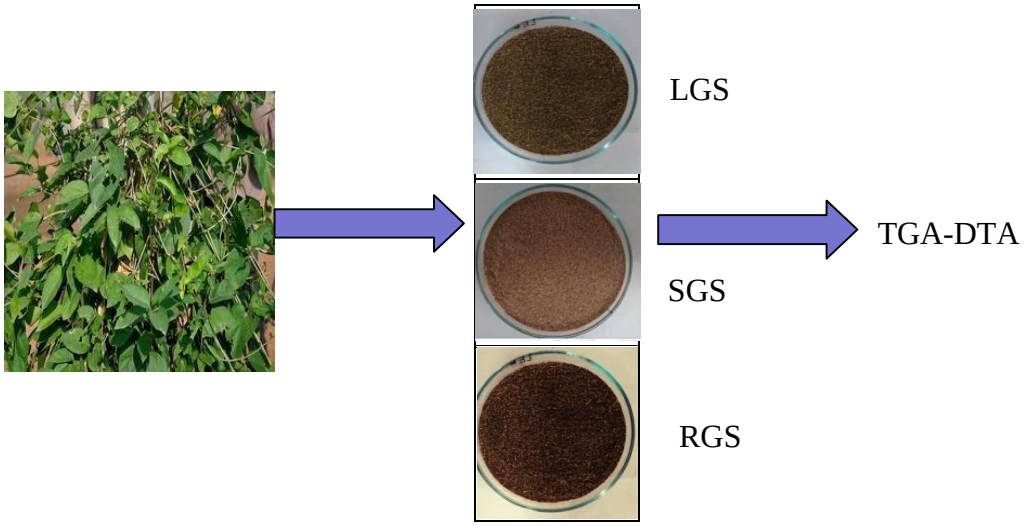

Figure 1 : Powdered sample of Leaves, stem and Root of *G. sylvestre*.

Instrumental Parameter:

TGA-DTA was carried out using Thermal analysis equipment (TGA, DTA), Make and Model: Perkin STA 8000. Analysis was carried out at heat from 35 °C to 700 °C at 10 °C/min rate with suitable cooling attachment with thermocouple sensor Pt-Pt/Rh. For the analysis sample weight of each sample were as taken 20.00 mg.

RESULT AND DISCUSSION:

Themogravimetric analyzer (TGA-Z shaped curve) and Differential Thermal Analyzer (DTA) analysis results for leaves, stem and root are shown in Fig.1, Fig.2 and Fig. 3 respectively. In DTA curve, all samples shows endothermic peak at 101 °C is due to dehydration or loss of water molecule from pores and surface of the powder sample**.**

From graph, it is observed that second weight loss is observed at temperature 350 ^{0}c to 400 ^{0}c in all samples may be due to degradation of cellulose and hemicellulose. Further continue heating between 450-700 °C causes degradation of lignin compounds from *G. sylvestre*.

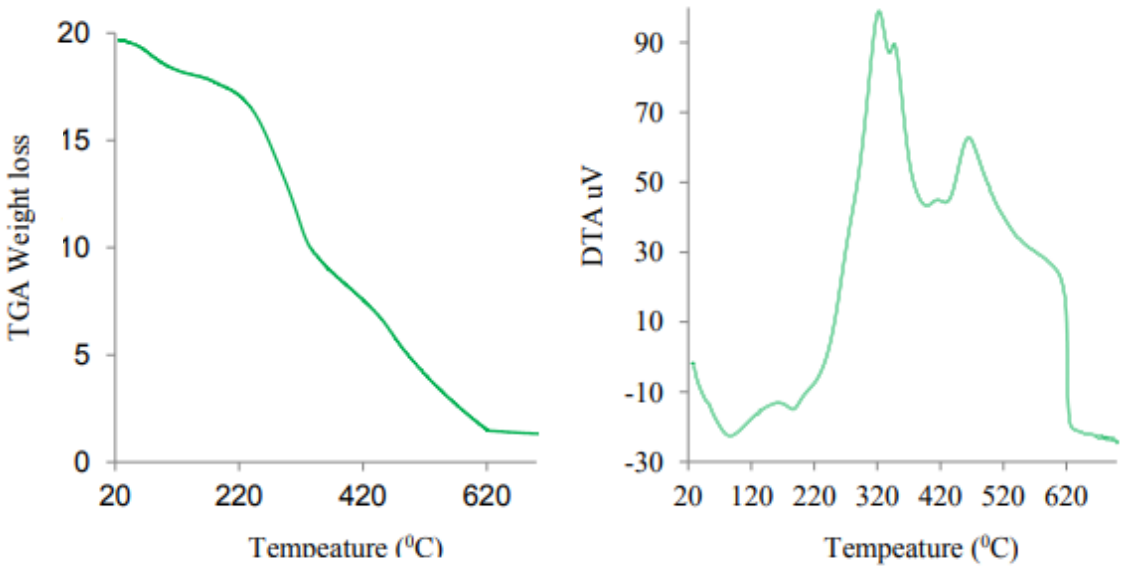

Figure 2. TGA-DTA curves of *G. sylvestre* leaves Powder

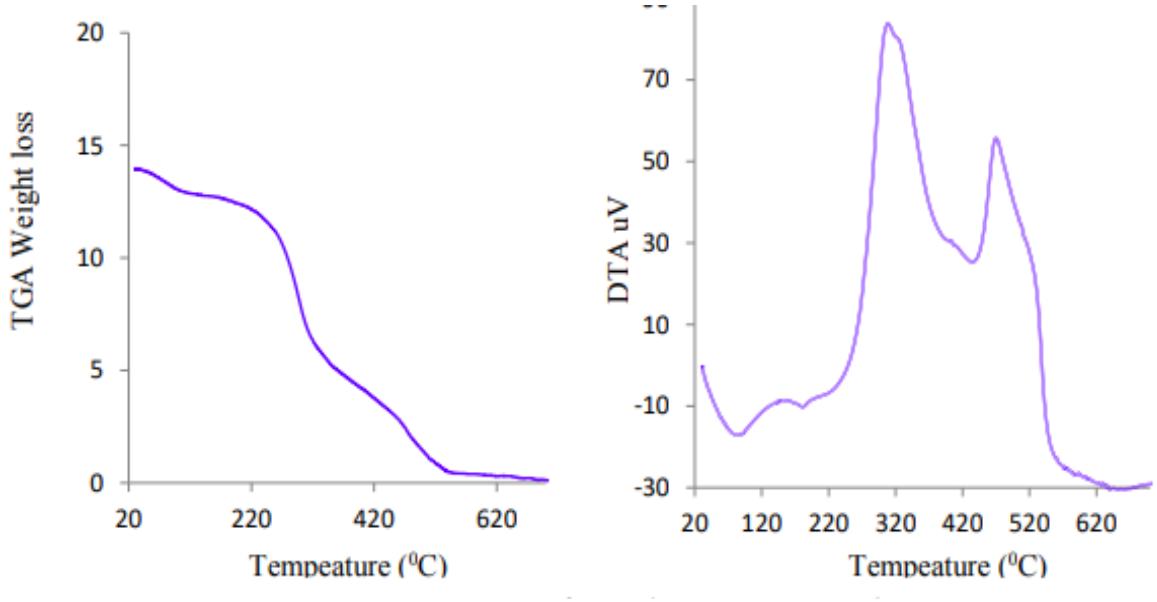

Figure 3. TGA-DTA curves of *G. sylvestre* stem Powder

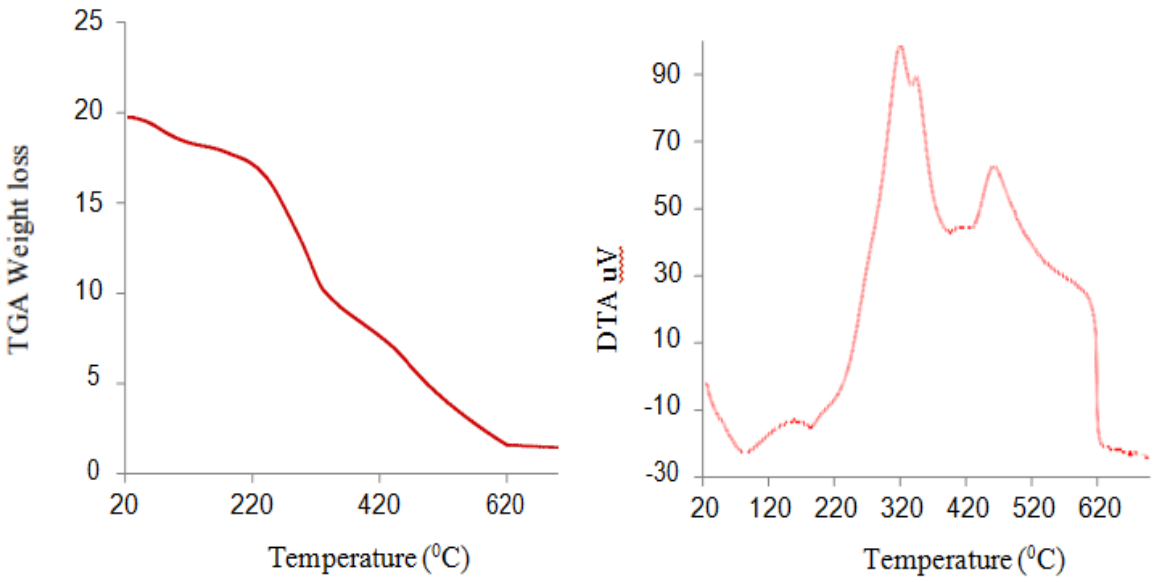

Figure 4. TGA-DTA curves of *G. sylvestre* root powder

CONCLUSIONS:

The thermal analysis method is a powerful tool for study of thermal stability and chemical composition of medicinal plant. The TGA-DTA data can be used for Authetification of medicinal plant and for standardization of herbal drug.

ACKNOWLEDGEMENT:

The authors are thankful for facilities provided by Department of Chemistry, B. Gholap College, New Sangavi, Pune, India and Dadapatil Rajale Art's, Science and Commerce college Adinathnagar, Maharashtra, India.

REFERENCES:

1. Rupanar S. V., Pingale S. S., Dandge C. N., Kshirsagar D., Phytochemical Screening and In vitro evaluation of antioxidant & antimicrobial activity of *Gymnema sylvestre,* International Journal of Current Research, **8** ,11:**2016.**

2. Rupanar S. V., Pingale S. S., Review: Phytochemical and Pharmacological Profile of *Gymnema sylvestre,* International Journal of Engineering Technology Science & Research, 5(3), **2018**.

3. Nair L. D., Sar S. K., Arora A., Thermogravimetric analysis of few medicinal plants of Chhattisgarh State, International Journal of Current research in chemistry and pharmaceuticalsciences.2(6),1-5**,2015.**

4. Wang Y., Application of Fourier Transform Infrared Micro spectroscopy (FTIR) and Thermogravimetric analysis (TGA) for quick identification of Chinese herb *Solanum lyratum, 5*(6),50-513,**2012**.

5. Pingale S. S., Chaskar M. G., Kakade N. R., Thermo gravimetric and Elemental Analysis of Caesalpinia bonducella Leaves Powder, Journal of Emerging Technologies and Innovative Research, 6(5),109-113,**2019.**

6. Naik D. G., Dandge C. N., Rupanar S.V., Chemical Examination and Evaluation of Antioxidant and Antimicrobial Activities of Essential Oil from *Gymnema sylvestre* R. Br. Leaves, Journal of Essential Oil Research, 23:13-19, **2011.**

7. Pingale S. S., Rupanar S.V., Chaskar M. G., Phytochemical analysis and Antioxidant activity of aqueous fruit extract of *Gymnema Sylvestre.* International Journal of Scientific and Research Technology; 4(2), **2018.**

Paper-12

"THE INTERNET-BASED CLASSROOM EDUCATION FOR VISUAL ARTS: CHALLENGES & OPPORTUNITIES"

Author: ***Dr. Shraddha Kaje****,*
Ph.D. Assistant Professor, Faculty of Art & Design,
Vishwakarma University, Pune.

Co-Author: ***Dr. Mukta Shirke****,*
Ph.D. Assistant Professor, Faculty of Art & Design,
Vishwakarma University, Pune

Abstract:

E-learning has had a huge impact on higher education. Many experiments were done by academicians in designing courses or applying E-learning to Visual Arts education. It was quite difficult to shift traditional learning into online mode suddenly as visual arts are concerned with experience based education. The challenges faced by students and academicians have been observed. Furthermore, this paper intended to explain the advantages and disadvantages of online learning within the context of practice-based tasks, which focus on practical skills. This paper examines quantitative and qualitative survey with data collection from academicians and from students who had experienced teaching-learning process since 2019. The observations have been stated for traditional and online education. Deliberations are made by watching various angles of it.

Keywords: Visual Arts Education, Teaching-learning, Internet-based education, Practice-based education

Objectives:

- To analyse the challenges faced in the teaching-learning practices of visual arts subjects.
- To analyse the Strengths, Weaknesses, Opportunities & Threats of internet-based learning for teachers and learners.
- To suggest possibilities for interactive and engaged studio learning for practical subjects of Arts & Design.

Introduction:

The fact of 21st century's education can be mentioned as e-learning, which involves addition of communication technologies in education. Because of this change and revolution process; traditional education practices have started to be implemented through new tools and technological settings. The change and renovation in education, which started with the process of assimilating communication technologies into education, also marked the way for the development of alternative systems to traditional education practices and further

consolidation of existing systems such as distance education through Internet-based learning (Dilmac, 2020). Technological inventions, which establish the basis and the starting point of the idea of distance education, marked the way for the training of individuals and collective structures at different times and places, and a new practice has emerged without the need for physical contribution. As mentioned in the research paper by Dilmac; Aytekin İşman stated that "Internet-based education, which is carried out in environments where teachers and students are separated from each other in terms of time and place" (Dilmac, 2020).
In this context, Internet-based education, which provides an equal chance of education for the individual who establishes difficulty for financial situation and cannot join in educational activities may be due to natural or pandemic circumstances, Internet learning attempts to exclude these hitches through means of communication use and reaches education to large masses.
The Covid-19 outbreak experienced by all over the world brought the revolution in education back to the agenda by forcing Internet-based education. Educational institutes and online education solutions have been forced to work on and improve quality and delivery for handling such situations during pandemic. Zoom, Google Meet, Teams, etc. became new digital classrooms, and the screens were new blackboards. Digital learning became the need and the only option left to reimburse for the loss education suffered through. In this sudden shift, educational institutions have rapidly adopted new approaches to stand-in student success in these strange times. Practical domains of Visual Arts, like Fine Arts or Applied Arts/Design will be challenging for the teacher as delivery of subject is determined to be practice-based and experience-based. It is difficult to see long term impact of change of medium for students. According to a report many doubts regarding the need of using face to face education will be settled without taking advantages of technologies once the offline education starts (United Nations Educational, 2020).

This study defines how online visual art courses are needed to be designed to overcome the challenges and worries and make learning an enjoyable virtual experience, with a collaborative approach. Qualitative and Quantitative survey of student's and teacher's evaluations of teaching and learning on various internet-based platforms have been collected and analyzed. Based on the data and findings, suggestions for the strategy of online Visual Arts courses have been provided.

1. Review of Literature:

Plenty of studies have been done on online education for school and higher level education. Studies have been done, to define and decide the effect of internet-based education on students as well as teacher's perceptions (CHAUDRY & -RAHMAN, July 2010). Many studies have been done to study the effect of online education on students perception, issues of student support services and feedback of students. Open Distance Learning can provide equal opportunities to all to learn and for contributing nation's progress (Dimri & Chaturvedi, 2009). Bolliger & Halupa endorse that internet-based education has an effect on student motivation (Bolliger & Halupa, 2018). Adams and Timmis bring into being that web-based exercises cause problems in communicating and conversing between students and student-teacher/educators. They also mention the problem of student isolation (Audrey & Timmins, 2006). As mentioned in the research article by Dilmac, he mentioned about the research conducted by Halter, Kleiner and Hess (2006) on 45 students, the students who did not want to leave their teams and their families stated that they were happy to participate in web-based learning (Dilmac, 2020). One study compared the symbolic perceptions of students regarding

face to face education and distance education, it was determined that internet education is not necessary for those who receive face to face education (sciedupress, 2020).
Researchers are also working on finding ways to raise involvement through online learning. In addition, there is a significant effort done to recognize the factors that affect student participation. Visual Art is an applied field of art and design education. Beyond the cognitive development of the student, determining students' views for these courses, which are necessary for their emotional development, the evaluation done by various researchers is important for student and teachers attitudes. In this context, the aim of this study is to determine the views of students as well as teachers of Visual Arts since the year 2019.

2. Traditional Teaching-learning practices in Visual Art Classrooms/ Studios:

Visual Arts are the human expressions in visual forms with aesthetic aspects, process, and representation. In other ways, it can be defined as a medium for visual communication. Visual Arts comprise the historical development of art and culture. Exploration of several demonstrative expressions through art forms such as painting, drawing, printmaking, sculpture, ceramics, photography, video, filmmaking, design, crafts, and architecture. The current usage of the term "visual arts" includes fine art as well as the applied, decorative arts and crafts. Expected learning outcomes in visual arts include creation and representation of thought, concept, or idea in the form of drawing design or craft. Teaching pedagogies mostly include demonstration, one-to-one guidance, display & observation, presentation. Which are more visual-based or interactive-based.

The Arts are about ‘what it is to be human’ (Thomas, 2014). They strengthen student’s understandings and information of other artists which is responsible for a way to ‘symbolize Indigenous, worldwide knowledge, people, histories and cultures. In the Visual Arts studio, teachers assist student’s creativity, imagination and bits of intelligence to cultivate their capacity to critically investigate and reflect on the creative process. It involves the improvement of artistic understanding of design elements and languages. Throughout the teaching-learning atmosphere, the teacher cultivates individual and common expressions and promotes active engagement and thinking individually and collectively. Students create their own artwork, which expresses ideas, observations, experiences, which consider viewers and purposes for their artworks. Students are involved in communicating their own art practice through active engagement in traditional education. It requires a range of tools, technologies and studio spaces. Students develop skills that will help them to satisfy creation and working lives. These studio practices provide students excellent career prospects. Offline studio learning involves experience based learning and the results and evaluation process takes step wise immediately. Teachers can guide students through interaction, demonstration, correction in physical workspace. This evaluation is specially needed in the domains like Painting, sculpture, drawings.

Fig.1. Traditional practices in Visual Art education.

3. Visual Arts and Internet-based education:

There are five key Proposes of visual arts; creative, expression, practical, influential, and formal likewise to the narrative. Visual arts are connected with all communities in our society. It has been normally observed that to study visual arts, few aptitudes are needed, observation from surrounding, artistic mind, and imagination power adequately. Visual arts have many forms that enable to set human emotions & skills (GOMES, 2019). In internet based education it is not possible to provide these basic essentials.
Through this study, we are trying to discuss the teacher's argument as an academician to teach these 80-90% practical based subjects on an online platform to undergraduate students of Applied Arts/Design and Fine Arts. Studies have shown that issues like creating demonstrations, internet connectivity and evaluation of assignments need to resolve efficiently in visual arts education. One of the major challenges for teachers was to create video setup to record and shoot videos. Bandwidth problem or image resolution problem occurred many times while streaming of demonstrations (Avachat-Shirke, 2021)

Alter identifies, it is very challenging to teach visual Arts subjects, due to entrenched pedagogical practices as well as lack of experience or knowledge regarding online platforms. She offers concrete approaches and advice for translating reflexive, performance-based Visual Arts pedagogy into eLearning modalities (Frances). It is a growing reality that teacher educators will need to become cognisant of online platforms as their teaching spaces.

Fig.2. Generalized Stages of Studio-based learning for visual Art courses

4. Methods & Findings:

Data Collection Tool and method of analysis-
For data collection, questionnaires were provided to academicians and students of visual arts to know the consequences of online education. The set of questions was open-ended and closed-ended (yes or no and rating scales) Cells were left blank if questions were unanswered. The frequency and percentages of positive or negative responses to the survey were documented.

Study Group- This research, carried out in order to determine the opinions of Academicians and students regarding the Internet-based education process, in the context of Fine arts and Applied Arts/design since 2019 academic year. 50% of responses from Applied Arts/Design and 50% of responses from Fine Arts were selected.

Qualitative analysis was later conducted by comparing and conflicting responses to each set of questions. Here are some of the findings-

Survey Analysis: Study Group-1 (Student)

Sample size: **Undergraduate Student- 20**
100% students are using online platform. Google Meet, ZOOM, WebEx, Microsoft teams Google classrooms and university's online education platforms have been widely used for assignment submission. According to the survey most students preferred actual studio based learning. One student mentioned that As a Fine Arts student, online platform binds them to a screen and for the practical subject it is difficult to learn on a screen.

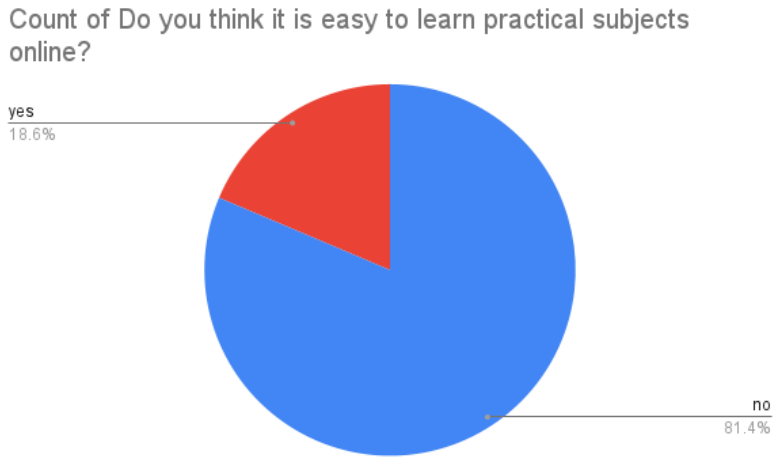

Fig. 3 Pie chart analysis for the question 'Do you think it is easy to learn practical subjects online?'

There are disadvantages more like not getting fieldwork knowledge, problems in understanding instructions, difficulty in getting feedback, difficulty in understanding the subject. Many students feel the lack of connection between teachers and students.

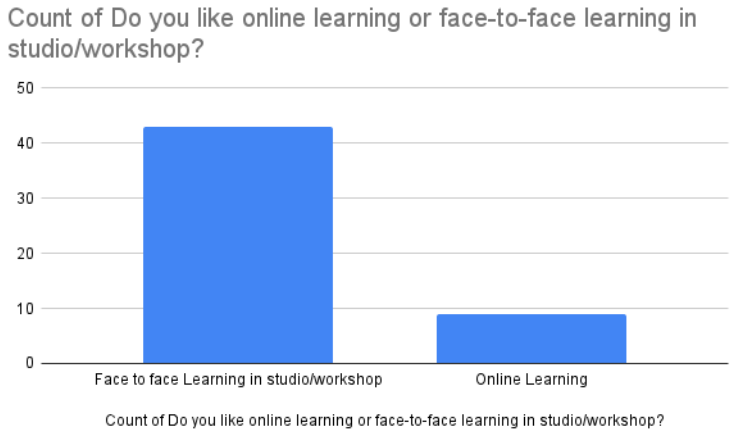

Fig. 4 Histogram of responses for 'Do you like online learning or face-to-face learning in studio/workshop?'

It is as opportunity for students to connect with mentors worldwide because of online courses. According to students, gaining theoretical knowledge online is much more easier than learning practical skills. Students had to submit all the submission through online mode.

Sometimes uploading images or visual data is a difficult task as it cannot give the actual tactile experience in 3D creations. One student mentioned that Images not give that experience and willingness to draw as compare to 3d models. In 3d model or still life students can catch the things properly and clearly without any disturbance. Also to get actual size of models/ objects in front of the eyes create the sense of space. Some of them mentioned that it was difficult for them to understand the feedback of teachers. Now students have adapted the techniques of online education. Although some enjoyed this phase and mode of learning; some of them are still not satisfied with the experience.

Survey Analysis: Study Group-2 (Teachers)
Sample size: **Teachers- 14**

100% teachers are using platforms like Google Meet, ZOOM, WebEx, Microsoft teams prominently. Teaching involves different subject courses aligned to Applied Art, Design, and Fine Art. Courses like Illustration, Calligraphy, Drawing, Visual Communication Design, UI, Photography, Colour and composition, Typography, Accessory Design etc. are also taught along with subjects like Mural, Painting, Anatomy drawing, Composition in online teaching.

Satisfaction rate of student learning output measured on a rector scale of 1-5 resulted to 3.54, indicating an average satisfaction.

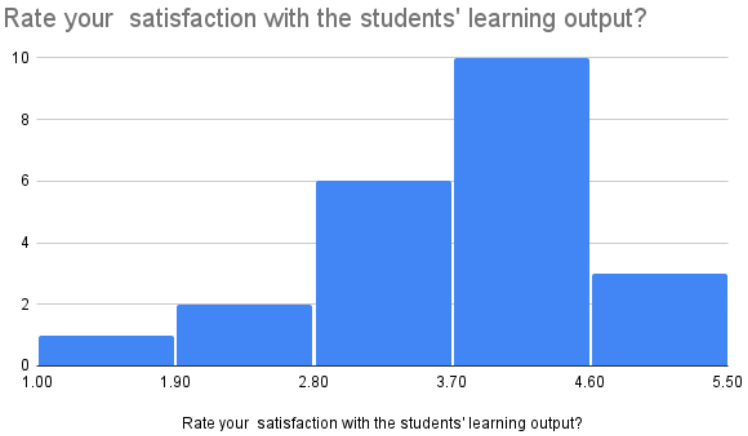

Fig. 5 Histogram of responses for ‘Rate your satisfaction with the students’ learning output?’

Various answers were received which showed the innovative techniques of teaching / demonstrating practical subjects. One academician mentioned that he demonstrates the artwork through pen tablet and screen sharing. The online courses like Swayam, NPTL are being explored and used. Youtube channel are also started by few faculties which provides audio-video recording of lectures and demonstrations.

Experiencing of physical/original artwork is a setback towards assessing students’ artworks. Actual value of colour and intensity of tone is difficult to analyse. Copied work, Delay in submission etc is the major drawback together with minor correction and guidance. The visual quality of work assignments is lost as an online medium has its own limitation. Creating videos / demonstrations, preparing presentations, digital class, personalized WhatsApp follow up, keeping camera on to understand students’ struggle points, live

demonstrations, conduct activity-based sessions etc. are some of the personal strategies observed by the respondents in online teaching.

Academicians mentioned that technology opens many possibilities / opportunities of self-learning and improvement. The tools like AR & VR Google classroom has been extensively used which provides digital assistance to the students while learning. Work presentation and discussion with the students become easy and personalized. Web-based education establishes a worldwide student-teacher connection through webinars, workshops and training.

SWOT analysis

SWOT analysis of internet based Classroom Education for Visual Arts have been done from the data received.

Strengths	Weakness	Opportunities	Threats
Online medium is accessible at anytime from anywhere, can reach to large number of students	Teacher-student interaction is missing.	New ways of education or creative tasks creation can be done	Students can take disadvantages of technology

Fig. 6 SWOT analysis of internet based Classroom Education for Visual Arts

Conclusion:

This analysis reveals that although there are many limitations for internet based classroom education for visual arts it opens many opportunities for students as well as teachers. Gaining multiple views on same subject is possible because of various online courses worldwide. The findings of this study will support further debate and future research regarding solving issues of online education.

Visual Arts can be taught with meaningful and deep engagement of in-service teachers in the Art world, through direct experiences with art making and critical practice in physical studios. Online education cannot provide the experience of space and experience of group activities where students are involved mentally with each other. Academicians and students have accepted this new way of education created strategies individually to perform better. This study also elaborates on students' attitudes and inspirations toward online education as a learner. Online learning can only function as a supporting method to the sector of Visual Arts that focuses on the development of practical skills, where conventional learning methods which are characterized by practice-based learning are more appropriate and effective.

Works Cited

(n.d.).

sciedupress. (2020). Retrieved october 4, 2021, from http://wje.sciedupress.com: World Journal of Education Vol. 10, No. 3; 2020 Published by Sciedu Press 115 ISSN 1925-0746 E-ISSN 1925-0754

Audrey, A., & Timmins, F. (2006). Students views of integrating web-based learning technology into the nursing curriculum – A descriptive survey. *Nurse Education in Practice*, 12-21.

Avachat-Shirke, M. (2021). Online Learning for Practical Subjects (In special reference to COVID-19 duration). In D. D. Singh, *Covid-19 Crisis and India* (pp. 97-105). Delhi: Adhyaya Publishers and Distributers.

Bolliger, D., & Halupa, C. (2018). Online student perceptions of engagement, transactional distance, and outcomes. *Distance Education, 39:3,* , 299-316.

CHAUDRY, M. A., & -RAHMAN, F. (July 2010). A CRITICAL REVIEW OF INSTRUCTIONAL DESIGN PROCESS OF DISTANCE LEARNING SYSTEM. *Turkish Online Journal of Distance Education, 11*, 193-204.

Dilmac, S. (2020). Students' Opinions about the Distance Education to Art and Design. *World Journal of Education*, 113-126.

Dimri, A., & Chaturvedi, A. (2009). Analysis with Learner Input of Student Support Services in India. *Asian Journal of Distance Education, 7(2),*, 4-16.

Frances, A. (n.d.). The experience of teaching tertiary visual arts education in a purely online learning environment. *Australian Art Education, 36(1),* , 48-64.

GOMES, J. (2019, July). *Importance of Visual Arts in Education.* Retrieved October 2, 2021, from Schools of dehradun: https://www.schoolsofdehradun.com/informational/importance-of-visual-arts-in-education/

Thomas, P. 1. (2014). HOW IS THE DOMAIN OF THE VISUAL ARTS REPRESENTED IN YEARS 7-10 IN STATE CURRICULUM FRAMEWORKS IN VICTORIA, QUEENSLAND AND NEW SOUTH WALES? *Australian Art Education* , 12-25.

United Nations Educational, S. a. (2020). *Covid-19 and Higher Education: Today and Tomorrow - Impact Analysis, Policy Responses and Recommendation", .* America: (IESALC), UNESCO .

Paper-13

Study of pH of Rhizospheric and Non- Rhizospheric soil of *Lablab purpureus* (L)

Chavan V. S.
Department of Botany
Anandibai Pradhan Science College, Nagothane, Roha, Dist-Raigad, India

Abstract: In present study hydrogen ion concentration of different samples of rhizospheric and non- rhizospheric soil of *Lablab purpureus* (L) was recorded. The pH of soil controls many of the chemical and biological activities that take place in the soil and indicates about the climate, vegetation and hydrologic conditions under which the soil formed.

Key Words: Physicochemical parameter-pH, Rhizosphere,Non- Rhizosphere, Microorganism etc

Introduction: Soil has different types of microorganisms which increase the living population. This living population increase the humus in soil to produces enzymes and liberate CO_2, Organic acids etc. They are responsible for bringing about numerous transformations which change the nutrients in to readily available forms which can be formed by plants. Hence the biological population has an important role to play in this planet.

The various types of micro-organisms present in soil. Among that VAM fungi are an important group of organisms. The VAM symbiotic association with the roots of the plants. The existence of these organisms is dependent on the physical and chemical properties of soil. The physical factors that influence VAM population and other microbial populations are texture, moisture content, temperature and pH etc of soil.

The chemical factors include pH, nitrogen, phosphorus, potassium etc. Several workers have studied the effect of these chemical factors on mycorrhiza. Soil system is the most important ecological factor on which the plants are dependent for their establishment, nutrition, water and mineral supply. Soil system is very complex and dynamic ,undergoing continuous change in its physicochemical parameters throughout the year. In the present study, physicochemical parameters, namely pH, was recorded.

These parameters vary in amount depending upon the texture and physical and chemical properties of soil. Their status is recorded to detect the available nutrients from all the sites for Sweet bean plants during the study. Seasonal variations are focused to study the effect of physicochemical parameters on the development of AM fungi,their number and the rate of colonization. Variations in physicochemical parameters for each selected sites for three years were recorded.Rhizosphere and non-Rhizosphere soil were collected from four different sites,which includes L-1 Chochinde, L-2 Dasgaon, L-3 Kondivate and L-4 Kol, for the year 2015-2017.

Materials and methods: During present investigation four villages from Mahad Taluka of Raigad District, Maharashtra (India) were selected as a case study. These localities were Chochinde, Dasgaon, Kondivate and Kol. Maharashtra state is divided in six divisions like Konkan, Nashik, Pune, Aurangabad, Amravati and Nagpur. Konkan division is divided into five districts viz. Raigad, Ratnagiri, Thane, Palghar and Mumbai. Raigad District is located between 17^0 and 51^0 North latitude and between 73^0 and 40^0 East longitude at 720 meters above mean sea level. Total area of the district is 7152 sq. km. Average rainfall of the district is 3028.9 mm. The maximum temperature in summer is 42^{o}C and minimum temperature in winter is less than 30^{o}C. Relative humidity ranges from 65% to 75%. Raigad District has Raigad, Pen, Panvel, Uran, Karjat, Khopoli, Alibag, Murud, Pen, Roha, Sudhagad, Tala,

Mangaon, Shrivardhan and Mahad Taluka. The present work was conducted for understanding the association of Arbuscular Mycorrhizal Fungi (AMF) with respect to their morphotaxonomy, ecology, water stress and relation of AM fungi and Rhizobium with *Lablab purpureus.*

The pH is one of the important parameters that determine the chemical nature of a soil sample. For determining the pH, 50 g of dried soil was mixed with 50 ml of water (1:1) thoroughly with the help of a glass rod, and then it could settle for some time.

The pH of the supernatant was measured using the pH paper by dipping it and comparing with the standard colour against its corresponding value. The pH requirements for germ tube production relates to the ability of different AM fungal isolates to survive and adapt to the environment. Very less attention has been given on the effect of pH on AM fungi [4] however, for specificity of AM fungal species to pH and its effect, some attempts were made.

Result: Soil pH is an indication of the soil's chemistry and fertility [6]. The pH affects the chemical activity of the elements in the soil, as well as many of the soil properties [5]. The pH of soil controls many of the chemical and biological activities that take place in the soil and indicates something about the climate, vegetation and hydrologic conditions under which the soil formed. The pH or the amount of hydrogen ions in a sample is an important consideration when studying soil. As in the study of hydrogen, the pH scale is used as an indication of the concentration of hydrogen ions in the soil. pH is measured on a logarithmic scale and represents the negative logarithm of the hydrogen ion concentration in moles/L.

When soil contains a high concentration of hydrogen ions, it is considered to be acidic and when it has a low number of hydrogen ions, it is considered to be basic, pH 7 is considered to be "neutral"(neither acidic nor basic).The pH

scale ranges from 1-14 with pH 1 being extremely acidic and pH 14 being extremely basic.

Soil pH Rhizosphere and Non-Rhizosphere (Year 2015)

Sr. No.	Locality	pH											
		Oct		Nov		Dec		Jan		Feb		Mar	
		R	NR	R	NR	R	NR	R	NR	R	NR	R	NR
1	L-1	6.9 N	7.1 N	6.7 N	6.9 N	6.8 N	6.9 N	6.7 N	6.9 N	6.8 N	6.8 N	6.9 N	6.9 N
2	L-2	6.1 A	6.0 A	6.3 A	6.1 A	6.1 A	6.2 A	6.2 A	6.0 A	6.2 A	6.4 A	6.1 A	6.4 A
3	L-3	6.8 N	7.2 N	6.8 N	7.2 N	6.9 N	7.1 N	6.9 N	7.0 N	6.8 N	7.1 N	6.7 N	7.0 N
4	L-4	6.4 A	6.3 A	6.3 A	6.1 A	6.2 A	6.2 A	6.3 A	6.1 A	6.2 A	6.4 A	6.2 A	6.2 A

L-1 Chochinde, L-2 Dasgaon , L-3 Kondivate and L-4 Kol

In 2015 pH of all four localities was acidic and neutral ranging from 6.0 to 7.2 recorded in month October to March. It was recorded maximum 7.2 in October and November at L-3 it was normal for non- Rhizosphere soil. However acidic pH was recorded in all months at L-2 and L-4for both Rhizosphere and non-Rhizosphere soil and Neutral pH was recorded at L-1 and L-4 for both Rhizosphere and non- Rhizosphere soil respectively.

Soil pH Rhizosphere and Non-Rhizosphere (Year 2016)

Sr No.	Locality	pH											
		Oct		Nov		Dec		Jan		Feb		Mar	
		R	NR	R	NR	R	NR	R	NR	R	NR	R	NR

1	**L-1**	7.1 N	7.1 N	6.9 N	7.2 N	6.8 N	7.0 N	6.7 N	6.9 N	6.8 N	7.2 N	6.9 N	6.9 N
2	**L-2**	6.1 A	6.0 A	6.3 A	6.0 A	6.1 A	6.3 A	6.2 A	6.2 A	6.2 A	6.2 A	6.1 A	6.0 A
3	**L-3**	7.0 N	7.2 N	6.8 N	6.9 N	6.9 N	7.1 N	6.9 N	6.9 N	6.8 N	6.7 N	6.7 N	6.9 N
4	**L-4**	6.4 A	6.3 A	6.3 A	6.2 A	6.2 A	6.0 A	6.3 A	6.1 A	6.2 A	6.0 A	6.2 A	6.2 A

L-1 Chochinde, L-2 Dasgaon , L-3 Kondivate and L-4 Kol

In 2016 pH of all four localities was acidic and neutral ranging from 6.0 to 7.2 recorded in month October to March. It was recorded maximum pH 7.2 in October at L-3 it was normal for non- Rhizosphere soil pH 7.2 also recorded in November and February at L-1. However acidic pH was recorded in all month at L-2 and L-4 for both Rhizosphere and non- Rhizosphere soil and Neutral pH was recorded at L-1 and L-3 for both Rhizosphere and non- Rhizosphere soil respectively.

Soil pH Rhizosphere and Non-Rhizosphere (Year 2017)

Sr. No.	**Locality**	**pH**											
		Oct		**Nov**		**Dec**		**Jan**		**Feb**		**Mar**	
		R	**NR**	**R**	**NR**	**R**	**NR**	**R**	**NR**	**R**	**NR**	**R**	**NR**
1	**L-1**	7.1 N	6.9 N	6.9 N	7.2 N	7.3 N	7.0 N	7.1 N	7.0 N	6.9 N	6.9 N	7.1 N	7.2 N
2	**L-2**	6.0 A	6.3 A	6.3 A	6.0 A	6.1 A	6.1 A	6.2 A	6.2 A	6.2 A	6.3 A	6.1 A	6.0 A
3	**L-3**	7.2 N	6.9 N	6.8 N	7.1 N	6.8 N	6.9 N	6.9 N	6.6 N	6.8 N	6.6 N	6.7 N	7.1 N
4	**L-4**	6.4 A	6.1 A	6.3 A	6.2 A	6.2 A	6.4 A	6.3 A	6.3 A	6.2 A	6.3 A	6.2 A	6.3 A

L-1 Chochinde, L-2 Dasgaon , L-3 Kondivate and L-4 Kol

In 2017 pH of all four localities was acidic and neutral ranging from 6.0 to 7.2 recorded in month October to March. It was recorded maximum 7.2 in October for Rhizosphere at L-3 and November and March at L-1 it was normal for non-Rhizosphere soil. However acidic pH was recorded in all months at L-1 and L-2 for both Rhizosphere and non- Rhizosphere soil and neutral pH was recorded at L-1 and L-2 for both Rhizosphere and non- Rhizosphere soil respectively.

Discussion: The three year result was recorded from 2015 to 2017 for rhizosphere and non rhizosphere soil. The pH of the soil was neutral to slightly acidic ranging from 7.2 to 6.00 in month October to March. Soil pH influences VAM fungal species composition, colonization and effectiveness [2]. The genus *Acaulospora* and *Glomus* are the dominant myco species in the rhizosphere soil, collected from four locality of Mahad taluka. The possible reasons for the predominance of *Glomus sp*. are that spores of *Glomus* species have different temperature and pH preferences for germination [2] and *Acaulospora* species are often associated with acidic soils [3].

Coclusion*:* The three years result recorded from 2015 to 2017 of rhizosphere and non rhizosphere soil. The pH of the soil was neutral to slightly acidic ranging from 7.2 to 6.00 in month October to March. Soil pH influences VAM fungal species composition, colonization and effectiveness [1] The genus *Acaulospora* and *Glomus* are the dominant myco species in the rhizosphere soil, collected from four localities of Mahad Taluka.

Acknowledgment - I am grateful thank to **Dr.M.R.Meshram**, Principal, Gokhale Education Society's Arts,Commerce and Science College,Shrivardhan,Dist-Raigad for providing research laboratory to undertake present work. I also thank **Dr.Sandesh Gurav**, Principal, Konkan

Education Society's. Anandibai Pradhan Science College, Nagothane, Raigad for encouragement and moral support time to time.

References:

1.Akhtar, M. S. and Z. A. Siddiqui 2009. Effects of phosphate solubilizing micro organisms and *Rhizobium sps.* On the growth, nodulation, yield and root-rot disease complex of Chick pea under field condition. *African Journal of Biotechnology*, 8(15): 3489-3496.

2.Hayman, D.S. and M. Tavares 1985. Plant growth responses to vesicular-arbuscular mycorrhiza XV: Influence of soil pH on the symbiotic efficiency of different endophytes, *New Phytol*, 100: 367-377.

3.Azcón, R., Gomes, M. and Tobart, R. 1996. Physiological and nutritional responses by *Lactuca sativa* L. to nitrogen sources and mycorrhizal fungi under drought stress conditions. *Biol. Fert. Soils*, 22:156-161.

4. Cox, G. and Tinker, P. B. 1976. Translocation and transfer of nutrients in vesicular

arbuscular mycorrhizas. I. The arbuscule and phosphorus transfer: a quantitative

ultrastructural study. *New Phytologist*, 77:371–378

5.Bray, R. H. and L. T. Kurtz 1945. Determination of total, organic and available forms of phosphorus in soils. *Soil Sci.* **59:** 39-45.

6. Goicoechea, N., Antolín, M. C. and Sánchez-Díaz, M. 1997. Gas exchange is related to the hormone balance in mycorrhizal or nitrogen-fixing alfafa subjected to drought. *Physiologia Plantarum*, 100: 989–997.

PAPER-14

A THEORETICAL AND EXPERIMENTAL STUDY OF TEMPERATURE DEPENDENT THERMAL CONDUCTIVITY ENHANCEMENT OF FUNCTIONALIZED NANOFLUIDS

Vijay S. Raykar[1]*

Department of Physics, G. M. Vedak College of Science, Tala,

(Affiliated to University of Mumbai) Maharashtra, India.

Abstract: A theoretical study of effective thermal conductivity (ETC) of Nanofluids (NFs) is carried out. The Carbon Nanotube (CNT) based Nanofluid (NF) has been synthesized by two-step synthesis method. ZnO/Silver based NFs were synthesized by single step wet chemical method. Hot wire transient method was used to measure the thermal conductivity of NFs. The various models of ETC in the current literature were discussed and are applied to our experimental data. New model have been compared to experimental data, which explains the anomalous behaviour in the thermal conductivity of NFs.

Keywords: Effective medium theory, Brownian motion, Carbon nanotubes, Nanofluids, Thermal Conductivity

Introduction

Recent work suggests that NFs, dispersions of nanometer-sized particles, CNTs in fluid, have the ability to increase the amount of thermal transport beyond what most conventional coolants can see today [1-3]. Since carbon nanotubes exhibit the highest thermal conductivity of any material known to man, the addition of them to conventional heat transfer fluids should, in turn, increase the fluid's thermal conductivity and effusivity [3-6]. Results indicate that through the uses of ionic surfactants, chemical functionalization, and the use of ultrasonication stable dispersions, on the order of months, can be obtained in water and ethylene glycol with loadings of carbon nanotubes as low as 0.001 wt%. [7]. Tests on the thermal conductivity and effusivity of the prepared samples reveal increases of nearly 85-90% [8]. Further tests on the viscosity and electrical conductivity of the added nanoparticles/CNTs reveals that charge interactions implemented by surfactants play an important role in the stability and subsequent increase in transport properties of the fluids [9]. The large thermal conductivity enhancements reported by experiment led to excitement but also to controversy [10]. The origin of the excitement was that the measured thermal conductivity was often much larger than that predicted by well-established effective medium theories under the assumption of well-dispersed particles. [11].

Most of the NFs fall naturally in to the two classes: those NFs in which one component is a metal/metal oxide NPs and surfactant and those in which the former is replaced with CNTs. Many NFs in both classes have been studied, but, because of the macroscopic scale for colloids and composites description now changed to nanoscale with different physics, the Effective Medium Theory (EMT) of Maxwell and Brugemann is not appropriate to predict

their transport properties [12]. Instead, the differential EMT developed by Gao and his coworkers for rod like inclusions and modified by us for CNT NFs, has been applied in conjunction with Brownian motion theory developed by Choi et al [1, 13]. Unfortunately, in spite of its wide application to NFs, the validity of this approach is still open to some questions [13]. In this formulation, for example, a CNT approximated as rod for calculation of ETC. Temperature dependence was explained in dynamic Brownian motion part but not in EMT part and two phase system is assumed in spite of NFs which are now mostly hybrid ones. The model discussed in this study consist of the Static mode and Brownian motion induced nanoconvection mode with the inclusion of effective dispersion term for volume fraction.

Experimental

Dispersing CNTs/Nanoparticles

The solvable properties of nanoparticles/CNTs in water show a behaviour, which is intermediate between that of homogeneous solution (complete dispersion) and that of incomplete dispersion [14]. Consider for instance the case of CNTs in water without surfactant; its sedimentation properties will be different from those dispersions, which contain various moieties, which make them partially water-soluble. To break the CNTs bundle in water it requires high power of ultrasonication as compared to time of ultrasonication. Increase in the power of ultrasonication increase the defragmentation of CNTs [15]. A CNT is chemically extremely stable because the valence of all its carbon atoms are saturated, which makes difficulties in electrostatic charge generation on them through various surfactants.

Synthesis of NFs

The existing methods of NF synthesis are divided into the single-step and two-step processes. In the single step, NF can be produced during one process cycle. The advantage is reflected by the fact that produced nanoparticles are usually small (2-30 nm), agglomeration is minimized, and the produced NFs are the stable ones. Silver NF was obtained by reduction of silver nitrate with PVP in ethanol under the effect of microwave radiation [16]. In the two-step methods, the nanoparticles are firstly produced and then incorporated into base the fluid. In comparison with the single step methods, the two-step method is preferable for the particles of oxides because of their lower tendency to agglomeration. Zinc oxide NFs are synthesized by this route with acetylacetone as a dispersant [17]. CNT based NFs are synthesized with the help of ultrasonication of CNTs in water containing various surfactants [18]. Figure 1 shows the SEM micrographs of nanoparticles/CNTs used in this study. Silver nanoparticles are trapped in PVP matrix with the typical size of 30nm (Figure 1a). ZnO nanoparticles are of the size of 100nm as can be seen in Figure 1b. CNTs are of uniform size and having the diameter of 80nm (Figure 1c).

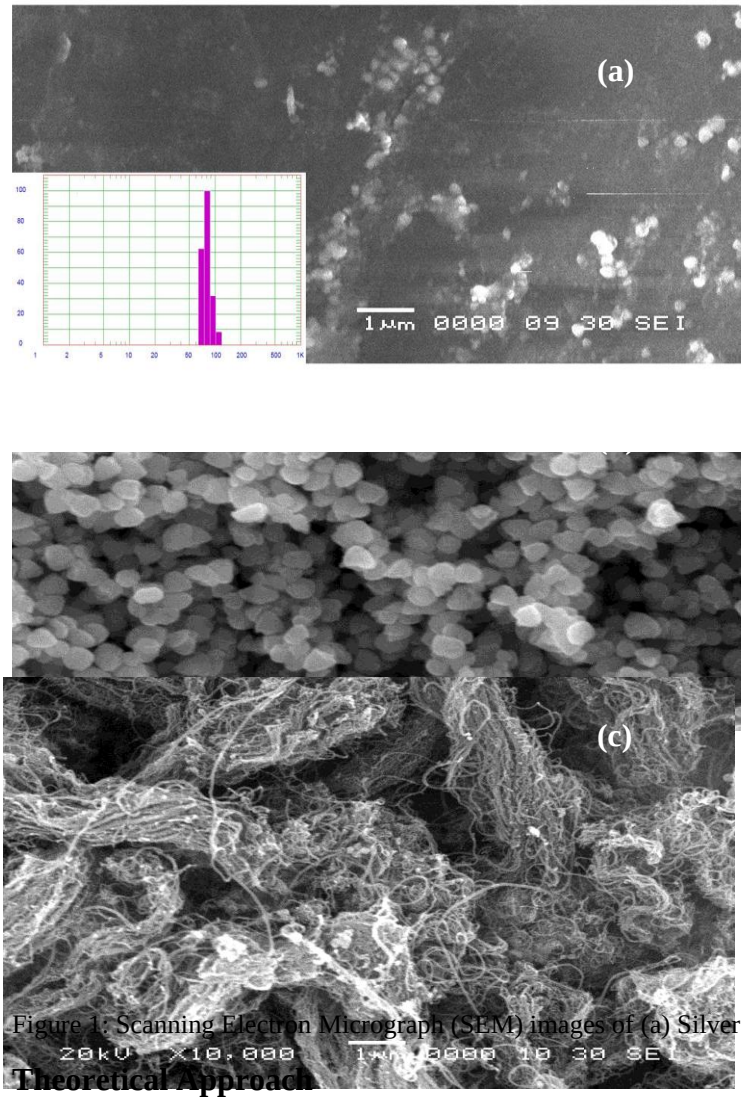

Figure 1: Scanning Electron Micrograph (SEM) images of (a) Silver NPs (b) ZnO NPs (c) CNTs.

Theoretical Approach

Stationary or static mode:

Static thermal conductivity of NFs obeys Maxwell model [19]. The Maxwell model for effective thermal conductivity of solid–liquid mixtures is given for micro or millimeter sized particles suspended in base fluids.

$$\lambda_{eff} = \frac{\lambda_p + 2\lambda_{bf} + 2(\lambda_p - \lambda_{bf})\phi}{\lambda_p + 2\lambda_{bf} - (\lambda_p - \lambda_{bf})\phi}\lambda_{bf} \qquad (1)$$

where λ_{eff} is the thermal conductivities of the solid–liquid mixture. Maxwell's model is good for spherical shaped particles with low particle volume concentrations. Hamilton and crosser modified Maxwell's model by incorporating shape factor to account for the effect of the shape of particles [20]. The ETC of the NF is given as

$$\lambda_{eff} = \frac{\lambda_p + (n-1)\lambda_{bf} - (n-1)\phi(\lambda_{bf} - \lambda_p)}{\lambda_p + (n-1)\lambda_{bf} + \phi(\lambda_{bf} - \lambda_p)}\lambda_{bf} \quad (2)$$

Where n is the empirical shape factor given by 3/ψ, and ψ is the particle sphericity, defined as surface area of a sphere (with the same volume as the given particle) to the surface area of the particle. For spherical particle, the value of n is 3. In the above model, if the particles in fluid are cylindrical, just like CNTs, λ_{eff} can be calculated by taking n=6, $\lambda_P = \lambda_{CNT}$ and ϕ is the volume fraction of CNTs in fluid [21].

Brownian motion induced nanoconvection mode

A theoretical model has been proposed by Jang and Choi [22] that involves four modes contributing to the energy transfer resulting in enhancement of thermal conductivity of NFs [22]. The first mode is collision between base fluid molecules, the second mode is the thermal diffusion in nanoparticles, the third mode is the collision of nanoparticles with each other due to the Brownian motion, and the fourth mode is collision between base fluid molecules and nanoparticles by thermally induced fluctuations. Considering the all the above four modes, the ETC of NF is given as

$$\lambda_{nf} = \lambda_{bf}(1-\phi) + \beta_1\lambda_p\phi + C_1\frac{d_{bf}}{d_p}\lambda_{bf}\,\mathrm{Re}_{dp}^2\,\mathrm{Pr}\,\phi \quad (3)$$

where $\beta_1 = 0.01$ is a constant for considering the Kapitza resistance per unit area; $C_1 = 18 \times 10^6$ is a proportionality constant; Pr is the Prandtl number is defined by $\mathrm{Pr} = \frac{\mu_{bf}}{p_{bf}\alpha_{bf}}$ of the base fluid, and the Reynolds number is defined by $\mathrm{Re}_{d_p} = \frac{\left(\overline{C}_{R.M.}d_p\right)}{\nu}$ where $\overline{C}_{R.M.} = \frac{\kappa T}{3\pi\mu_{bf}d_p l_{bf}}$ is the random motion velocity of a nanoparticle and ν is the kinematic viscosity of base fluid. They recommend, for water-based NFs the equivalent diameter d_{bf} = 0.384 nm and mean-free path of water l_{bf} =0.738 nm at a temperature of 300 K. The overall thermal conductivity of NFs could be found by adding equations consisting static and dynamic parts.

$$\lambda_{eff} = \lambda_{static} + \lambda_{dynamic} \quad (4)$$

The model proposed by Koo and kleinstreuer is one among the existing models that predict the thermal conductivity of NFs based on Brownian motion [23]. This model was composed of two parts. One is referred to as the static part (λ_{static}) evaluated by mixture models, i.e. the Maxwell model and the other part ($\lambda_{dynamic}$) is attributed to the Brownian motion. According to this model the ETC of NFs given as

$$\lambda_{eff} = \frac{\lambda_p + 2\lambda_{bf} - 2(\lambda_{bf} - \lambda_p)\phi}{\lambda_p + 2\lambda_{bf} + (\lambda_{bf} - \lambda_p)\phi}\lambda_{bf} + 5\times10^4\,\beta\phi\rho_{bf}C_{pbf}\sqrt{\frac{\kappa T}{\rho_p d_p}}\,f(T,\phi) \quad (5)$$

Where β shows the fraction of the liquid volume which travels with a particle and decreases with the particle concentration because of the viscous effect of moving particles. β is a function of the volume fraction ϕ of nanoparticles, which is given by

$$\beta = 0.0137(100\phi)^{-0.8229} \quad \text{for } \phi<0.01 \tag{6}$$

$$\text{And} \quad \beta = 0.0011(100\phi)^{-0.7272} \quad \text{for } \phi>0.01 \tag{7}$$

The function f (T, ϕ) is given by

$$f(T,\phi) = (-6.04\phi + 0.4705)T + (1722.3\phi - 134.63) \tag{8}$$

Which is valid for 0.01<Φ<0.04 and 300 K<T<325 K.

New empirical correlations were derived by Das et al [24] from a broader set of experimental data derived from three NFs.
Where,

$$f(T,\varphi) = (2.8217\times10^{-2}\phi + 3.917\times10^{3})\left(\frac{T}{T_0}\right) + (-3.0669\times10^{-2}\phi - 3.91123\times10^{-3}) \tag{9}$$

$$\text{And} \qquad \beta = 8.4407\times(100\phi)^{-1.07304} \tag{10}$$

$$\beta = 9.881\times(100\phi)^{-0.9446} \tag{11}$$

for ZnO and CuO based NFs respectively.

Chon et al. [25] proposed an empirical correlation based upon experimental data for the thermal conductivity of Al_2O_3 NF using Buckingham-Pi theorem with a linear regression scheme. They showed that the Brownian motion of the suspended nanoparticle is the most important factor in the enhancement of thermal conductivity of NFs. The correlation is given as

$$\frac{\lambda_{eff}}{\lambda_{bf}} = 1 + 64.7\,\mathrm{Re}^{1.2321}(\mathrm{Pr})^{0.9955}\left(\frac{d_{bf}}{d_p}\right)^{0.3690}\left(\frac{\lambda_p}{\lambda_{bf}}\right)^{0.7476}(\phi)^{0.7460} \tag{12}$$

where d_{bf} is the molecular diameter of the base fluid; $\mathrm{Pr} = \dfrac{\mu_{bf}}{p_{bf}\alpha_{bf}}$ is the Prandtl number of the base fluid and $\mathrm{Re} = \dfrac{(\rho_{bf}\kappa T)}{(3\pi\mu_{bf}^2 l_{bf})}$ is the Reynolds number; l_{bf} is the mean-free path for the base fluid.

Prasher et al. [26] proposed the multi-sphere Brownian model (MSBM) to predict the enhancement in the thermal conductivity of NFs is primarily due to the convection caused by the Brownian motion of the nanoparticles. They introduced a convective–conductive model, which is a combination of Maxwell–Garnett conduction model and the convection caused by the Brownian motion of suspended nanoparticles.

$$\frac{\lambda_{nf}}{\lambda_{bf}} = 1 + A\mathrm{Re}^{m}(\mathrm{Pr})^{0.333}\phi\left(\frac{\left[\lambda_p(1+2\alpha)+2\lambda_m\right]+2\phi\left[\lambda_p(1-2\alpha)-\lambda_m\right]}{\left[\lambda_p(1+2\alpha)+2\lambda_m\right]-\phi\left[\lambda_p(1-\alpha)-\lambda_m\right]}\right) \tag{13}$$

where the coefficient $A = 4 \times 10^4$; m = 2.5 ± (15% of 2.5) for water based NFs, m = 1.6 ± (15% of 1.6) for EG-based nanofluids and m = 1.05 ± (15% of 1.05) for oil-based nanofluids; $\lambda_m = \lambda_{bf}\left[1+\left(\frac{1}{4}\right)\mathrm{Re}.\mathrm{Pr}\right]$ is the matrix conductivity; $\mathrm{Re} = \frac{1}{\nu}\sqrt{\frac{18\kappa T}{\pi\rho_p d_p}}$ is the Brownian–Reynolds number; $\alpha = 2R_b\lambda_m/d_p$ is the nanoparticle Biot number; R_b is the interfacial thermal resistance between nanoparticles and different fluids; ν is the kinematic viscosity and Pr is the Prandtl number of the base fluid.

Another model based upon regression analysis is used to predict temperature dependent ETC enhancement in NFs [27]

$$\frac{\lambda_{eff}}{\lambda_f} = 1 + 4.4\,\mathrm{Re}^{0.4}\left(\mathrm{Pr}\right)^{0.66}\left(\frac{T}{T_{fr}}\right)^{10}\left(\frac{\lambda_s}{\lambda_f}\right)^{0.03}\left(f_{eff}\right)^{0.66} \tag{14}$$

Following the work of Corcione [27], he developed an ETC enhancement model based upon regression analysis. The correlation proposed based upon 11-12 data sets of thermal conductivity of NFs mainly containing TiO_2, Al_2O_3 and CuO nanoparticles. The nanoparticle volume fractions are in the range from 0.002 to 0.09 whereas temperature lies from 294 K to 324 K. The effective thermal conductivity enhancement of NF is given by equation is a function of Reynolds number, Prandlts number and effective volume fraction.

Model applied

For nonspherical inclusions, the differential effective medium theory gives [18],

Static part: k_{static}

$$\left[\left(\frac{K_m}{K_e}\right)^{\frac{3A}{D}}\left(\frac{K_m+S_+}{K_e+S_+}\right)^{3C_+}\left(\frac{K_m+S_-}{K_e+S_-}\right)^{3C_-} - f + 1\right] = 0 \tag{15}$$

where S_{+-}, C_{+-}, A and D are constants.

From the Jang and Choi model, the Brownian term of diffusion can be written as

Dynamic part: $k_{dynamic}$

$$3C_1\frac{d_{bf}}{d_e}K_{bf}\,\mathrm{Re}_{d_{nano}}^2\,\mathrm{Pr}\,f \tag{16}$$

where C_1 is empirical constant. d_{bf}, d_e are diameters of base fluid and nanotube respectively. K_{bf} is thermal conductivity of base fluid. $\mathrm{Re}_{d_{nano}}$, Pr is Reynolds and Prandlts numbers. f is the volume fraction of CNTs.

For CNTs the diffusion coefficient for semi dilute suspensions is given by [18]

$$D_0 = \frac{3k_bT\left(\ln\left(\frac{L}{d}\right)-\gamma\right)}{\pi\eta_m L^3} \tag{17}$$

where k_b is the Boltzmann constant, γ is a constant (~0.8), η_m is the viscosity of the solvent.

We have performed numerical simulations applying bisection algorithm to solve static interfacial resistance term with diameter of base fluid molecule and CNT, d_{bf} = 2.75×10^{-10} m,

d = 2×10^{-8} m, length of CNTs L =15×10^{-6} m, mean free path length l_{bf} =2×10^{-8} m. Pr evaluated as $\Pr = \eta_m / \alpha$.

The total ETC enhancement was calculated as $k_{eff} = k_{static} + k_{dynamic}$.

The combination of the static terms with Brownian dynamic terms when used to model surfactant doped CNT NFs leads to simple expressions that can be used to fit the experimental data and find k_{eff}.

Results and discussion

Figure 2 depicts a comparison of the new model (volume fraction term replaced with dispersion effectiveness term) with experimental data for CNT-water NFs at different temperatures.

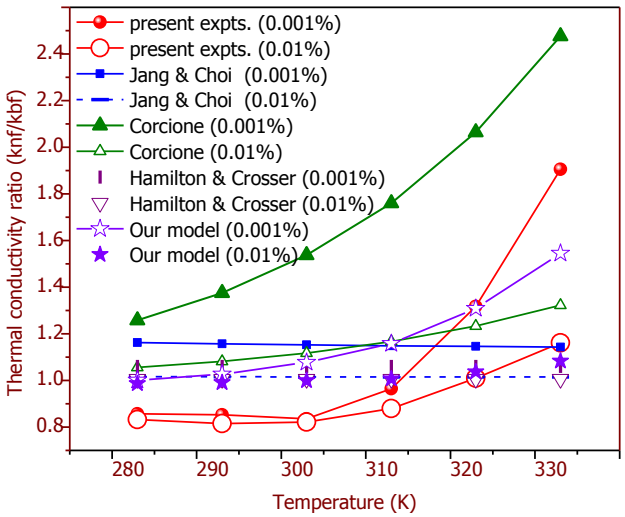

Figure 2: Comparison between theoretical models and experimental data on thermal conductivity for CNT/water NFs of 0.01% and 0.001% particle weight fraction.

Both NFs shows enhancement below one for temperature 313 K. However, above 313 K new model shows a good agreement with experimental data as compared to other models (HC and Jang [21]). The model by Corcione et al [27] over predicts the thermal conductivity enhancement values (Table 1).

T (^{0}K)	0.001 %	0.01 %	Our (0.001 %)	Our (0.01 %)	Jang (0.001 %)	Jang (0.01 %)	Corcion e (0.001 %)	Corcion e (0.01 %)	Hamilto n (0.001 %)	Hamilto n (0.01 %)	% d (0.001%)	% d (0.01%)
28 3	0.8565 5	0.8320 7	1.0013 4	0.9856 1	1.0162 6	1.0162 6	1.05639	1.25776	1.006	1.0605	14.4596 1	15.5786 4
29 3	0.8522 7	0.8151 7	1.0270 1	0.9898	1.0157 6	1.0157 6	1.08202	1.37488	1.006	1.0605	17.0145 4	17.6427 8
30 3	0.8357 2	0.8212 5	1.0771 8	0.9987 8	1.0153 4	1.0153 4	1.11756	1.53736	1.00599	1.06049	22.4165 3	17.7742 7
31 3	0.9646 3	0.8796 2	1.1582 2	1.0068 8	1.0150 3	1.0150 3	1.16643	1.76071	1.00599	1.06049	16.7140 5	12.6394 2
32 3	1.3174 8	1.0101	1.3085 8	1.0363 3	1.0148 5	1.0148 5	1.23299	2.06499	1.00599	1.06049	0.68039	-2.53088
33 3	1.9055 5	1.1615 5	1.5448 3	1.0824 7	1.0147 9	1.0147 9	1.32296	2.47622	1.00599	1.06049	23.3497 6	7.30547

Table 1: Thermal conductivity values for CNT based NFs

In Figure 3 various models are compared with experimental data for ZnO/water based NFs at different temperatures. Both the Chon model and Prasher model showed good agreement with experimental results. The model by Das et al, Corcione and Maxwell over predicts the enhancement in thermal conductivity (Table 2).

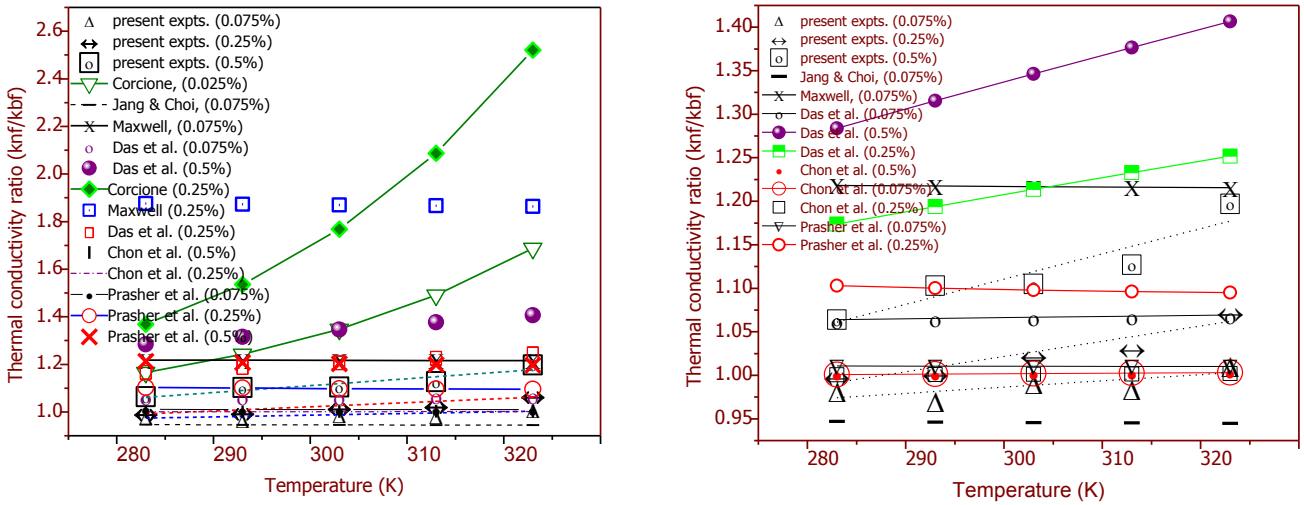

Figure 3: Comparison between theoretical models and experimental data on thermal conductivity for ZnO/water based NFs

T (^{0}K)	Present expts. (0.075%)	Present expts. (0.25%)	Present expts. (0.5%)	Corcione, (0.075%)	Corcione, (0.5%)	Jang & Choi, (0.075%)	Maxwell, (0.5%)	Das et al. (0.075%)	Das et al (0.5%)	Chon (0.075%	Chon (0.5%)	Prasher (0.5%)
283	0.983	1.0005	1.064	1.16632	1.58174	0.94699	3.47538	1.06517	1.28367	1.00022	1.000925	1.21324
293	0.971	1.004	1.103	1.24189	1.84607	0.94632	3.46122	1.0737	1.31553	1.00033	1.001344	1.20726
303	0.992	1.024	1.105	1.34673	2.21276	0.94574	3.44826	1.0819	1.34643	1.00045	1.001858	1.20237
313	0.985	1.032	1.127	1.49085	2.71684	0.94526	3.43684	1.09009	1.37669	1.0006	1.002475	1.19869
323	1.012	1.074	1.197	1.68719	3.40356	0.94487	3.42708	1.09806	1.40661	1.00078	1.003207	1.19624

Table 2: Thermal conductivity values for ZnO based NFs.

For silver nanofluid the model by Maxwell and Prasher matches with the experimental data below 303 K but fails to predict the thermal conductivity enhancement above and at 303 K (Figure 4). The model by Chon and Corcione over predicts the enhancement data [25, 27].

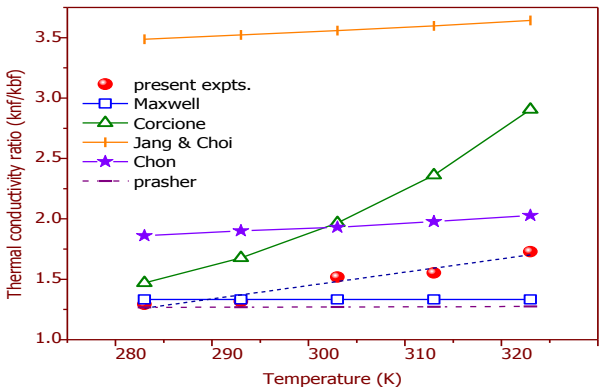

Figure 4: Comparison between theoretical models and experimental data on thermal conductivity for Silver NF of 0.1% particle weight fraction.

For Silver NF the model by Maxwell and Prasher matches with the experimental data below 303 K but fails to predict the thermal conductivity enhancement above and at 303 K (Figure 4). The model by Chon and Corcione over predicts the enhancement data [25,27].

Conclusion

The obtained data for thermal conductivity reveals that the prepared NFs were more effective above room temperature. The most effective and stable dispersion of NFs are of those which have concentration of CNTs of the order of 0.001 wt.%. Theoretical interfacial resistance model has to be extended to take effect of temperature dependency and Brownian motion. The classical models are inadequate to explain the anomalous increase in the effective thermal conductivity of NFs. Therefore, there is a need to further develop the effective thermal conductivity model, which encompasses all the prepared NFs with different variety of nanoparticles of different shape.

Acknowledgement

The V.S.R. is thankful to Dr. Vijay M. Sarode, Principal, G. M. Vedak College of Science, Tala for his valuable guidance during this research work.

References

[1] Eastman, J., Choi, S., Li, S., Yu, W., and Thompson, L., 'Anomalously increased effective thermal conductivities of ethylene glycol-based nanofluids containing copper nanoparticles,' Applied Physics Letters, Vol. 78, No. 6, 2001, pp. 718–720.

[2] Das, S., 'Nanofluids - The cooling medium of the future,' Heat Transfer Engineering, Vol. 27, No. 10, 2006, pp. 1–2.

[3] Hosseini, M. and Ghader, S., 'A model for temperature and particle volume fraction effect on nanofluid viscosity,' Journal of Molecular Liquids, Vol. 153, No. 2-3, 2010, pp. 139–145.

[4] Li, C.H., P. G., 'Experimental investigation of temperature and volume fraction variations on the effective thermal conductivity of nanoparticle suspensions (nanofluids),' Journal of Applied Physics, Vol. 99, No. 8, 2006,

[5] Jang, S., Lee, J. H., Hwang, K., and Choi, S., 'Particle concentration and tube size dependence of viscosities of Al_2O_3 water nanofluids flowing through micro- and minitubes,' Applied Physics Letters, Vol. 91, No. 24, 2007,

[6] Zhang, X., Gu, H., and Fujii, M., 'Effective thermal conductivity and thermal diffusivity of nanofluids containing spherical and cylindrical nanoparticles,' Journal of Applied Physics, Vol. 100, No. 4, 2006,

[7] Gharagozloo, P., Eaton, J., and Goodson, K., 'Diffusion, aggregation, and the thermal conductivity of nanofluids,' Applied Physics Letters, Vol. 93, No. 10, 2008.

[8] V.S. Raykar, A. K. Singh, Photoacoustic method for measurement of thermal effusivity of Fe_3O_4 nanofluid,J. of Thermodynamics, 464368, (2011).

[9] Cherkasova, A. and Shan, J., 'Thermal conductivity enhancement of nanofluids,' Carbon Nanotubes, Vol. 222, 2006, pp. 235–237

[10] Xie, H., Lee, H., Youn, W., and Choi, M., 'Nanofluids containing multiwalled carbon nanotubes and their enhanced thermal conductivities,' Journal of Applied Physics, Vol. 94, No. 8, 2003, pp. 4967–4971

[11] Murshed, S., Leong, K., and Yang, C., 'A combined model for the effective thermal conductivity of nanofluids,' Applied Thermal Engineering, Vol. 29, No. 11-12, 2009, pp. 2477–2483.

[12] Hasselman, D. P. H. and Johnson, L. F., 'Effective Thermal Conductivity of Composites with Interfacial Thermal Barrier Resistance,' Journal of Composite Materials, Vol. 21, 1987, pp. 508–515.

[13] Gao, L. and Zhou, X., 'Differential effective medium theory for thermal conductivity in nanofluids,'Physics Letters, Section A: General, Atomic and Solid State Physics, Vol. 348, No. 3-6,2006, pp. 355–360.
[14] Bandyopadhyaya, R., Nativ Roth, E., Regev, O., and Yerushalmi Rozen, R.,Stabilization of Individual Carbon Nanotubes in Aqueous Solutions,' Nano Letters, Vol. 2, No. 1, 2002, pp. 25–28.
[15] Ding, Y., Alias, H., Wen, D., and Williams, R., 'Heat transfer of aqueous suspensions of carbon nanotubes (CNT nanofluids),' International Journal of Heat and Mass Transfer, Vol. 49, No. 1-2, 2006, pp. 240–250.
[16] A. K. Singh, V. S. Raykar, Microwave synthesis of silver nanofluids with polyvinylpyrrolidone (PVP) and their transport properties, Colloid Polym. Sci., 286, no. 14-15 (2008), p. 1167.
[17] V.S. Raykar, A. K. Singh, Thermal and rheological behavior of acetylacetone stabilized ZnO nanofluids, Thermochim. Acta., 502, no. 6 (2010), p. 60.
[18] V.S. Raykar, A. K. Singh, Dispersibility dependence of thermal conductivity of carbon nanotube based nanofluids, Phys. Lett. A, 374, no. 45 (2010), p. 4618.
[19] Maxwell, J. C., Treatise on Electricity and Magnetism, Vol. Claredon Press, 1873, pp. Oxford, U. K.
[20] Hamilton, R. and Crosser, O., 'Thermal conductivity of heterogeneous two component systems,' I and EC Fundamentals, Vol. 125, 1962, pp. 187.
[21] Jiang, W., D. G. P. H., 'Measurement and model on thermal conductivities of carbon nanotube nanorefrigerants,' International Journal of Thermal Sciences, Vol. 48, No. 6, 2009, pp. 1108– 1115.
[22] Jang, S. and Choi, S., 'Role of Brownian motion in the enhanced thermal conductivity of nanofluids,'Applied Physics Letters, Vol. 84, No. 21, 2004, pp. 4316–4318.
[23] Koo, J., K. C., 'A new thermal conductivity model for nanofluids,' Journal of Nanoparticle Research, Vol. 6, No. 6, 2004, pp. 577–588.
[24] Vajjha, R.S.and Das, D., 'Experimental determination of thermal conductivity of three nanofluids and development of new correlations,' International Journal of Heat and Mass Transfer, Vol. 52, No. 21-22, 2009, pp. 4675–4682.
[25] Chon, C., Kihm, K., Lee, S., and Choi, S., 'Empirical correlation finding the role of temperature and particle size for nanofluid (Al2O3) thermal conductivity enhancement,' Applied Physics Letters, Vol. 87, No. 15, 2005, pp. 1–3.
[26] Bhattacharya, P., Saha, S., Yadav, A., Phelan, P., and Prasher, R., 'Brownian dynamics simulation to determine the effective thermal conductivity of nanofluids,' Journal of Applied Physics, Vol. 95, No. 11 I, 2004, pp. 6492–6494.
[27] Corcione, M., 'Heat transfer features of buoyancy-driven nanofluids inside rectangular enclosures differentially heated at the sidewalls,' International Journal of Thermal Sciences, Vol. 49, No. 9, 2010, pp. 1536–1546.

Paper-15

Plant mediated biosynthesis, characterization and antioxidant activity of silver and copper nanoparticles employing root extract of Cyperus pertenuis

H.S.Koli [1], B.B.Bahule [2] and Khursheed Ahmed [1]
1. Department of Chemistry, Abeda Inamdar College,
2. Department of Chemistry, Nowrosjee Wadia College,
Affiliated to Savitribai Phule Pune University, Pune India

Abstract- In the present paper, we are reporting a biosynthesis of silver and copper nanoparticles using a root extract of Cyperus pertenuis plant. The dried roots of this plant are powdered and an aqueous extract was prepared. The root extract thus prepared has been used for the preparation of silver and copper nanoparticles from silver nitrate and copper sulphate respectively. The silver and copper ions have been successfully reduced to their corresponding metals in high yield. The roots of this plant has medicinal value and are useful in the treatment of various ailments. The root extract is useful in the treatment of fatigue, chest disorder, fevers, haemorrhoids, nasal discharge, eye sores, antimalerial and anti-inflammatory agent. The alkaloids, flavonoids, phenols, tannins, steroids and essential oils can act as a natural source for reducing and capping agent in stable nanoparticles synthesis. The biosynthesised nanoparticles have been characterised by UV-Visible, FTIR, XRD, FESEM techniques. The antioxidant activity of these nanoparticles is also determined by DPPH method.

Keywords: nanoparticles, root extract, bioreduction, green synthesis, antioxidant activity

Introduction

Nanotechnology is a fast growing innovative technology for manipulation, creation and application of nanomaterials. Being at the transition between bulk materials and atomic or molecular structures, they often exhibit phenomena that are not observed at either scale [1] Metallic nanoparticles are of great interest due to their excellent physical and chemical properties such as high surface-to-volume ratio and heat transfer (thermal conductivity) These unique properties of nanoparticles allows heat, molecules and ions to diffuse into the particles in a very short time which can make the particles very reactive or catalytic [2]. And thus the nanomaterials finds an enormous range of potential applications in different walks of life such as medicine, environment [6], food processing, agriculture[7],electronic, sensing devices, biomolecular detection, pharmacy, textile sizing, optoelectronics, biomedical products, catalysis, energy, electrochemical products[8] and so on. Potential of Nanotechnology is immense and encompasses virtually every field of life [3]. Hence the nanomaterials have attracted huge interest as a rapidly innovating and developing class of materials. It has the combination of new ideas and knowledge from various research fields like physics, material science, chemistry, biotechnology, engineering, medicine etc.[3] Current chemical and physical methods which frequently utilize environmentally corrosive agents for metal nanoparticles synthesis are not only dangerous to environment but costly too[13]. So, in the field of nanotechnology, development of rapid, simple, cost-effective, and eco-friendly procedures for the synthesis of nanoparticles is worth [4]. Several biological methods are suggested which involve the use of environmentally benign materials like bacteria, fungi, yeast, enzymes, plants or various parts of plant extracts have been reported to possess high bioreductive ability to synthesise various metal nanoparticles. An eco-friendly plant mediated synthesis of nanoparticles is a fast growing research in the field of nanotechnology [5] whereas harmful chemicals, high temperature, energy and pressure are excluded. The biomolecules present in plant play a vital role in reduction of metal ions. Using herbal plants is advantageous, as their medicinal properties are added to the nanoparticles during the synthesis, offering numerous benefits of compatibility for pharmaceutical and biomedical applications [9]. Different parameters such as surface area, particle size and surface reactivity determine the cytotoxicity of biosynthesized nanoparticles.[2] The advancement of "green chemistry" approach over chemical and physical methods are easy to control the reaction process, high production rate, cost effectiveness and environmentally friendly nature. The biosynthesised nanoparticles are non-toxic, more stable and more uniform in size than the counterparts prepared by the traditional method and also exhibit distinct chemical, physical and biological applications in various areas of science and technology. Thus green preparation methods have become a hotspot in the field of nanoparticles synthesis [6].

In the present study, a simple, rapid and ecofriendly biosynthetic method using root extract of herbal plant Cyperus pertenuis has been carried out at lower temperature for producing silver and copper nanoparticles The synthetic method adopted here is advantageous over chemical and physical procedures as it is a resource efficient, non toxic, cost effective method and it provides a single-step technique for the biosynthesis process [10]. It does not require any specific isolation and maintenance procedures which are needed in bacteria, fungi or algae based nanoparticles [5]. Cyperus pertenuis is a perennial, grass-like plant, belongs to family Cyperacae, growing in northeast India, Bangladesh and Myanmar. The root of Cyperus pertenuis is considered to be useful in the treatment of fatigue, flatulence, thirst relief, diarrhoea, chest disorders, fevers, haemorrhoids, nasal discharge, eye sores, also used in perfumery, cosmetics and as an antidote for scorpion stings, antimalarial, anti-inflammatory[15]. Phytochemical profile of Cyperus pertenuis revealed the presence of alkaloids, flavonoids, glycosides, phenols, tannins, steroids, essential oils and many novel sesquiterpenoids which can act as a natural source for reducing and capping agent in stable nanoparticles synthesis reaction which eliminates multistep synthesis practice problems and costs of chemical reagents[14]. The bioactive phytochemicals present in the root extract of Cyperus pertenuis may be accountable for significant remarkable antioxidant activity of green synthesized nanoparticles while determining their different pharmacological properties [11]. Antioxidants may be for great benefit in improving the quality of life by preventing or postponing the onset of degenerative diseases [17]. This present study was attempted to find out the antioxidant activity along with IC_{50} values of metal nanoparticles, synthesised ecofriendly by using Cyperus pertenuis root extract as a reducing agent against the 2, 2-diphenyl-1-picrylhydrazyl (DPPH) free radical.

Materials and Methods

Materials

Silver nitrate($AgNO_3$), Copper sulphate ($CuSO_4.5H_2O$), Ascorbic acid, DPPH and dimethyl sulfoxide (DMSO) were used in this scheme. Aqueous extract was prepared by using powdered dried roots of Cyperus pertenuis plant. All the chemicals used were of analytical grade with 99% purity and used as it is without further purification. All the solutions were freshly prepared using deionised water. All glasswares used in the process, were washed with double distilled water and acetone and dried before use.

Preparation of extract from roots of Cyperus pertenuis

The extract was prepared by taking 4 gm of powdered dried roots of Cyperus pertenuis in a250-mL Erlenmeyer flask with 100 mL of deionised water and the mixture was heated at 70^0C at 1500 rpm for 45 min. by using magnetic heating stirrer. The extract thus obtained was filtered through Whatman paper no.41 and the resulting filtrate (extract) was used for the synthesis of metal nanoparticles.

Preparation of silver nitrate and copper sulphate solutions

Aqueous solution of 10,000 ppm of $AgNO_3$ is prepared by dissolving 1 gm of Silver nitrate in 100 mL deionised water. In the same way aqueous solution of 10,000 ppm of Copper sulphate $CuSO_4.5H_2O$ is prepared.

Green synthesis of silver and copper Nanoparticles

The synthesis of silver nanoparticles was carried out by adding slowly 3 mL aqueous extract from roots of Cyperus pertenuis to 50 mL solution of aq. silver nitrate along with constant stirring at room temperature. Within few seconds the colourless reaction mixture turned to light brown and after 15 minutes the solution became dark and after 24 hrs. there is no any change in colour of the reaction mixture(Fig.1b,1c).

The green synthesis of copper nanoparticles was carried out by preparing the reaction mixture with 50 mL aqueous solution of copper sulphate and 3 ml aqueous extract from roots of Cyperus pertenuis. The colour of the reaction mixture was changed from light blue to green within 10 minutes with constant stirring at 60^0C. After 20 minutes the green colour became dark and it remained as it is after 24 hrs. (Fig.1d,1e).

(a) (b) (c) (d) (e)

Fig.1. (a) aq. solution of extract from roots of Cyperus pertenuis (b) aq. solution of silver nitrate (c) solution containing silver nanoparticles (d) aq. solution of copper sulphate (e) solution containing copper nanoparticles

Isolation of synthesised metal nanoparticles

The aqueous solutions containing the signatory colours of silver and copper nanoparticles were transferred in two separate petri dishes by pouring and left in an oven for drying at 250^{o}C for 24 hrs. Decomposition of organic matters and evaporation of moisture and impurities resulted in completely dried powder of Ag and Cu nanoparticles.

Characterization

The biosynthesised Ag and Cu nanoparticles were subjected to various characterisation techniques which helped us to understand their specific properties such as crystal structure, particle size distribution, functional groups studies, elemental composition, crystallinity, optical properties and a variety of other other basic features of nanoparticles[12]. These techniques were helpful to verify the utility of our method, leading to a better understanding of nanoscale properties and their interactions within these advanced materials.

The absorbance spectra of green synthesised Ag and Cu nanoparticles were measured by using UV-Visible double beam spectrophotometer, operated at a resolution of 1 nm and an electromagnetic wavelength within the range from 200 to 800 nm. Fourier transform infrared (FTIR) spectroscopy measurements are usually performed to identify and classify probable biomolecules that can be reliable for capping, leading to proficient stabilization of nanoparticles. FTIR spectra were investigated using the FTIR spectrometer at a spectrum wavelength in the range of 4000 to 500 cm^{-1} with a resolution of 4 cm^{-1} based on KBr pellet technique. The phase identification and crystalline structure of biosynthesised metal nanoparticles were determined by powder X-ray diffractometer (XRD) using CuKα radiation (λ = 1.5406 A^{o}) Low angle diffract grams were recorded in the 2θ range 20^{o} - 80°. Field Emission Scanning Electron Microscopy (FESEM) is another technique used to characterize the morphology of nanoparticles through direct visualization. This method is based on electron microscopy and offers several advantages for morphological and size analysis.

UV-Visible spectroscopy

Bioreduction of metal ions to metal nanoparticles were determined by recording UV-Visible spectrum of the reaction mixture after diluting a small aliquot of the sample with deionised water. The measurements are recorded on UV–visible double beam spectrophotometer at resolution of 1nm.(Fig.2)

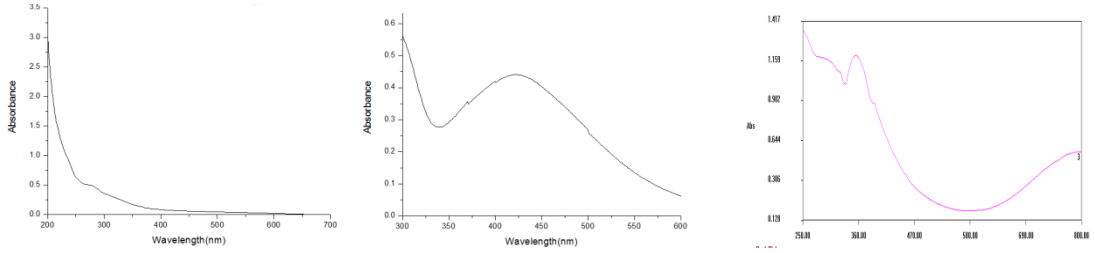

(a) (b) (c)

Fig.2. UV-Vis absorption spectrum of (a) Cyperus pertenuis root extract (b) silver nanoparticles (c) copper nanoparticles

The absorption of green synthesised Ag and Cu nanoparticles were observed near 422 nm and 353 nm respectively in the UV–Vis spectra which is due to surface plasmon resonance of synthesised nanoparticles, conforming the eco-friendly synthesis of stable metal nanoparticles.

FT-IR analysis

FT-IR analysis of root extract of Cyperus pertenuis as well as green synthesised nanoparticles are as shown in Fig.3

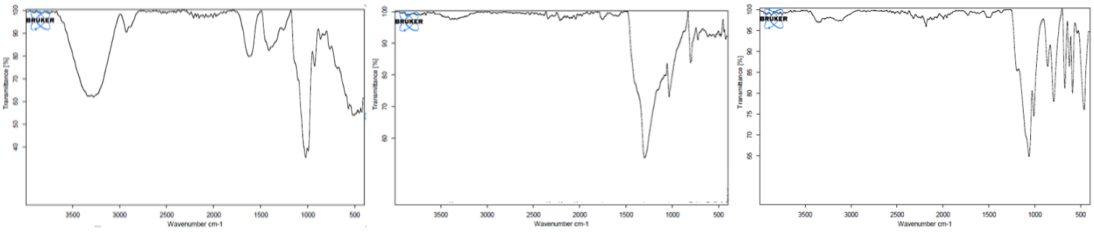

(a) (b) (c)

Fig.3. FT-IR spectrum of(a) Cyperus pertenuis root extract (b) Silver nanoparticles (c) Copper nanoparticles

There are small changes in the intensity and wavenumber at the maximum peak of the FTIR spectra of Cyperus pertenuis root extract and synthesised nanoparticles. The strong band at 3276.39 cm^{-1} correlated to alcoholic or phenolic –OH stretching vibration contained in the FTIR spectrum of root extract has been shifted to 3432.16 cm^{-1} for Ag and 3102.72 cm^{-1} for Cu nanoparticles, apparently because of protein binding. The medium-intensity peak at 1626.46 cm^{-1} assigning conjugated carbonyl (C=O) stretching vibration or aromatic ring C=C stretching vibration appearing in the root extract is disappeared from IR spectrum of synthesized nanoparticles. Also the IR frequency of root extract at 1312.32 cm^{-1} denoting C-O stretch due to aldehydes or phenols was shifted to a small peak at 1298.80 cm^{-1} in silver which is absent in Cu spectrum. The band at 1022.83 cm^{-1}, which is characteristic of glycoside or ether (C–O–C) groups in root extract, slightly shifted to 1034.62 for Ag and 1063.31 cm^{-1} for Cu nanoparticles. In addition, absorption peaks located at 724.42 and 794.37 cm^{-1} corresponded to the presence of alkanes, alkenes and aromatic rings in as synthesised nanoparticles. Stretching vibrational frequency due to metal-oxide bond appeared at 517.74 and 589.25 cm^{-1} in the spectra of root extract and Cu nanoparticles respectively.

X-ray diffraction studies

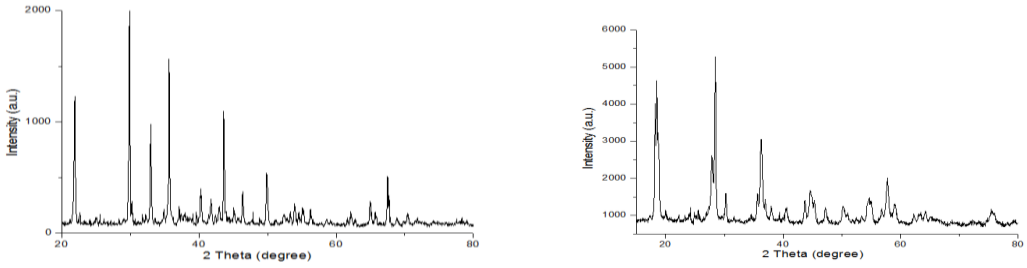

(a) (b)

Fig.4. The X-ray diffraction patterns obtained for (a) Ag nanoparticles (b) Cu nanoparticles

Ecofriendly synthesized silver nanoparticles when subjected to XRD analysis, gave a clear picture on the presence of major characteristic peaks at 2θ values of 20.89, 29.08, 32.98, 35.14, 40.32, 43.69, 46.02, 49.96, 62.00 degrees corresponding to the crystal plane (200), (220), (311), (222), (400), (331), (420), (422), (531) respectively (Fig.4a).

XRD spectrum obtained with as-synthesised copper nanoparticles showed different diffraction peaks at 2θ values of 18.05, 28.44, 30.26, 36.28, 43.76, 44.62, 47.89, 54.58, 57.76, 59.47 and 77.12 degrees corresponding to (101), (112), (200), (004), (220), (213), (204), (312), (224), (116) and (316) Miller indices respectively (Fig.4c).

The characteristic peaks in the XRD of green synthesised Ag and Cu nanoparticles indicates the crystallinity of as synthesised nanoparticles.

FESEM

The typical FESEM images at different magnification levels suggested further clear picture of surface morphology with variable size of biosynthesised Ag and Cu nanoparticles (Fig.5a &5b)

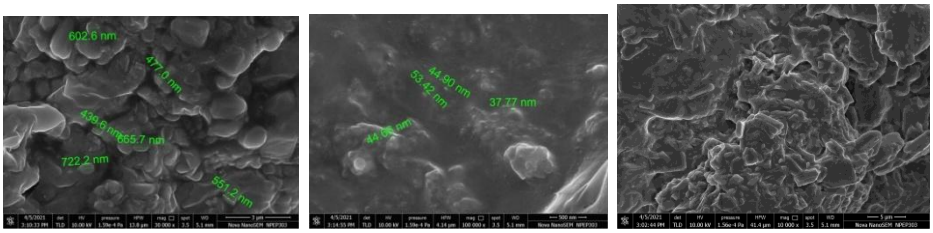

Fig.5a. FESEM images of silver nanoparticles at different magnification levels

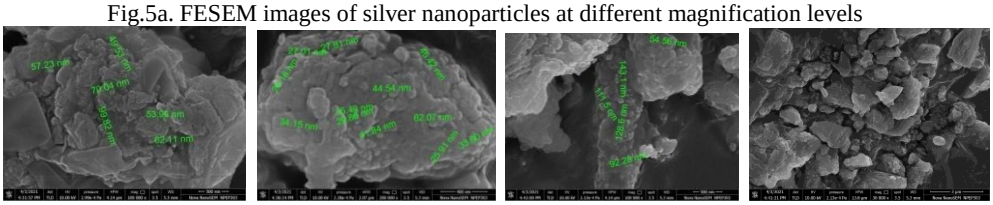

Fig.5b. FESEM images of copper nanoparticles at different magnification levels

Determination of antioxidant activity by DPPH method

The antioxidant property of biosynthesised nanoparticles were analyzed by 2, 2-diphenyl-1-Picrylhydrazyl (DPPH) free radical method [13]. The free radical scavenging activity of green synthesised Ag and Cu nanoparticles and that of standard ascorbic acid were determined using the stable radical DPPH. 3 ml of each of different concentrations (100, 200, 300, 400 and 500 µg/ml) of Ag and Cu nanoparticles were mixed with 2 ml freshly prepared DPPH solution. In the same way different aliquots of the ascorbic acid solutions corresponding to 100–500 µg/ml were used for calibration. Then all the solutions were incubated at room temperature in the dark for 30 min. The absorbance was recorded at 517 nm using UV-Visible spectrophotometer. Mixture of DPPH and DMSO was used as a control. The free radical scavenging activity which is expressed as the percentage of inhibition was determined by using following formula,

$$\text{Scavenging effect (\%)} = [\,(Ac - As)\,/\,Ac\,] \times 100$$

where, *Ac* is the absorbance of the control and *As* is the absorbance of the sample or standard. The result of different concentrations of biosynthesised silver and copper nanoparticles on DPPH radical scavenging activity is shown in Table no.1 The % inhibitions were plotted against concentrations and from the graph IC_{50} value was calculated (Fig.6). Antioxidant activity of green synthesized silver and copper nanoparticles against DPPH radical were assessed and compared with standard ascorbic acid.

Sample	% Inhibition at concentrations					IC_{50} µg/ml
	100 µg/ml	200 µg/ml	300 µg/ml	400 µg/ml	500 µg/ml	
Silver nanoparticles	20.75	25.01	42.19	53.74	55.96	211
Copper nanoparticles	3.33	3.68	10.09	25.29	28.07	323
Ascorbic acid	20.78	24.12	59.39	65.15	68.54	227

Table no.1: Profile of DPPH radical scavenging activity with IC_{50} values

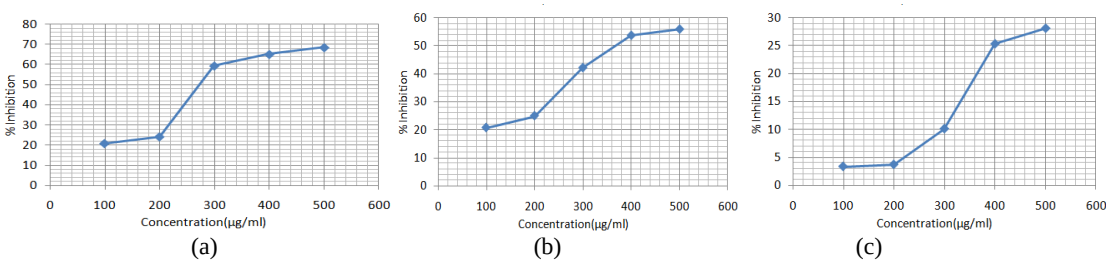

(a) (b) (c)

Fig.6. Graphical representation of antioxidant activity shown by (a) standard Ascorbic acid (b) silver nanoparticles and (c) copper nanoparticles

Result and discussion

The present synthesis of silver and copper nanoparticles was easy, convenient and high yielding. Herein, the mixing of aqueous root extracts of Cyperus pertenuis into the silver nitrate solution caused a change in colour of

the colourless silver nitrate solution to dark brown and in the same manner blue coloured copper sulphate solution turned green indicating the synthesis of Ag and Cu nanoparticles in the respective reaction mixtures (Fig.1) and the colours of both the reaction mixtures remain unchanged after 24hrs. The colour change of the reaction mixtures were ascribed to the excitation of surface plasmon vibrations indicating the formation of stable nanoparticles. Characteristically, root extract mediated Ag and Cu nanoparticles displayed the absorption peaks within UV-Vis range of wavelengths near 422 nm and 353 nm respectively in the UV–Visible spectra, validating the completion of reaction with synthesis of stable metal nanoparticles(Fig.2). The variations in the spectral positions of FTIR bands in root extract and phytosynthesised nanoparticles indicated presumably, hydroxyl, ether, aromatic and carbonyl groups of some active metabolites are present in the Cyperus pertenuis root extract that might be involved in the reduction of the metal ions and also responsible for capping and efficient stabilization of the bioreduced nanoparticles (Fig.3). The characteristic diffraction peaks in XRD patterns of ecofriendly synthesized silver and copper nanoparticles suggesting the crystalline nature of metal nanoparticles. The resulting diffraction patterns are compared with the standard patterns to get the final information, according to which the synthesised silver nanoparticles are face-centered cubic in nature while biosynthesised copper nanoparticles are having body-centered tetragonal geometry (Fig.4). XRD patterns clearly exhibited the presence of silver nanoparticles and copper nanoparticles with some unassigned peaks which may be of fewer bio compounds. FESEM images at different magnification levels revealed that the green synthesized silver nanoparticles and copper nanoparticles were aggregated with irregular spherical shapes. (Fig.5a &5b). Simply put, these images suggest that the particles agglomerate with irregular morphology. The average particles size of green synthesized silver and copper nanoparticles are found to be 363 nm and 58 nm respectively. The antioxidant activity of root extract mediated nanoparticles determined by using DPPH free radical are recognized to be due to the hydrogen or electron donating abilities of nanoparticles. The free radical scavenging activity of green synthesised nanoparticles tends to increase with increasing their concentration (Fig.6). Notably, antioxidant activity of Ag nanoparticles and Cu nanoparticles found to be 55.96%, 28.07% at 500 µg/ml respectively. However, the standard Ascorbic acid demonstrated 68.54% inhibition in the same concentration with the IC_{50} value of 227µg/ml. The DPPH potential of the synthesized Ag and Cu nanoparticles showed an IC_{50}values of 211µg/ml and 323µg/ml respectively. The results confirmed that as synthesised silver nanoparticles has stronger antioxidant activity than that of Copper nanoparticles.

Conclusions

An ecofriendly plant mediated synthesis of metal nanoparticles using aqueous root extract of Cyperus pertenuis is one of the more stable, rapid, economical, energy efficient and cost effective process whereas harmful chemicals, high temperature and pressure are not required. Based on the earlier observations, we may conclude that during the process of nanoparticles synthesis, the bioactive phytochemicals from the root extract adheres on the surface of metal nanoparticles as capping and stabilizing agents which might be responsible for effective and significant antioxidant potentiality of synthesised nanoparticles, offering numerous benefits of compatibility for their pharmaceutical and biomedical applications. Also the green approach for nanoparticles synthesis adopted here provides healthier work places and communities, protecting human health and environment leading to lesser waste and safer products.

Acknowledgements: The authors are thankful to the Principals of Nowrosjee Wadia College and Abeda Inamdar College for providing the necessary infrastructural support. Our sincere thanks are due to the Savitribai Phule Pune University for the assistance in recording the various spectra. We wish to thank the Head, Department of Chemistry, Abeda Inamdar College for the help and support in the execution of this experimental work.

References

1. K. Yokohama, D. R. Welchons, Nanotechnology 18 (2007) 105101-105107

2. Ali, M. Text Book of Pharmacognosy, Pune, 1996; 2nd ed: pp. 215-216;

3. M. Nishikimi, N.A. Rao, K. Yagi, Biochem. Biophys. Res. Commun. 46 (1972) 849-853.

4. Iravani, S.; Korbekandi, H.; Mirmohammadi, S.V.; Zolfaghari, B. Synthesis of silver nanoparticles: Chemical, physical and biological methods. Res. Pharm. Sci. 2014, 9, 385-406.

5. Singh, P., Kim, Y.J., Zhang, D.; Yang, D.C. Biological synthesis of nanoparticles from plants and microorganisms. Trends Biotechnol. 2016, 34, 588-599.

6. Omowunmi, A. Sadik, Environ. Sci. Processes Impacts, 2013, 15, 19-20

7. B. Kumar, K. Smita, et al., in: S. Ranjan, et al. (Eds.), Nanoscience in Food and Agriculture Sustainable Agriculture Reviews, Volume 2, chapter 7 Springer International Publishing, Switzerland, 2016, pp. 235-252. chapter 7.

8. Didier Astruc, Chem. Rev., 2020, 120(2), 461-463

9 C. Jacobs, R.H. Muller, Pharmaceut. Res. 19 (2002) 189-194

10. J.R. Peralta-Videa, Y. Huang, J.G. Parsons, L. Zhao, L. Lopez-Moreno, J.A. Hernandez-Viezcas, J.L. Gardea-Torresdey, Plant-based green synthesis of metallic nanoparticles: scientific curiosity or a realistic alternative to chemical synthesis? Nanotechnol. Environ. Eng.1 (2016) 4.

11. Yamamoto O., M. Komatso, Jun Sawai and Zenbe-E-Nakagawa, 2004. Journal Materials science: Materials in Medicine, 15: 847-851.

12. Dhas,N.A.; Raj, C.P.; Gedanken,A. Synthesis, characterization, and properties of metallic copper nanoparticles. Chem. Mater. 1998, 10, 1446–1452

13. Green synthesis of silver nanoparticles using Artemisia annua and Sida acuta leaves extract and their antimicrobial, antioxidant and corrosion inhibition potentials, A.S. Johnson, I.B. Obot, U. S. Ukpong , J. Mater. Environ. Sci. 5(3) (2014) 899-906

14. Dinesh Kumar, Vijender kumar, Zulfiqar Bhat, Mohmmad Iqbal Zargar, International journal of research in phytochemistry and pharmacology 1(4),2014

15. Kritikar KR, Basu BD. Indian Medicinal Plants, Dehradun. 2006; pp.1393-1394.

16. Shriniwas, P.P., Subhash, T.K. Antioxidant, antibacterial and cytotoxic potential of silver nanoparticles synthesized using terpenes rich extract of Lantana camara L. leaves. Biochem. Biophys. Rep. 2017, 10, 76-81.

Paper-16

Looking at the high-energy X-ray universe- An overview

BITOPAN DAS[a], BIPLOB SARKAR[b], and ANKUR NATH[b]

[a] *Department of Mechanical Engineering, Tezpur University, Napaam, Tezpur, Assam, India*

[b] *Department of Applied Sciences, Tezpur University, Napaam, Tezpur, Assam, India*

Abstract:

X-ray astronomy started in the early 1960s and since then, the X-ray range of electromagnetic radiation has produced a great deal of astronomical information about the high-energy universe. We begin this article by giving a brief introduction to X-ray astronomy. We then provide a concise explanation of the emission and detection of X-rays from astronomical systems and discuss some of the known sources of high-energy X-rays in the universe. We also describe the capabilities of the X-ray missions in the past and X-ray missions that are currently underway. Finally, we discuss some of the upcoming X-ray satellites and present the concluding remarks.

Keywords: X-rays, high-energy universe, X-ray satellites, X-ray detectors, high luminosity.

1. Introduction

X-rays are a form of electromagnetic radiation which have frequencies (3×10^{16} Hz–3×10^{19} Hz) much higher than visible light. X-rays were discovered for the first time in 1895 and it is considered as one of the most important discoveries ever. Wilhelm C. Roentgen discovered X-rays while studying electric discharge phenomena in gas. Roentgen noticed a faint glow on the fluorescent screen when the tube was covered with black cardboard. He called these strange new rays X-rays for it to be given an appropriate name later. Usually, X-rays are generated when electrons are accelerated with high voltage.

X-rays from cosmic sources were not observed until post-World War-II advancements in rocket technology. Initially, it was thought that objects in space could not generate stronger X-rays than the Sun. Even if they did, the X-rays

would be masked by the Sun's own X-ray radiation. It was only when a mission headed by Riccardo Giacconi (Riccardo *et al.* 1962) was sent that the first powerful cosmic source of X-rays were discovered. This was a turning point which immediately attracted the attention of the scientific community towards cosmic X-ray sources. It was surprising at that time because the first strong source of X-rays, Sco X-1, was optically fainter by 400 times than the faintest visible star. After this, several surveys were conducted using rockets and high-altitude balloons.

Rocket based surveys only provided minutes of data but they were instrumental in the building the base for X-ray astronomy. With subsequent missions and particularly the Uhuru mission, other sources were observed. However, the processes behind the high energy generation in X-ray sources were still not clear.

Astronomical X-rays are different from medical X-rays which are used to get images of fractures. In case of X-rays used for medical purposes, an obstruction, i.e., a biological part is kept between a source and a detector. Bones and metals absorb X-rays and this appears as an image of the bone on the detector side. In case of astronomical X-rays, the source is a high-energy object or phenomena located at astronomical distances either within the galaxy or outside it. They are detected by instruments operating at high altitudes from the earth's surface in the form of image or spectrum.

2. X-ray emission

Astrophysical X-rays are primarily generated during these three radiation phenomena: (a) thermal bremsstrahlung, (b) synchrotron radiation and (c) black body radiation. At a very high temperature, usually of the order of 10^5 K, gases get ionized into electrons and positive ions. In such ionized media, when an electron encounters a positive ion, they mutually interact and lead to a net acceleration of the lighter electron, thus forcing it to change its path. During such accelerations, electrons emit energy and in astrophysical systems, these emissions are usually dominated by X-rays, at temperatures > 10^6 K. This is how the "bremsstrahlung" radiation is generated. Usually, the ionized media attains a thermal equilibrium and the emitted radiation is thus, a continuum of energy. But in thermal gases, the sources of radiation may be a combination of bremsstrahlung and 'line spectra'. Line emissions occur when fast electrons collide with ions with bound electrons and transfer energy to create a transition to higher energy states. These excited ions decay rapidly to ground state by losing photons with energy equal to the energy level spacing through which they were excited by the electrons, thus, is captured as line spectra. Studying the spectral lines can yield information

about the gas such as temperature and elemental composition (Seward and Charles 1995).

The second mechanism through which X-rays are generated is when a relativistic electron passes through a magnetic field. Such fast moving electrons with a range of velocities experience the electromagnetic Lorentz force and thus get accelerated enough to emit high energy photons. The energy of these photons depends on the velocity of the electrons, the magnetic field strength and the direction of travel. This radiation is named as synchrotron radiation. The spectrum of synchrotron radiation usually has a power law form which arises from the fact that the energy spectrum of the emission source, i.e., the electrons also have a power law spectrum. The spectrum of the power law is given by $I(E) = AE^{\square}$, where A is a constant and $\square$ is the spectral index (Seward and Charles 1995).

The third dominant process of X-ray emission is Planck's black body radiation. The term 'black body' is used to refer to objects which absorb as well as emit radiation of all frequencies in ideal scenarios. This is a universal law for any surface to show blackbody behaviour owing to absorbing radiation energies at different temperatures. The frequency at which a blackbody would be bright depends on its temperature. X-rays became dominant in the blackbody continuum spectra, at temperatures > 10^6 K, and a common astrophysical example is the surface of a star - Neutron stars are very bright in X-rays emitted due to blackbody radiation as accreting material contacts the surface. Mathematically, the spectra of stars with temperatures up to 40,000 K can be expressed approximately as $I(E,T) = 2E^3\left[h^2c^2\left(e^{\frac{E}{kT}} - 1\right)\right]^{-1}$, where I is the intensity, E is the energy of the radiation, T denotes the temperature, h is the Planck's constant, c is the speed of light and k denotes Boltzmann's constant (Seward and Charles 1995).

3. X-ray detection

There are a number of methods used in the detection of X-rays. X-ray detectors are designed such that they return information about the number, location, time of arrival and energy of the X-rays. Since X-rays are of high energy, they are able to ionize many materials. Some of the X-rays will be absorbed by whatever lies in their path including the detector setup. Since most of the missions work in the upper levels of the atmosphere, they have to be made robust enough to withstand the journey on the rocket or balloon; they also have to be secure against the vacuum conditions and adverse temperature ranges. In the early missions, Geiger counters were used which were soon replaced by proportional counters.

3.1 Proportional counters

Proportional counters are a type of detector that are robust and efficient. The detector is a box with a window for allowing X-rays to enter and there is a high voltage wire in the middle. The window has to be thin while being strong enough to withstand the pressure of the gas within when the detector is in the upper layers of the atmosphere. Electrons are liberated when X-ray photons hit an atom by the photoelectric effect. If the energy of the X-rays simply exceeds the amount needed to emit an electron, the primary photoelectrons will use the excess energy to ionize other atoms. The primary and secondary electrons then travel to the high voltage wire and get accelerated by the electric field, ionizing other atoms along the way thereby increasing the strength of the electric field. An avalanche occurs which amplifies the signal. The voltage in proportional counters is maintained such that the initial photon energy is proportional to the charge pulse. In case of Geiger counters, the voltages are comparatively higher which saturate the avalanche. Due to this limitation, Geiger counters used in earlier missions were soon replaced by proportional counters. The probability that the photon actually hits the detector surface is given by the Quantum Efficiency. The optical depths of the window and the gas are expressed respectively as $\tau_w = \rho_w \mu_w(E) x_w$ and $\tau_g = \rho_g \mu_g(E) x_g$ (Arnaud *et al.* 2011), where $\mu(E)$ is the mass attenuation coefficient, x and ρ are the material's thickness and density respectively. Quantum Efficiency can be represented in terms of τ_w and τ_g as (Arnaud *et al.* 2011)

$$P = e^{-\tau_w}(1 - e^{\tau_w}) \quad (1)$$

3.2 Gas-scintillation Proportional Counters

The second important type of detectors are Gas-scintillation Proportional Counters (GSPC). X-rays entering through the window collide with the detector gas ionizing an atom. The primary atom then ionizes other atoms which then move under the electric field's influence. As they gain energy in the strong field scintillation region, they excite other atoms to form diatomic molecules. The diatomic molecules lose energy by emitting x-rays which are detected by photomultiplier tubes (PMT). GSPCs are almost similar to proportional counters except the fact that there is a scintillation region and a set of photomultiplier tubes instead of a charge collection section. The minimum resolution of GSPCs are better than that of proportional counters.

Incident X-rays with energies more than 50 keV cannot be stopped by gas detectors as they have low densities and become virtually transparent. In such cases, crystals of NaI and CsI are used as the detection medium. They are dense enough to absorb X-rays with higher energies and

emit light which is why the process is referred to as scintillation. NaI crystals perform the function of detection while CsI performs the function of background rejections. Scintillation counters have been used in balloon based detection of high energy X-rays.

3.3 Micro-channel plates

Another technology used is micro-channel plates. It consists of a plate with numerous small tubes and pores. A high voltage is applied along the tubes. When a photon strikes one end of a pore, low energy electrons are ejected which becomes an avalanche of electrons as they move. Gas is not required for detection. Although they provide very good spatial resolution, spectral information is lost. ROSAT high resolution imager and Chandra high resolution camera used these instruments. The cathode end is coated with CsI to improve background rejection. An aluminum plastic UV-ion shield is provided to detect only X-rays and reject low energy photons like UV rays and IR rays.

3.4 Calorimetry

Calorimetry is a new, capable method of detecting cosmic X-rays first used in the Suzaku mission (Ezoe *et al.* 2021). In this method, a change in the temperature is detected by a crystal block with high precision thus, essentially making it a spectrometer. It can provide an energy resolution of 6 eV. However, for its functioning, a constant, reliable refrigeration is required which sometimes poses challenges.

Unlike visible light, X-rays don't reflect off shiny surfaces. However, at very small angles of incidence <1°, they can be made to reflect. Such an arrangement can be made which would make a mirror based X-ray telescope (Windt *et al.* 1994). The rays after getting reflected will be collected at a focus. Two main sets are provided, one being parabolic and the other being hyperbolic to increase the telescope's effective area. The image of the detection is bright and is surrounded by a faint ring around it.

3.5 Charge Coupled Devices

Charge Coupled Devices (CCD) are the most popular detection devices in use today. They are used in both optical observations and X-ray detection. The device has a semiconductor substrate where photons fall which is converted into electron-hole pairs (Holst and Lomheim 2007). A charge is stored proportional to the energy of the photon in a pixel. In this way, arrays of pixels are read row by row. A bright detection produces a bright center with a halo ring around it. Charge collection occurs at the capacitors which are basically p-n junctions. Three phase CCDs are

the most common types of CCD with three gates for each pixel. The charge is collected during a period called the frame time, after which the charge from each pixel is transferred in parallel and is then passed through the readout amplifier. CCDs should be operated at very low temperatures and such temperature maintenance can become a major issue as contaminants can accumulate during the journey from earth and also throughout its tenure of operation. The universe is abundant with different types of X-ray emitters and given the high energy needed to generate X-ray photons in the first place, the mechanisms behind the radiation generation vary for the different types of objects.

4. Cosmic High-Energy X-ray Sources

High-energy phenomena in the cosmos are not easily detected from ground-based observatories. This is because X-rays that are emitted from these high-energy sources are absorbed in the atmosphere before they can reach the ground. X-rays from high-energy sources are a result of either particles being accelerated to relativistic speeds or plasma being heated to extreme temperatures. X-ray astronomy therefore helps to understand the nature of such high-energy objects, their composition as well as their evolution. In this section, known high-energy X-ray sources are discussed briefly.

4.1 Active Galactic Nuclei

Active Galactic Nuclei (AGN) are highly luminous objects which are observable over vast distances. AGNs can be differentiated from other sources through their broad emission lines and unusually high luminosity. Before the 1960s, radiation sources like 3C 48 and 3C 273 were observed with broad emission lines and high luminosity but without a visible galaxy around the source. These radio sources having exceptional luminosity were called quasi-stellar radio objects (quasars). Quasars are now perceived as AGNs because they are so far from us that simple optical observations cannot resolve the galaxies they reside in (Osterbrock *et al.* 1991; Tadhunter 2008). Along with quasars, some radio-quiet objects were also observed which were termed quasi-stellar objects or QSOs, the difference with quasars being the luminosities. The luminosities of AGNs can be ~10^{46} ergs/sec (Edelson and Malkan 1986). Such high energies are released from only a very small volume of space. This means that nuclear processes are by no means sufficient to produce the scales of energy observed. The answer lies in the accretion produced by the region of strong gravity. AGNs host supermassive black holes into which material accretes, generating high amounts of energy (Trumper and Hasinger 2008; Arnaud *et al.* 2011).

Accretion around compact objects is an area of study that has attracted many physicists to better understand the mechanism involved. AGNs emit over a broad range of frequencies including X-rays and γ-rays. QSOs and Type 1 Seyfert galaxies are luminous in the X-ray region. Their emission follows power law spectra, observable in the 2-20 keV range (Mushotzky 1984). The mechanism behind emission could be either synchrotron or Compton scattering. Variations in X-rays are also evident from some AGNs with timescales up to 10^6 sec (Mushotzky 1986).

4.2 Supernovae

Supernovae are some of the most beautiful and vibrant events to observe and they are very luminous. A supernova is an event in which a massive star explodes towards the end of its life-cycle and the core of the original star collapses into a neutron star. Supernovae events are very rare but the remnants of the explosion can be studied both from spectral information and visual observations. Supernovae may occur in two ways- one, due to gravitational collapse and second, due to thermonuclear processes. Studying the remnants of a supernova helps explain the supernova in the first place. Obviously, these high-energy events are the source of X-rays, gamma rays, and cosmic rays. Information about the nucleosynthesis of supernovae can be acquired essentially from X-ray spectroscopy consisting of elements Mg, Si, O, Ar, Ne, Ca and Fe, Ni; comprising the alpha-group elements and the iron-group elements respectively (Bethe 1990).

Supernova remnant shocks and their properties can also be studied using X-ray spectroscopy. These are high Mach-number shocks and are collisionless which means that the heating of the atoms doesn't occur through collisions of particles (Vink 2012). Presence of emission lines in the X-ray spectroscopy of supernovae remnants can give information about the temperature and the plasma whereas, absence of such lines indicates that the cause of the X-ray emission may be synchrotron radiation. Studying the X-ray synchrotron radiation can in turn reveal the magnetic field strengths and acceleration of electron cosmic-rays. XMM Newton and Chandra missions have studied the X-ray spectroscopy of supernovae remnants with high resolution. Thus, X-ray spectroscopy has helped physicists and astronomers understand supernovae, supernovae remnants and complex processes such as acceleration of cosmic rays.

4.3 Neutron Stars

Neutron stars are some of the densest objects in the observable universe. Neutron stars produce strong pulses of radiation and spin very quickly. The pulses of radiation observed on Earth is the

consequence of the magnetic axis of the rotating neutron stars lining up with earth based observers' field of view as it spins, since the neutron star's axis of rotation and magnetic pole are not aligned. The densities at their core range from 10^{14} g/cm^3 to 10^{15} g/cm^3 (Lattimer and Prakash 2004). The birth of neutron stars result from the gravitational collapse of massive stars, i.e., through Type II supernovae. Neutron stars' rotation slows down over time as the rotating dipole radiates and the torque arising from that slows down the rotation.

For neutron stars which are isolated, the X-ray bursts are studied by measuring the light curves, luminosities and oscillations of such X-ray bursts. Estimating the radii of isolated neutron stars is more difficult than for binary stars, so studying X-ray bursts provides a model for estimating their radii.

4.4 Cataclysmic Variables

Cataclysmic Variables (CV) are systems in which a white dwarf accretes material from an accompanying star, i.e., in a binary setup. With the white dwarf being the compact object, the time period of the binary is often small. They do not emit X-rays significantly in the higher energy range. Low accretion rates compared to other compact objects are what makes the X-ray emissions weaker (Kuulkers *et al.* 2006). The accretion in most CVs consist of Roche-Lobe filling mechanisms from the donor star (Robinson 1976). Unlike supernovae, which are significantly more luminous and are a very high energy event that occurs once in the lifetime of a very massive star, novae and dwarf novae involve lower energy release and have also been found to be recurring. Novae are triggered by unstable thermonuclear processes on the surfaces of a white dwarfs. The accretion does not account significantly towards the energy release during nova outbursts. Nevertheless, the accretion discs in Cataclysmic Variables serve as excellent study subjects for accretion in general. The number of novae are much more than that of supernovae. The main types of CVs are magnetic and non-magnetic- in the former, radiation emission is primarily due to the accretion disc whereas, in the latter, radiation emission occurs as a result of matter falling in due to magnetic effects. The disc can reach temperatures of up to 10^4 K due to viscous effects.

If the mass of a white dwarf crosses the Chandrasekhar Limit (~ 1.4 $M_\odot$), a type Ia supernova would occur due to the gravitational collapse of the star. When mass transfer rate through the disc is low, i.e., when the state is quiescent, the viscosity is low and so are temperatures. When the density of the quiescent disc rises to a critical value, viscosity increases and dwarf nova outbursts occur. Dwarf novae can be divided into two categories- U Gem and Z Cam. In U Gem stars, outbursts occur in weeks

whereas, in Z Cam stars, standstill periods occur between outbursts (Kuulkers *et al.* 2006).The flickering X-ray radiation that we observe is caused by shocks in the interior regions of accretion discs. In such cases, only the inner disc has enough energy to generate X-rays.

4.5 Clusters of Galaxies

The galaxy clusters are again some of the most luminous objects with X-ray luminosities reaching around 10^{43}-10^{45} ergs/s (Sarazin 1986). They are structurally the largest objects in the observable universe which can span up to 10 MPc across. These galaxy clusters are gravitationally bound and an individual cluster can have as many as 10^4 galaxies in it. Gas which is millions of degrees hot is present in the space between the galaxies (Forman and Jones 1982). The hot gas clouds called inter-cluster medium (ICM) are the source of strong X-rays which are mostly of thermal bremsstrahlung origin. X-ray imaging provides information about the structure of the clusters as the intergalactic ICM radiates in the X-ray regime. Not only that, X-ray studies also tell a lot about the composition, formation and population within a cluster. Over time, loosely bound structures within the galaxy clusters form dense aggregations.

X-rays from galaxy clusters appear in a diffused form and not as individual sources. This is because of the hot gas that is present throughout the region, held together by the gravitational effects of dark matter. X-ray observations from galaxy clusters can reveal information about the temperature of the hot gas which can be used to estimate the depth of the gravitational potential which in turn can tell us how much matter is present within the region. The ICM temperature and the chemical composition of the plasma can be measured by X-ray spectroscopy.

Galaxy clusters also merge at a high speed of about 2000 km/s. The resulting release of gravitational energy is extremely large, on the order of 10^{64} ergs. The shocks that dissipate gravitational energy heats the ICMs and gives them the characteristic high temperatures. However, intracluster gas has been found to be cooling in some regions by the Einstein Observatory.

4.6 X-ray Binary Systems

X-ray binaries are two-membered systems in which one member is a compact object (either a black hole or a neutron star), with each member orbiting around the other. They are luminous in X-rays and are therefore known to have very high energy output. The high luminosities result from accretion as material from the companion star spirals onto the compact member under very strong gravitational fields. The accreting material

heats up due to viscous effects. X-ray binaries have been at the center of discussion about them being the evidence of black holes. It was in the early observations from X-ray missions in the 1960s like Cyg X-2 and Sco X-1 when it was found that these compact objects are much more massive than white dwarfs. Also, the pulsating periods were very small, for which candidates like white dwarfs would not be able to withstand the high centrifugal forces. There were only two options remaining- neutron stars or black holes. Since the orbiting periods are short, the members in such binary systems have to be close which in turn allows for mass transfer to happen.

X-ray binaries consist of two types- Low-mass X-ray binaries (LMXB) and High-mass X-ray binaries (HMXB). In HMXBs, the companion stars are massive stars and mass transfers occur through stellar winds. Mass transfer in LMXBs take place by accretion through overflow of Roche-lobe equipotential surfaces. Because the stars in LMXBs are of low mass, they are not easily visible in the optical range. Accretion of matter in LMXBs takes place through a Roche-lobe filling method as mentioned above. As the matter has angular momentum, it rotates in a Keplerian orbit around the compact star, thus forming a disc shape. Temperatures can reach as much as 10^7 K in the inner regions of the disc and hence produces the X-ray radiation (Done *et al.* 2007; Seward and Charles 1995).

X-ray examination is the most preferred method for finding black holes. It is accepted as the norm that the mass of a compact object must be> $3M_{\odot}$ for the binary system to be a black hole binary system. The mass of a compact object can be found from spectroscopic information if the mass function is known (Done *et al.* 2007)-

$$f(M) = \frac{M_x^3 i}{(M_x+M_c)^2} = PK^3/2\pi G \qquad (2)$$

In Eq. (2), M_c and M_x are the masses of the companion star and the compact object respectively, i is the orbit inclination, P is the period and K is the Doppler curve amplitude. What differentiates black hole binary systems from neutron star binary systems is that in systems where a black hole is the compact object, the material accreting onto it will disappear after passing through the event horizon, whereas in the latter case, there is an actual surface, from which kinetic energy is released as the material touches the surface releasing black body radiation (Done *et al.* 2007).

5. Past X-ray satellites

Over the past decades, there have been many X-ray missions ranging from minutes-long rocket flights, hot-air balloon missions, to large-scale orbiting satellites. The first evidence of cosmic X-ray sources in the 1960s sparked an interest in X-

ray space research and opened the door for X-ray missions. There is no doubt that X-ray missions have helped provide evidence and data for phenomena that would otherwise have remained in the mathematical realm of theoretical physics. Three X-ray astronomical observatories that have operated in the past are discussed below:

5.1 RXTE Mission

The Rossi X-ray Timing Explorer (RXTE) mission, given a name after physicist Bruno Rossi, was launched by NASA and it operated from 1995 to 2012. This satellite mission was designed for rapid X-ray timing measurements and it has produced numerous excellent results in X-ray astronomy. The RXTE consisted of three sets of detectors- a proportional counter array (PCA), the High Energy X-ray Timing Experiment (HEXTE; 15-250 keV) and an All-Sky Monitor (ASM; 2-10 keV). The PCA consisted of five identical xenon gas proportional counter units, called PCUs, which detected X-rays with energies ranging from 2 to 60 keV. These PCUs had 1-m-long honeycomb collimators so that the field of view could be limited to 1 degree Full-Width at Half Maximum (FWHM) using these detectors.

The instruments aboard RXTE made a significant contribution in the study of neutron star properties. RXTE data was especially useful for studying X-ray binaries, together with accretion-powered pulsars. A noteworthy achievement of the RXTE mission was the discovery of kHz quasi periodic oscillations (QPOs), which provided information about the innermost region of an accreting and rotating neutron star. In 1998, RXTE discovered the first coherently pulsating accreting millisecond pulsar. The launch of RXTE in 1996 considerably increased the rate of detection of transient X-ray sources. The ASM instrument onboard RXTE scanned up to ~80% of the sky daily and it was sensitive enough to detect bright X-ray transients from almost anywhere in the Galaxy. For detailed description on RXTE, see (Seward and Charles 1995; Trumper and Hasinger 2008; Arnaud *et al.* 2011).

5.2 Suzaku Mission

Suzaku was an orbiting joint Japanese-US X-ray mission which started in July 2005. It achieved a mission duration of over 10 years and was declared completed in 2015. Suzaku observed X-rays shining from high energy X-ray sources, such as supernova explosions, AGNs, X-ray binaries and galactic clusters. This mission provided a unique sensitivity over a wide range of energies from 0.2 to 600 keV. Suzaku consisted of two co-aligned instruments as the scientific payload: an X-ray Imaging Spectrometer (XIS) (Koyama *et al.* 2007) and a higher-energy detector (HXD) (Takahashi *et al.* 2007). The XIS

(consisting of four imaging CCD cameras) and HXD instruments onboard Suzaku, were sensitive in the energy bands of 0.2-12 keV and 10-600 keV, respectively.

Suzaku produced significant results from various cosmic X-ray sources. The sensitive HXD instrument performed measurement of the spectra of the hard component in a number of supernova remnants (Sawada *et al.* 2019). It was the Suzaku mission which spotted the metals chromium and manganese in intergalactic space for the first time (Tamura *et al.* 2009). This was the largest known concentration of rare metals in the universe. Suzaku performed the chemical census of the universe and it revealed just how rare and precious some corners of the cosmos are. For details on Suzaku mission, see (Trumper and Hasinger 2008; Mitsuda *et al.* 2007).

5.3 BeppoSAX Mission

The X-ray satellite BeppoSAX was a significant Italian project in which the Netherlands participated. Several small instruments made observations in a wide spectral coverage of 0.1-300 keV, which was the main scientific feature of the mission. The instruments were co-aligned and pointed to an accuracy of 2'. The purpose of this X-ray mission was to characterize the cosmic X-ray sources through timing and spectral analysis.

The wide energy coverage was designed for the precise determination of spectral parameters. The satellite included four gold-coated nested concentrator/ mirror assemblies. These focused on position-sensitive gas scintillation proportional counters to collect photons below 10 keV. A collimated High pressure Gas Scintillator Proportional Counter (HPGSPC), extended coverage from 4 to 120 keV (Manzo *et al.* 1997), and a collimated Phoswich Detection System (PDS), recorded photons with energies from 15 to 300 keV (Frontera *et al.* 1997).

The scientific payload onboard BeppoSAX included two wide-field cameras (WFCs), which accomplished the task of long-term monitoring of strong X-ray sources and detecting transients (Jager *et al.* 1997). Each WFC made use of a xenon-filled position-sensitive proportional counter (PSPC) behind a coded mask. BeppoSAX mission was launched on April 30 1996 and it was in operation for six years, making the first observations of X-ray afterglow in a gamma-ray burst and monitoring the afterglow intensity of many gamma ray-burst sources. The mission obtained broadband spectroscopy of all types of X-ray sources and it was particularly useful in X-ray binary studies (Seward and Charles 1995
; Arnaud *et al.* 2011; Boela *et al.* 1997).

6. Current X-ray satellites

Presently, there are a number of different X-ray satellites with each mission carrying a different set of instruments with varying detection sensitivity. A few of the current X-ray missions are discussed below.

6.1 NuSTAR

NuSTAR is a satellite manufactured by NASA in collaboration with the California Institute of Technology and launched in June 2012 to detect high-energy X-rays in the energy range 3-79 keV (NuStar https://www.nustar.caltech.edu/page/instrumentation). It was basically implied for a two-year operation period. The NuSTAR data provides further insights into black holes from their accretion energies, the supermassive black hole at the heart of the Milky Way and other powerful sources of X-rays in the Milky Way. Neutron stars and relativistic jets which emit X-rays are also a focus of the NuSTAR mission. The satellite has four hybrid detectors with a CdZnTe sensor, 133 concentric mirror shells and a resolution of 12.5". The extended length of the satellite is 10 m and the satellite was launched on a Pegasus XL rocket.

6.2 ASTROSAT

ASTROSAT is an Indian Astronomical mission launched in September, 2015 with an initial operation plan of five years (Singh *et al.* 2014). ASTROSAT can conduct surveys in different electromagnetic energy bands. The primary instruments for detecting X-rays in the ASTROSAT are the Soft X-ray Telescope (SXT) and the Large Area Xenon Proportional Counters (LAXPC). SXT is for soft X-rays and has a detection range of 0.3-8 keV. LAXPC has three proportional counters with a detection range of 3-80 keV for hard X-ray observations (ASTROSAT https://www.issdc.gov.in/docs/as1/AstroSat_Payloads.pdf). SXT performs spectroscopy of galactic plasma, supernovae remnants, clusters of galaxies, AGNs, accretion discs and shocks while the LAXPC studies the variability of X-ray sources. For hard X-ray imaging, another instrument is provided- the CZTI (Cadmium Zinc Telluride Imager) with energy sensitivity in 10-250 keV region and it is helpful in the spectroscopy of strong X-ray sources. The CZTI can also perform hard X-ray monitoring above 80 keV. Not only that, another instrument- Scanning Sky Monitor (SSM) is present for detecting transient X-ray sources and it is sensitive in the 2-10 keV energy band.

ASTROSAT is a multi-wavelength satellite and it can perform observations on wavelengths ranging from optical to hard X-rays simultaneously. The simultaneous observations

over multiple wavelengths help properly understand the underlying physics of cosmic X-ray sources. ASTROSAT has low inclination which leads to less contamination from background radiation. Unlike other X-ray satellites where detectors get saturated from bright X-ray sources, the SXT in ASTROSAT is capable of detecting bright sources reliably.

6.3 Swift Mission

Swift is a mission which is primarily dedicated to detecting gamma ray bursts. It can carry observations on different wavelengths- X-rays, γ-rays and UV/optical (Gehrels *et al.* 2004). The X-ray telescope is a narrow field telescope with a detection range of 0.3-10 keV while the Burst Alert Telescope (BAT) can perform hard X-ray observations in the 15-150 keV range. Launched in 2004 by NASA in collaboration with Italy and the United Kingdom, data from the SWIFT helps understand the early universe from the study of γ-rays, by recording the origin of γ-ray bursts and classifying them.

6.4 Chandra X-ray Observatory

Chandra X-ray Observatory is a very capable and accomplished X-ray satellite. It was launched in July 1999 on Space Shuttle Columbia. It has an energy detection range 0.08-10 keV and works on an elliptical, higher earth orbit (Weisskopf *et al.* 2000). It can provide uninterrupted observations up to over 50 hours. There are a total of four nested mirrors with the focal length being 10 m and resolution being 0.5'. The structure is 13.8 m long and the satellite consumes only 600 Watts. The effective area of the mirrors are about 800 cm^2 and 10 CCD chips are provided for image capture and spectroscopy. At the time when it was made, the technology put into making the satellite was the most precise and advanced in the world. With a high resolution and large area, it is capable of detecting faint sources from even dense regions. With Chandra, a new era of X-ray observations has begun, allowing humans to efficiently observe and study high-energy phenomena in the universe.

6.5 XMM-Newton

XMM-Newton is a mission of the European Space Agency (ESA) which was launched in December 1999. It has three CCD cameras, two of which are Metal Oxide Semiconductor CCDs. The setup has a 30' FOV and an energy sensitivity range of 0.15-15 keV. Half of the incoming X-rays are used by the Refraction Grating Spectrometer (RGS) which diffracts the rays to a strip of CCDs (Jansen *et al.* 2001). The RGS setup is used to measure the energy and position of each photon; the telescope's focal length is 7.5 m. The entire structure is 10 m weighing 4000 kg. The telescope has a length of 6.8 m. The main structural

elements are made of carbon composites which have many advantages such as low thermal expansion, high modulus of elasticity and light weight characteristics.

6.6 NICER Mission

The NICER (Neutron Star Interior Composition Explorer) is another mission installed on the International Space Station (ISS) which was launched on a SpaceX Falcon 9 rocket (Arzoumanian *et al.* 2014) in June 2017. As the name suggests, this mission is meant to perform precise measurements of neutron stars properties like mass, magnetic fields, radius, density etc. (Gendreau 2012). Thermal and non-thermal emission spectroscopy studies of neutron stars can be performed through NICER in the range of energy 0.2-12 keV.

7. Future X-ray Missions

A number of X-ray missions are scheduled for launch in the coming years. Some of these future missions are in the development stage while some are undergoing testing before the actual launch. NASA's next X-ray mission- the Imaging X-ray Polarimetry Explorer (IXPE) is scheduled for launch in 2022 (NASA's HEASARC https://heasarc.gsfc.nasa.gov; IXPE Home https://wwwastro.msfc. nasa.gov/ixpe). It will provide temporal, spectral and spatial measurements of X-ray sources simultaneously. Planned for launch in 2027, the eXTP or Enhanced X-ray Timing and Polarimetry mission will study mainly stellar mass black holes, magnetars, neutron stars and supermassive black holes. It will be able to detect radiation in the range 0.5-30 KeV (eXTP 2021). Advanced Telescope for High Energy Astrophysics (ATHENA) is an X-ray observatory mission being developed by the ESA with contributions from NASA. It will have a large-aperture grazing-incidence X-ray telescope with 12 m focal length and will study baryons in galaxy clusters and accretion onto compact objects (Athena https://www.the-athena-x-ray-observatory.eu/). It is expected to launch in the early 2030s. The X-Ray Imaging and Spectroscopy Mission (XRISM), expected to launch in 2022, will be capable of conducting high-resolution spectroscopy and imaging high-energy X-ray sources. The payload will be launched on a JAXA H-IIA rocket and will have two instruments- a spectrometer, Resolve and an X-ray imager, XTend (XRISM https://heasarc.gsfc.nasa.gov/docs/ xrism/). It is being developed by NASA and JAXA with participation from ESA.

8. Summary and conclusions

X-ray astronomy, as a field, is a relatively recent entrant in the realm of astronomy. Before

X-rays were known to exist, light in the visible range was believed to be the only radiation emitted by celestial objects. Even after 60 years of the discovery of X-rays, no X-ray emitting sources were observed beyond the solar system. But the enthusiastic short-duration rocket and balloon missions of the 1960s brought a significant change in the way astronomical studies were carried out. X-ray astronomy has opened a whole new vista into studying complex phenomena occurring light years away from us. The fact that there are objects that emit X-rays, supernovae and neutron stars to AGNs and X-ray binaries, shows that the scale of energy output in such systems is very high. Therefore, the study of the high-energy universe in different energy bands certainly requires X-ray astronomy. In this article, we have provided a brief review of the X-ray astronomy of high energy objects in the universe. The emission and detection methods used in modern day X-ray astronomy are discussed. In addition, known high-energy objects are also discussed. Later, past and current X-ray missions working in space are described with the specifications, objectives and uniqueness of each mission. Some of the upcoming X-ray missions are also discussed. The advances in X-ray astronomy over the past few decades have been remarkable and this is just the beginning. There is also the need for more missions capable of carrying observations in different wavelengths simultaneously, i.e., multi-wavelength astronomy. Observing cosmic objects over a broad range of spectra at a given time would allow us to properly understand the physics of high-energy objects, thus providing us with a complete picture. The scope of X-ray astronomy is, therefore, vast and it helps us to understand the high energetic phenomenon happening at huge distances.

References

Arnaud, K., Smith, R., & Siemiginowska, A. 2011, Handbook of X-ray Astronomy, by K. Arnaud, R. Smith, and A. Siemiginowska. Cambridge, UK: Cambridge University Press, 2011.

Arzoumanian Z., Gendreau KC., Baker C.L. et al. 2014, The neutron star interior composition explorer (NICER): mission definition. Space Telescopes and Instrumentation 2014: Ultraviolet to Gamma Ray, Volume 9144 (International Society for Optics and Photonics, 2014), p. 914420.

ASTROSAT Payloads, 2021: https://www.issdc.gov.in/docs/as1/AstroSat_Payloads.pdf [accessed July 2021].

Barr, P. & Mushotzky, R.F. 1986, Nat, 320, 421.

Bethe, H.A. 1990, Rev. of Mod. Phys., 62, 801.

Boella, G., Butler, R.C., Perola, G.C., et al. 1997, Astron. And Astroph. Supp. Series, 122, 299.

Boldt, E.A. 1987, NASA Conference Publication, 2464, 339.

Done, C., Gierliski, M., & Kubota, A. 2007, Astron. and Astroph. Rev., 15, 1.

Edelson, R.A. & Malkan, M.A. 1986, Astroph. J., 308, 59.

Ezoe Y., Ohashi T., Mitsuda K. 2021, Rev. of Mod. Plasma Phys. 5, 1-43

Forman, W. & Jones, C. 1982, Ann. Rev. of Astron. and Astroph., 20, 547.

Frontera, F., Costa, E., dal Fiume, D., et al. 1997, procspie, 3114, 206.

Gehrels, N. & Swift 2004, American Astron. Soc.

Gendreau K.C., Arzoumanian Z., Okajima T. 2012, The Neutron star Interior Composition ExploreR (NICER): an Explorer mission of opportunity for soft x-ray timing spectroscopy. Space Telescopes and Instrumentation 2012: Ultraviolet to Gamma Ray, Volume 8443 (International Society for Optics and Photonics, 2012) p. 844313.

Giacconi, R., Gursky, H., Paolini, F.R., et al. 1962, Phys. Rev. Lett., 9, 439.

Holst, G. C. 2007, CMOS/CCD sensors and camera systems, Gerald C. Holst, Terrence S. Lomheim. SPIE Press Book.

IXPE Home: Expanding the X-ray View of the Universe, 2021: https://wwwastro.msfc.nasa.gov/ixpe/ [accessed July 2021].

Jager, R., Mels, W.A., Brinkman, A.C., et al. 1997, Astron. and Astroph. Supp. Series , 125, 557.

Jansen, F., Lumb, D., Altieri, B., et al. 2001, Astron. And Astroph., 365, L1.

Koyama, K., Tsunemi, H., Dotani, T., et al.2007, Publ. of Astron. Soc. of Japan, 59, 23.

Kuulkers, E., Norton, A., Schwope, A., et al. 2006, Compact stellar X-ray sources, 421.

Lattimer, J.M. & Prakash, M. 2004, Science, 304, 536.

Manzo, G., Giarrusso, S., Santangelo, A., et al. 1997, Astron. and Astroph. Supp. Series, 122, 341.

Mitsuda, K., Bautz, M., Inoue, H., et al. 2007, Publ. of Astron. Soc. of Japan, 59, S1.

Mushotzky, R.F., Done, C., & Pounds, K.A. 1993, Ann. Rev. of Astron. and Astroph., 31, 717.

NASA's HEASARC, 2021: https://heasarc.gsfc.nasa.gov [accessed July 2021].

NuStar, 2021: https://www.nustar.caltech.edu/page/instrumentation [accessed July 2021].

Osterbrock, D.E. 1991, Reports on Prog. in Phys., 54, 579.

Robinson E.L. 1976, Ann. Rev. of Astron. and Astroph. 14, 11.

Sarazin, C.L. 1986, Rev. of Mod. Phys., 58, 1.

Sawada, M., Tachibana, K., Uchida, H., et al. 2019, Publ. of Astron. Soc. of Japan, 71, 61

Seward, F.D. & Charles, P.A. 1995, Exploring the X-Ray Universe, by Frederick D. Seward and Philip A. Charles, pp. 414. ISBN

0521437121. Cambridge, UK: Cambridge University Press, November 1995, 414.

Singh K.P., Tandon S.N., Agrawal P.C. et al. 2014 ASTROSAT mission, in: Space Telescopes and Instrumentation 2014: Ultraviolet to Gamma Ray, Volume 9144 (International Society for Optics and Photonics, 2014) p. 9144S.

Tadhunter, C. 2008, New Astro. Rev., 52, 227.

Takahashi, T., Abe, K., Endo, M., et al. 2007, Publ. of Astron. Soc. of Japan, 59, 35.

Tamura, T., Maeda, Y., Mitsuda, K., et al. 2009, Astroph. J. Lett., 705, L62.

The Athena X-ray Observatory: Community Support Portal, 2021: https://www.the-athena-x-ray-observatory.eu/ [accessed July 2021].

The eXTP Mission, 2021: https://www.isdc.unige.ch/extp/ [accessed July 2021].

Trumper, J.E. & Hasinger, G. 2008, The Universe in X-Rays: , Astronomy and Astrophysics Library. ISBN 978-3-540-34411-7. Springer Berlin Heidelberg, 2008.

Vink, J. 2012, Astron. and Astroph. Rev., 20, 49.

Weisskopf M.C., Tananbaum H.D., Van Speybroeck L.P., O'Dell S.L. 2000. Chandra X-ray Observatory (CXO): overview. X-Ray Optics, Instruments, and Missions III, Volume 4012 (International Society for Optics and Photonics, 2000) p. 2-16.

Windt D.L., Waskiewicz W.K., Griffith J.E. 1994, App. Optics. 33, 2025-2031.

X-Ray Imaging and Spectroscopy Mission (XRISM), 2021: https://heasarc.gsfc.nasa.gov/docs/xrism/ [accessed July 2021].

Paper-17

"Study of Synthesis and Applications of Zinc sulphide (ZnS) Thin Films: Review"

Mahendra S. Shinde
Department of Physics, M.J.M. Arts, Commerce and Science College, Karanjali, Tal: Peth, Dist: Nashik
Affiliation: S. P. Pune University, Pune (MS), India

Abstract:

Zinc sulphide is II-VI compound Semiconducting material. It is very efficient due to its properties like wide band gap, high refractive index, high transmittance and lower Bohr exciton radius. Nanocrystalline semiconducting Zinc sulphide thin films evoked much attention due to their vast potential with wide variety of applications in various fields. It is used as key material for solar control coatings, antireflection coating for heterojunction solar cells, for light emitting diode and other optoelectronic devices such as blue light emitting diode, electro luminescence devices and photovoltaic cells which enable wide application in the field of displays, sensors and lasers. There are several synthesis techniques for preparation of zinc sulphide thin films. In this article we have reviewed different deposition techniques and applications of ZnS Thin films studied by various researchers.

Keywords: Zinc Sulphide, Thin films, Nanocrystalline, Band gap.

1. Introduction

Zinc sulphide is II-VI compound semiconductor material. It is very efficient due to its properties like wide band gap, high refractive index, high transmittance and lower Bohr exciton radius.Nanocrystalline semiconducting Zinc sulphide thin films evoked much attention due to their vast potential with wide variety of applications in various fields. It is used as key material for solar control coatings , antireflection coating for heterojunction solar cells, for light emitting diode and other optoelectronic devices such as blue light emitting diode, electro luminescence devices and photovoltaic cells which enable wide application in the field of displays, sensors and lasers. There are several synthesis techniques for preparation of zinc sulphide thin films like Thermal evaporation, Spray pyrolysis, Molecular beam epitaxy, RF reactive sputtering, Chemical bath deposition, Modified chemical bath deposition, Photo chemical deposition, Atomic layer deposition, Screen printing, in this article we are studying various synthesis methods and its applications studied by various researchers.

2. Result and Discussion:

First time in 1943 Hammer[1] studied the behavior of ZnS thin films and found that these films have nonabsorbing nature in the visible region, later Huldt (1959) [2], Gonellian (1996)[3] have shown the enhanced absorption of ZnS films in the neighborhood of $\lambda = 330$ nm and Nadeem (2000)[4] for $\lambda = 360$ nm with fine grained size. Oikkonen [1985] et al. [5] grew ZnS thin films from anhydrous zinc acetate and hydrogen sulfide by atomic layer epitaxy (ALE) at 290^0C to 330^0C. Thickness of the films ranged from 110 to 1350 nm. The average crystallite size was 40-80 nm depending upon the film thickness. These values were more than one half of those observed earlier for ZnS thin films grown by ALE from $ZnCl_2$ and H_2S and two or three times of those found in the films grown by electron beam evaporation. Milind Bhise (1989) et al.[6] have studied the effects of various deposition techniques on the growth of ZnS thin films on a sintered $BaTiO_3$-based complex perovskite substrate, using the scanning electron microscope. It was found that films grown by electron-beam evaporation and resistance-heated evaporation showed a shadowing effect. Increase in the thickness of the films tends to decrease the shadowing effect. On the contrary, films grown by the atomic layer epitaxy method, exhibit a complete and uniform coverage of the substrate, even for thin (< 100 nm). Lindroos et al. [1994] [7] found that the films grown on Al_2O_3 and Si (1 1 1) were inhomogeneous and of poor quality. The XRD analysis showed that ZnS films were polycrystalline and presumably cubic. Some preferential (1 1 1) orientation was detected. The films were found to begin to crystallize for a thickness of 30 nm. The annealing (3 h, at 500^oC and N_2 atmosphere) increased the intensity of (1 1 1) line and decreased the half width correspondingly. The S/Zn ratio was approximately 0.8 and it increases with thickness. The ZnS films were found to contain uniformly distributed oxygen. Y. Nosaka (1994) et al. [8] have prepared ZnS thin films by a new type of laser chemical vapour deposition process, in which the reactants are incorporated in the mist of the solvent. It was applicable to prepare high-quality thin films from reactants having a low vapour pressure. By using a continuous wave CO_2 laser, ZnS thin films, consisting of c-axis oriented ultrafine microcrystallites, have been prepared. J M Dona (1994) et al. [9] have prepared ZnS thin films from NH_3/NH_2-$NH_2/SC(NH_2)_2/ZnSO_4$ solutions using chemical bath deposition method. The effect of various process parameters on the growth and the film quality is presented. A first approach to a mechanistic interpretation of the chemical process was reported. The structural, optical, chemical, and electrical properties of the ZnS thin films deposited by this method have been studied. The electron diffraction (EDS) analysis showed that the films were microcrystalline with a cubic structure. E-DAX analysis has demonstrated that the films were highly stoichiometric. Scanning electron microscopy studies of the ZnS

thin films deposited by this method showed that the films were continuous and homogeneous. Electrical conductivity measurements have shown the highly resistivity nature of these films. Olga L Arenas (1997) et al [10] demonstrate the deposition of ZnS thin films with a thickness of 0.04 to 0.45μm at temperatures ranging from 25 to 80^0C from chemical baths comprising zinc sulphate, triethanolamine and thioacetamide at pH of about 10. They found that the deposited films do not show crystallinity, photosensitivity with conductivity 10^{-9} $\Omega^{-1}cm^{-1}$. Annealing of the films in air at 450 to 500^0C for 1 - 2 h leads to partial conversion of the ZnS films to ZnO films. This was accompanied by an increase in the photoconductivity by more than six orders of magnitude. The optical bandgap was >3.85 eV in the as-prepared films, after annealing in air the value drops to about 3.7 eV. Jie Chenget (2003) et al. [11] have grown crystalline zinc sulfide (ZnS) thin films by chemical bath deposition (CBD) method using the mixed aqueous solutions of zinc acetate, thiourea and tri-sodium citrate as the complexing agent. After suitable characterization they found that the as-deposited thin films were homogeneous with pure wurtzite structure. Its optical band gap was found to be 3.53 eV.

A. Antony (2005) et al. [12] have synthesized zinc sulfide thin films by chemical bath deposition from different host solutions. The variation in the optical and electrical properties of these films with the pH value of the reaction mixture was investigated in details. The films showed a high transmission (>80%) and a wide band gap of 3.93 eV. The resistivity of the films was found to decrease with the increase in pH of the reaction mixture and was approximate to 10^4 Ω-cm for pH 10.6. The refractive index, extinction coefficient and the dielectric constants of the chemical bath deposited ZnS films were measured. The films prepared from the zinc nitrate solution have been found to possess a higher band gap, better transparency and surface morphology compared to the films grown from zinc chloride solution. S.D. Sartale (2005) et al. [13] have reported a new chemical bath deposition route for the preparation of dense, compact and uniform nanocrystalline ZnS thin films, where thiourea acts as a complexing agent as well as a source of sulfide ions and explained cluster-by-cluster growth mechanism of film and residual powder. The formed film and powder have cubic zinc blende structure with transmittance of about 75% in the visible region. Liudmila V (2005) et al.[14] have grown zinc sulfide thin films using chemical bath deposition (CBD) method on soda lime glass, silicon and gallium phosphide substrates using an acidic (acetic acid-thioacetamide) and ammonia (thiourea or thioacetamide) baths. The thickness of the films varied from a few nm to 100 nm. Films deposited using the acidic bath showed a smaller concentration of Zn-O bonds and are much closer to ZnS stoichiometry, as

it was found by x-ray photoelectron spectroscopy and wavelength-dispersive x-ray fluorescence spectroscopies. X-ray diffraction patterns prove crystallinity of as deposited films from the acidic bath, which crystallize in the cubic modification. The optical band-gap energy was determined to be 3.64 eV from the best-fit of spectroscopic ellipsometry measurements. Liangyan Chen (2006) et al.[15] have grown ZnS thin films by modified chemical bath deposition (CBD). The parameters which concern the growth and properties of the films including the concentration of the sources, pH value of the solution, the deposition temperature were optimized. X-ray diffraction patterns indicated that the annealed samples are microcrystalline with a sphalerite structure. The band gap of the annealed films was about 3.1eV. The effects of complexing agents on the deposition of the films were discussed. Mustafa Oztas (2007) et al. [16] have synthesized ZnS thin films by spray pyrolysis technique using aqueous solution of zinc chloride and thiourea at molar ratio of 1:1, 1:2, and 2:1. The depositions were carried out on substrates heated from 400 to 520°C .The films were then annealed under sulphur atmosphere for 90 min at 450 and 550°C. The crystallites exhibit preferential orientation along the (0 0 2) α or (1 1 1) β directions. A. U. Ubale (2007) el al. [17] have reported synthesis of ZnS thin films of different thicknesses by chemical bath deposition using thiourea and zinc acetate as S^{2-} and Zn^{2+} source. The effect of film thickness on the optical and structural properties was studied. The optical absorption studies in the wavelength range 250–750 nm showed that band gap energy of ZnS increases from 3·68–4·10 eV as thickness varied from 332–76 nm. The structural estimation showed variation in grain size from 6·9–17·8 nm with thickness. From thermoemf measurement films prepared by this method were of n-type. K. R. Murali (2008) et al. [18] have synthesized zinc sulphide thin films by the pulse plating technique using AR grade zinc sulphate and sodium thiosulphate precursors. The pH of the deposition bath was adjusted to 2. The duty cycle was varied in the range of 20–60%. After suitable characterization it was found that zinc sulphide films have single phase cubic structure and heat treatment changes the crystal structure into hexagonal structure. Optical absorption measurements indicated a band gap values in the range of 3.6–4.0 eV.

Busarin Noikaew (2008) et al.[19] have synthesized highly transparent and nanocrystalline zinc sulfide thin films onto various substrates by chemical bath deposition method and studied the influence of deposition parameters on the physical properties of films in order to understand the optical properties and surface morphologies. They found that the degree of transparency depends on the concentration of thiourea and the deposition time. The

surface morphology depends on the roughness of the substrates. T Bennasr et al. (2008) [20] have deposited zinc sulphide thin films on SnO_2/glass using the chemical bath deposition technique. After suitable characterization they specify the effect of pH of solution and heat treatment in vacuum at 500^0C. The cubic structure corresponding to the (1 1 1) planes of beta-ZnS was obtained for pH equal to 10. The work function ($\phi_{material}$ - $\phi_{probe)}$ for ZnS deposited at pH 10 was equal to -152 meV. Annealing at 500^0C increases $\phi_{(m)}$ (by about 43 meV) and induces the formation of a negative surface barrier. Z. Q. Bian et al. (2008) [21] have synthesized zinc sulfide (ZnS) thin films on glass substrates deposited at 80–82^0C using a mixed aqueous solution of zinc sulfate, ammonium sulfate, thiourea, hydrazine hydrate, and ammonia at the alkaline conditions. Both the traditional magnetic agitation and the substrates vibration by hand frequently were done simultaneously during the deposition. The substrates vibration reduced the formation and residence of gas bubbles on the glass substrates during growth and resulted in growth of clean ZnS thin films with high quality. Ammonia and hydrazine hydrate were used as complexing agents. It was found that hydrazine hydrate played an important role in growth of ZnS films. The structure and microstructure of ZnS films were characterized by scanning electron microscopy (SEM), X-ray diffraction (XRD) and UV-VIS spectroscopic methods. The XRD showed a hexagonal structure. The formed ZnS films exhibited good optical properties with high transmittance in the visible region and the band gap value was estimated to be 3.5–3.70 eV. Reza Sahraei (2008) et al. [22] have synthesized nanocrystalline zinc sulphide thin films by a new chemical bath deposition route on glass and quartz substrates using a weak acidic bath, in which nitrilotriacetic acid acts as a complexing agent and thioacetamide acts as a source of sulphide ions. The thickness of films varied from a few nm to 500 nm. The chemical composition of films was determined by energy dispersive X-ray analyzer and Fourier transform infrared spectroscopy. The films were very close to ZnS stoichiometry and no organic compounds, or $Zn(OH)_2$, or ZnO species were observed as impurities in them. X-ray diffraction indicates that the films have cubic zinc blende structure. SEM images showed that the films consisted of small uniform grains (about 40 nm in size) and were free of pinholes. The effect of film thickness on optical properties, band gap energy and the size of nanocrystals were studied by UV-VIS spectrophotometer measurements. The films of about 170 nm thickness have high transmittance of about 75% in the visible region. A.Goudarzi (2008) et al. [23] have prepared zinc sulfide thin films on glass substrates by ammonia-free chemical bath deposition method using thioacetamide as the sulfide source and ethylene diamine tetra acetic acid disodium salt as the complexing agent in a solution of pH = 6.0. Thin films of ZnS with

different thicknesses of 18–450 nm were prepared. The effect of film thickness and annealing temperature in atmospheric air, on optical properties, band gap energy and grain size of nanocrystals were studied. The X-ray diffraction analysis showed a cubic zinc blend structure and a diameter of about 2–5 nm for ZnS nanocrystals. The Fourier transform infrared spectrum of films revealed no peaks due to impurities. The as-deposited ZnS films had more than 70% transmittance in the visible region. The direct band gap of as-deposited films ranged from 3.68 to 3.78 eV and those of annealed films varied from 3.60 to 3.70 eV. L Qi et al. (2008) [24] have grown ZnS thin films by chemical bath deposition method from $NH_3/SC(NH_2)_2/ZnSO_4$ solutions. The influence on the growth rate of solution composition and the structural, optical properties of the ZnS thin films deposited by this method have been studied. The XRF and XRD analysis showed the high volume of oxygen and cubic structure of ZnS. The XRD analysis of annealed films shows the annealed films were cubic ZnS and ZnO mixture structure. Those results confirmed that the as-deposited films have amorphous $Zn(OH)_2$. SEM studies of the ZnS thin films grown on various growth phases showed that ZnS film formed in the none-film phase was discontinuous. ZnS film formed in quasi-linear phase showed a compact and a granular structure with the grain size about 100 nm. There were adsorbed particles on films formed in the saturation phase. Transmission measurement shows that an optical transmittance was about 90% when the wavelength over 500 nm. The band gap (E_g) value of the deposited film was 3.51 eV. Limei Zhou (2009) et.al.[25] have reported the deposition and structural characterization of zinc sulfide (ZnS) thin films by chemical bath deposition (CBD) from a bath containing thiourea, $ZnSO_4$ and ammonia in aqueous solution on common glass substrates. The solution concentration and annealing condition played a very important role on transmissivity and homogeneity of ZnS thin films. Spectrophotometer, x-ray diffraction (XRD), scanning electron microscopy (SEM), energy dispersive spectroscopy (EDS), digital four-point probe resistance measurement were used to characterize their properties and composition. As a result, transmissivity for the samples were more than 80%. Then it would be stable above 600 nm. The surface morphology showed that the thin films were homogeneous. However, there were some white spots in the SEM patterns that might be colloidal particles sedimentation mixed with ZnS. These particles could be amorphous or non-crystalline. According to the detection, ZnS films resistance were changed with the $ZnSO_4$ solutions concentration.

K. R. Murali (2010) et al. [26] have grown thin films of ZnS by the pulse electrodeposition technique employing zinc sulphate and sodium thiosulphate in diethylene glycol solution at 80°C and at different duty cycles in the range 6–50%. The films were

polycrystalline exhibiting cubic structure. Transmission measurements indicated interference fringes from which the refractive index of the films were calculated to be in the range of 2.30–2.70. The band gap of the films was in the range of 3.66–3.62 eV with increase of duty cycle. The films exhibited resistivities in the range of 400–50 ohm cm with increase of duty cycle. S. S. Kawar (2010) et al. [27] have grown thin films of zinc sulfide (ZnS) by chemical bath deposition technique using aqueous solution of zinc acetate ($Zn(CH_3COO)_2$) and thiourea on glass substrates. After suitable characterization it was found that grain size of ZnS was about 8–130 nm with an optical transmittance more than 70% in the visible range. Optical band gap found from the absorption study was about 3.7 eV. Anuar Kassim (2011) et al.[28] have deposited ZnS thin films onto glass substrate from a chemical bath. The grain size, film thickness and roughness of deposited films were investigated by atomic force microscope and found that the film thickness and surface roughness were mainly dependent on the pH value. The effect of pH on the morphology of the thin films was studied at pH 2, 3 and 4 and found that at pH 2 more nucleation sites had formed as compared with other pH values. S. Nithiyanantham (2011) et al. [29] have deposited zinc sulphide (ZnS) thin films on indium oxide coated glass substrates by photo chemical deposition (PCD) with starting precursor of zinc sulphate and sodium thiosulphate as a source material for Zn and S respectively. In addition the pH was varied (3 to 8) using sulphuric acid by adding up in the precursor. Later the ZnS thin films were annealed at 500°C and it was found that crystalline structure was improved. It was found that average thickness of thin film was about ~1.02 micron with zinc blende crystalline structure. Dong Hyun Hwang (2012) et al. [30] have deposited zinc sulfide [ZnS] thin films on glass substrates using radio frequency magnetron sputtering. The substrate temperature was varied in the range of 100°C to 400°C. The ZnS films have zinc blende structures with (1 1 1) preferential orientation, with a grain size of approximately 69 nm. The films grown at 350°C exhibit a relatively high transmittance of 80% in the visible region, with an energy band gap of 3.79 eV. It was found that these ZnS films were suitable for use as the buffer layer of the $Cu(In, Ga)Se_2$ solar cells.

M. Ashraf (2011) et al. [31] have grown thin films of ZnS on soda lime glass substrates by a modified close-space sublimation technique. The change in optical and structural properties of the films deposited at various substrate temperatures (150–450°C) was investigated. X-ray diffraction spectra showed that films were polycrystalline in nature having cubic structure oriented only along (1 1 1) plan. The crystallinity of films increased with the substrate temperature up to 250°C. However, crystallinity decreased with further increase of substrate temperature and films became amorphous at 450°C. It was found that

band gap of film increased from 3.52 to 3.65 eV with increase of substrate temperature and refractive index of the films were decreased with heating of substrate. Abdullah Goktas (2011) et al. [32] have grown zinc sulfide (ZnS) thin films of different thickness on glass substrates by the sol–gel dip-coating technique. Thickness dependent structural and optical properties of the films were studied in detail. Both the refractive index (n) and extinction coefficient (k) of the films were increased as the film thickness decreased. Electrical measurements showed that the resistivities of the films were decreased as the substrate temperature and film thickness increased.

Sanjeev Kumar (2012) et al.[33] have reported highly reflective and durable coatings using synthesized zinc sulfide-capped thioglycerol nanoparticles. The coating material was prepared by dispersing ZnS/thioglycerol nanoparticles in an acrylic binder. The light reflectors were made applying this coating material to an aluminum substrate, their diffuse reflectance was measured and found to vary from 97% to 100% for 0.30 mm thick coating having 14% pigment-to-binder ratio. The aging effect of the reflectors with respect to temperature and illumination was also investigated to check their durability and they have been found to be optically stable up to 10,000 lux, and thermally up to 80°C. R. Resch (2012) et al. [34] have grown ZnS thin films on a mica substrate by successive ionic layer adsorption and reaction (SILAR) method. The films were deposited in-situ using the commercial AFM liquid cell as flow-through reactor. Reactants and rinsing water were exchanged in the cell continuously by a computer controlled valve system. In this way the film growth could be observed directly in a time resolved sequence of images taken after 1 up to 100 cycles. The results showed that the stability of the films increases between 1 and 30 cycles and that a full coverage of the surface is reached after approximately 50 cycles. A. Vadivel Murugan (2012) et al. [35] have reported the synthesis of nanocrystalline ZnS particles by microwave solvothermal method for optoelectronic device. The effect of different parameters such as time, temperature, solvents, molar ratio of zinc and thiourea on the phase(s) formation of nanocrystalline zinc sulphide was investigated. The obtained nanosize ZnS materials have cubic phase, with bandgap 4.01 eV. The ZnS nano materials were coated on nano porous silicon by screen-printing technique. Luminescence studies indicated room temperature emission in the wavelength ranges from 422.6 to 612 nm, which cover the blue emission to red emission. C. H. Lee (2012) et al. [36] have reported low-pressure metal organic chemical vapour deposition of ZnS thin films on silicon, oxidized silicon and glass substrates using Zn $(C_2H_5)_2$ and C_4H_4S as source chemicals. The growth process and the film properties were characterized as functions of process parameters including substrate

temperature, reactant ratio and reaction pressure. Growth rates increased with reaction pressure and thiophene flow rate depending on the temperature condition. The microstructure indicated that growths above 250^0C possess a cubic (zinc blende) structure, while growths below 150^0C were polycrystalline of wurtzite structure. Zhao(2017) et.al. [37] have used a spin-coating method and ZnS Nanostructures were fabricated into Nafion/uricase/ZnS/ITO electrodes which have been successfully applied for electrochemical and photoelectrochemical UA detection in aqueous solution. The ZnS urchin-like nanostructures based electrochemical biosensor showed the highest sensitivity of 76.12 μ A.cm^{-2}. mM^{-1}. The wide linear detection range from 0.01 mM to 1.7 mM also meets the requirements for diagnosis in clinic. With irradiation of 300 nm UV, its sensitivity of detecting UA is increased 5 times, reaching 413.98 μ A. cm^{-2}. mM^{-1}, which is higher than that of most electrochemical biosensors.

Md. Khalilur Rahman (2018) et al [38]. showed that Cu doped ZnS thin films have found a wide application in the optoelectronic devices. all of the doping elements show that transmittance decreased with increasing concentration because of higher absorption. In the range of transmission 60% - 80% which could be used in various applications of ZnS such as sensors. Moreover ZnS:Cu^{2+} with effective surfactants such as TOPO, SHMP, PEG shows that it helps to reduce crystal size and eliminate defects. Among the surfactants the TOPO molecules are completely covered the ZnS:Cu^{2+} surface and crystallinity is improved. This result indicates the potential applications of the surfactant-capped ZnS:Cu^{2+} nanoparticles in nanoscale fluorescent probes for biological and medical applications. Ultrafine ZnS is a mixture of commercial ZnS powder, while C powder and S powder are successful as a field emitter. Catalytic activities give helps CO_2 reduction with ZnS suspension. As a buffer layer in CIGS solar cell, ZnS is more efficient than CdS which upholds 18.1% of efficiency. The conductance of ZnS nanobelts as a function of oxygen pressure in logarithmic scale utilized as a gas sensor.

3. Conclusion:

In this work we have reviewed the different successful deposition techniques and applications of Zinc sulphide (ZnS) thin films, studied by Various Researchers. Semiconducting ZnS is potentially important material to be used as an antireflection coating for heterojunction solar cells, for light emitting diode, for optoelectronic devices, for electro luminescence devices, photovoltaic cells, for sensors and lasers deposited by Several techniques.

References:

[01] Hammer, K. *Z. Techn. Phys*., 24 (1943) p. 169.

[02] Huldt L , Staflin T. *Opt. Acta*, 6 (1959) 27.

[03] Gonellian, J. *Basic Problems in Thin Films Physics*, R. Niedermayer and H. Mayer (Eds.), Vandenhoeck and Ruprecht,Gottingen, (1996) p. 280.

[04] Nadeem, M.Y., Ahmed, W. *Turk. J. Phys.*, 24 (2000) 651.

[05] Oikkonen, M., Blomberg, M., Tuomi, T. *Thin Solid Films*, 24(3-4) (1985) 317.

[06] Milind D. Bhise, Brian Sanders, Nic Dalacu and Adrian H. Kital *Journal of Materials Science* Volume 24, Number 9 (1989) 3164-3168.

[07] Lindroos, S., Kannianen, T., Leskela, M. *Appl. Surf. Sci*. 75 (1994) 70.

[08] Y. Nosaka, K. Tanaka, N. Fujii and R. Igarashi *Journal of Materials Science* Volume 29, Number 2 (1994) 376-379.

[09] J M Dona, J Herrero *Journal of the Electrochemical Society* Volume: 141, Issue: 1 (1994) 205-210.

[10] Arenas, Olga L.; Nair, M. T. S.; Nair, P. K. *Semicond. Sci. Technol.* 12(1997)1323-1330.

[11] Jie Cheng, DongBo Fan, Hao Wang1, BingWei Liu, YongCai Zhang and Hui Yan *Semicond. Sci. Technol.* 18 No.7 (2003) 676.

[12] A Antony, K V Murali, R Manoj, M K Jayaraj *Materials Chemistry and Physics* Volume: 90, Issue: 1 (2005) Pages: 106-110.

[13] S.D. Sartale, B.R. Sankapal, M. Lux-Steiner, A. Ennaoui *Thin Solid Films* 480–481 (2005) 168–172

[14] Liudmila V Makhova, Igor Konovalov, Rdiger Szargan, Nurdin Aschkenov, Mathias Schubert, Thomas Chass. Physica Status Solidi C Volume: 2, Issue: 3 (2005) 1206-1211.no

[15] Liangyan Chen, Daoli Zhang, Qian Chen 2006 1st IEEE International Conference on Nano-Micro Engineered and Molecular Systems Issue: 20050487034 (2006) 599-602.

[16] Mustafa Oztas, Metin Bedir, Sule Ocak and R. Guler Yildirim Journal of Materials Science: Materials in Electronics Volume 18, Number 5 (2007) 505-512.

[17] A U Ubale, V S Sangawar And D K Kulkarni Bull. Mater. Sci., Vol. 30,

No. 2 (2007) pp. 147–151.

[18] K. R. Murali, J. Abirami and T. Balasubramanian Journal of Materials Science: Materials in Electronics Volume 19, Number 3 (2008) 217-222.

[19] Busarin Noikaew, Panita Chinvetkitvanich,Intira Sripichai And Chanwit Chityuttakan Journal of Metals, Materials and Minerals, Vol.18 No.2 (2008) pp.49-52.

[20] T Bennasr, N Kamoun, C Guasch Applied Surface Science Volume: 254, Issue: 16 (2008) Pages: 5039-5043.

[21] Z. Q. Bian, X. B. Xu,J. B. Chu,Z. Sun,Y. W. Chen,S. M. Huang Surface Review and Letters s(SRL) Volume: 15, Issue: 6 (2008) pp. 821-827.

[22] Reza Sahraei, Ghaffar Motedayen Aval, Alireza Goudarzi Journal of Alloys and Compounds Volume: 466, Issue: 1-2 (2008) Pages: 488-492.

[23] Alireza Goudarzi, Ghaffar Motedayen Aval , Reza Sahraei and Hiva Ahmadpoor Thin Solid Films Volume: 516, Issue: 15 (2008) Pages: 4953-4957.

[24] L Qi, G Mao, J Ao Applied Surface Science Volume: 254, Issue: 18 (2008) Pages: 5711-5714.

[25] Limei Zhou, Yuzhi Xue, Jianfeng Li Journal of Environmental Sciences Volume: 21, Issue: Supplement 1 (2009) Pages: S76-S79.

[26] K. R. Murali, S. Kala and P. Elango Journal of Materials Science: Materials in Electronics Volume 21, Number 12 (2010) 1293-1298.

[27] S. S. Kawar and B. H. Pawar Journal of Materials Science: Materials in Electronics Volume 21, Number 9 (2010) 906-909.

[28] Anuar Kassim, Nani Razak and Ho Soon Min International Journal Of Advanced Engineering Sciences And Technologies Vol No. 7, Issue No. 1 (2011) 169 – 172.

[29] S. Nithiyanantham, R. Gopalakrishnan and K. Ashok Applied Solar Energy Volume 47, Number 3 (2011) 239-242.

[30] Dong Hyun Hwang, Jung Hoon Ahn, Kwun Nam Hui, Kwan San Hui and Young Guk Son, Nanoscale Res Lett. 7(1) (2012) 26.

[31] M. Ashraf, S. M. J. Akhtar, Z. Ali and A. Qayyum Semiconductors Volume 45, Number 5 (2011) 699-702.

[32] Abdullah Goktas, Ferhat Aslan, Eyup Yasar and Ibrahim Halil Mutlu

Journal of Materials Science: Materials in Electronics (2011).

[33] Sanjeev Kumar, N. K. Verma and M. L. Singla Journal of Coatings Technology and Research Volume 8, Number 2 (2011) 223-228.

[34] R. Resch, T. Prohaska, G. Friedbacher, M. Grasserbauer, T. Kanniainen, S. Lindroos, M. Leskelä, L. Niinisto and J. A. C. Broekaert Fresenius' Journal of Analytical Chemistry Volume 353 (1995) Numbers 5-8.

[35] A. Vadivel Murugan, Oh Yee Heng, V. Ravi, Annamraju Kasi Viswanath and V. Saaminathan Journal of Materials Science Volume 41, Number 5 (2006) 1459-1464.

[36] C. H. Lee and C. Y. Pueng Journal of Materials Science Volume 28, Number 3 (1993) 811-816.

[37] Zhao, Y., Wei, X.Y., Peng, N.C., Wang, J.H. and Jiang, Z.D. Volume 17(2017) Sensors, 1235

[38] Md. Anisuzzaman Shakil, Sangita Das, Md. Ashiqur Rahman, Umma Salma Akther, Md. Kamrul Hassan Majumdar, Md. Khalilur Rahman, Materials Sciences and Applications , Vol.9 No.9 August 2018, 751-778.

Paper-18

Study of Assisting Tools like Pin-on-Disc to Determine Tribological Factors of Microhardness and Coefficients of Friction for Thin Film Coatings on Industrial Tools

Goswami Vishal H
Assistant Professor
Department of Physics
Chikitsak Samuha's Sir Sita Ram and Lady Shanta Bai Patkar College of Arts and Science and V. P. Varde College of Commerce and Economics, S.V Road, Goregaon (W), Mumbai

ABSTRACT

Using Pin-on-Disc to test and evaluate factors such as microhardness and coefficients of friction helps extend into the impact of thin film coating on different metals for industrial use. The coating thickness, microstructure of such thin films depends on the size of the grain, biased voltage, cathodes, and the nitrogen flow rate. In this study, there exists a testing mechanism that allows to evaluate the hardness and the protection received by industry tools on the basis of thin film coatings, which have proved to surpass load and pressure to ensure a more efficient industrial tool.

Keywords: pin-on-disc, Microhardness, Coefficients of Friction, base material, industrial tools, thin film coating, wear-resistance, coating systems.

Introduction

A recent research study resulted in the development of high-performance metals with enhanced surface properties. These materials are highly engineered to perform the world's most technically demanding applications. These materials offer properties such as high temperature, corrosion resistance, strength, electrical properties and controlled thermal expansion. The demand of the twenty-first century is "thin film technology." It is a well-established coating technology for the development of new nanostructured materials. These technologies are still evolving on a daily basis.

One of the most important areas in which such coatings have been used is that of the cutting tool industry where nitrides, carbides, and carbo-nitrides films of transition metals have been used to increase the lifetime of the tool or component Research on optimization of different performance parameters, including high hardness, good ductility, excellent lubricity, high chemical stability, and toughness of coating showed improve tribological performance of components [1, 2]. C. Lorenzo-Martin et al. focused on applications like cutting and forming tools, dies, and automotive components. In their work, the effects of the thickness and microstructure of the coating on parameters like friction and wear behavior of CrN coatings were studied [3].

Another study on the basis of microstructure, mechanical properties, and wear mechanisms completed their paper. Douglas E. Wolfe et al. discussed the synthesis and characterization of ((Ti,Cr)N) thin films on AM355 and analyzed the ways of improving erosion resistance [4]. According to Shinya Sasaki, environment-friendly tribology, eco-tribology, through progress in surface modification, is seen as an effective engineering technology that contributes to sustainable societies. As per the paper, multi-scale surface texturing enhances the tribological properties of materials, and diamond-like carbon coating (DLC) technology would be an expected future development [5].

Techniques Used for Analysis of the Thin Film Coating Structure

The tribological and morphological behavior of the thin films deposited is not fully understood and its effects on various industrial tooling components. This study manages to

have a glimpse of the microstructure that is thin film coatings bear.

Pin-on-Disc Test

The Pin-on-Disc tester helps study the tribological characterization and characteristics of materials, lubricants, and so on. The Pin-on-Disc test requires two specimens:

1. A pin with a circular tip
2. A flat circular disc

The pin is situated perpendicular to disc and the tip of the pin is circular with a radius of 5 mm. The test motor attached to the Pin-on-Disc tester rotates either the disc or the pin. In both cases, the sliding path is circular on the surface of the disc. The disc stands either vertically or horizontally. The pin presses over the disc at a predetermined load applied using a lever or arm attached to a dead-weight load. In some instruments, the applied load uses hydraulic or pneumatic methods. The circular wear scars developed on the disc is a result of multiple rotation on the same track. The friction force can be determined by using the measuring system, for example, the use of a load cell, allowing the coefficient of friction to be determined.

Calculation of Coefficient of Friction:

The coefficient of friction was determined by dividing the friction force (FF) and the normal load exerted on the pin by the testing machine's deadweight during Pin-on-Disc Test.

Let the tip of the pin be circular with radius (r), hence to find the area of the cross-section (A) the following formula is used,

$$A = \pi r^2$$

To calculate Contact Pressure,

$$\text{Contact Pressure} = \frac{\text{load}}{\text{area}}$$

Therefore, the coefficient of friction (COF) is obtained as follows,

$$\text{coefficient of friction} = \frac{\text{friction force}}{\text{load}}$$

Microhardness Test

The hardness of the coatings produced for industrial applications of tool steel is an important consideration. It is important to accomplish sufficient hardness for controlling the deformation of edges and critical dimensions.

For micro-indentation hardness measurements, soft or malleable films may not withstand the force of piercing therefore, during testing a low normal load is applied using the Diamond tip. The best technique for low load indentation tests can be achieved by three diamond tips, used for mechanical testing: Conical, Berkovich, and Vickers as shown in the figure.

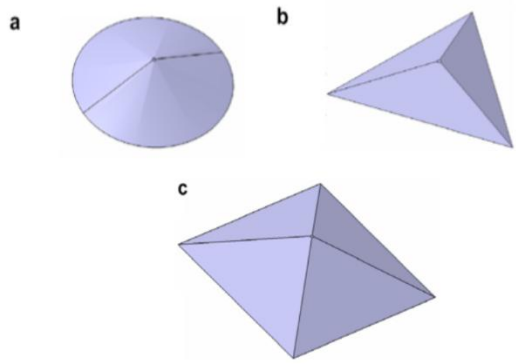

Indentation geometries for (a) Conical, (b) Berkovich, and (c) Vickers tips

Berkovich and Vickers are most commonly used for micro indentation to determine the hardness of coatings. When applying a load to a material, this material experiences elastic displacement and some residual deformation. Hence, low loads avoid deforming the substrate material, which would yield false information on the properties of the film. Depending on the film thickness, density, and hardness of the film, a suitable value of indentation load helps to measure the microhardness of coatings. During this procedure, the tip presses itself against the sample surface for around two seconds at suitable low indentation loads. Measurements are taken before and after the indentation to determine the surface's topography.

Calculation of Hardness:

To calculate hardness, normal load is applied using the Diamond tip indenter, where the indentations will be marked. The hardness is calculated by the following two methods:

1. Measuring the length of the diagonals and converting the diagonal lengths to

a hardness number related to the load of the indentation.

2. Hardness is obtained by dividing the indentation load (F_L) by the projected residual area (A_p),

$$H = \frac{F_L}{A_P}$$

Results and Analysis of Thin Film Coating Structures

The constant need for improvement and the competitive nature of industries have pushed researchers to find more adequate coatings that protect the base metal in harsh manufacturing and production environments. The demands have increased the need to showcase evidence to support the role of thin film coating technology in the production of strong base metals that can withstand wear and tear and improve longevity, thus contributing to productivity and profitability. As a research unit, arriving at such conclusions helped this study to understand the evaluation mechanisms that can bring in a true picture of the coating technologies available and potentially enhance the most recent search for the appropriate tribological and chemical factors that promote base metal enhancement.

Pin-on-Disc Test

While performing the pin-on-disc test on the Plint TE 70SLIM reciprocating machine under dry lubricated conditions, the study establishes tribological parameters like the sliding wear and coefficient of friction. These values helped determine the characteristics of the materials and the lubricant. In these experiments, the aluminum bronze pin and the coating on a 22-mm-diameter HSS disc helped perform various tests under dry lubricated conditions. The material of the coated disc and the material of the pin purposively helped simulate the sliding part of any industrial tooling and workpiece.

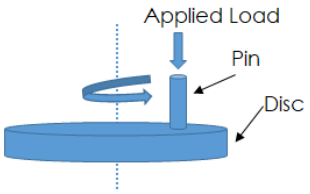

General diagram of the Pin-on-Disc machine

A brief on the pin-on-disc tester showcases it as a horizontal rotating disc (in this case, the study used a coated sample) and a calibrated deadweight-loaded aluminum bronze pin. The tests were conducted under an average vacuum of 420 mbar, a relative humidity of 59 Rh% to 62 Rh%, at 20 °C to 24 °C chamber temperature and 26 °C to 30 °C pin temperature. The test considered loads of 5 N, 10 N, and 15 N for durations of 15 minutes each. Several tests helped achieve a sense of accuracy in the calculations and results. During the testing, the tip of the pin and disc rotated, and the friction force, normal load, and vertical displacement of the pin were documented continuously. The following table represents the average data achieved after process stabilization for comparison of the results:

On analysis of the data, it is found that like DLC (diamond-like carbon) and WC/C, the thin film coatings deposited using the ACAD process not only improves wear resistance but also lowers friction coefficients that lead to high efficiency and usability in heavy load-carrying applications. This analysis was a clear indication to encourage higher use of Cr and Ti based nitride, carbide and carbonitride coatings in industries like the field protective, decorative and tool-making industries, and even the key ingredient in multilayer or bilayer multicomponent coating systems to produce harder and highly wear-resistant tools for cutting and reshaping.

In this experiment, the pin was pressed by a mechanical dead load and skidded against the rotating disc in the presence of abrasive fluid. As the pin passes above the surface of the coated disc, it triggers a tribochemical reaction within the abrasive fluid that gradually deposits a thin film on the surface of the disc. Pressure applied on the pin leads to a rubbing effect because of which valleys were created, and due to the chemical reaction with the abrasive fluid thin tribo-film gradually deposited in the valley during the process. The microscopy/SEM technique inspected these valleys / wear scars to identify the types of wear debris and their dimensions.

	Time (S)	FF (N)	Wear (micron)	Load (N)	COF	Pin T (deg c)	Contact. P (N/mm^2)
CrN 5N	899.873	7.279	1.417	4.877	1.500	26.608	0.062
CrN 10N	899.475	7.308	1.496	9.942	0.735	28.999	0.127
CrN 15N	899.4	8.375	3.041	14.932	0.561	30.168	0.190

TiN 5N	899.938	4.808	3.262	4.926	0.977	25.171	0.063
TiN 10N	899.442	5.639	3.685	9.983	0.565	27.671	0.127
TiN 15N	899.837	8.274	4.785	14.958	0.553	28.054	0.190
TiC 5N	899.531	6.304	2.260	4.858	1.299	26.543	0.062
TiC 10N	899	6.726	2.520	9.968	0.675	27.148	0.127
TiC 15N	898.978	7.886	3.434	14.929	0.528	28.067	0.190

CrCN 5N	900.024	3.508	1.185	4.859	0.922	27.568	0.062
CrCN 10N	899.428	8.595	1.698	9.960	0.863	28.647	0.127
CrCN 15N	899.272	11.471	2.863	14.915	0.769	27.957	0.190

Tribo parameters of CrN, TiN, TiC, and CrCN thin films under loads of 5 N, 10 N, and 15 N for a duration of 15 minutes

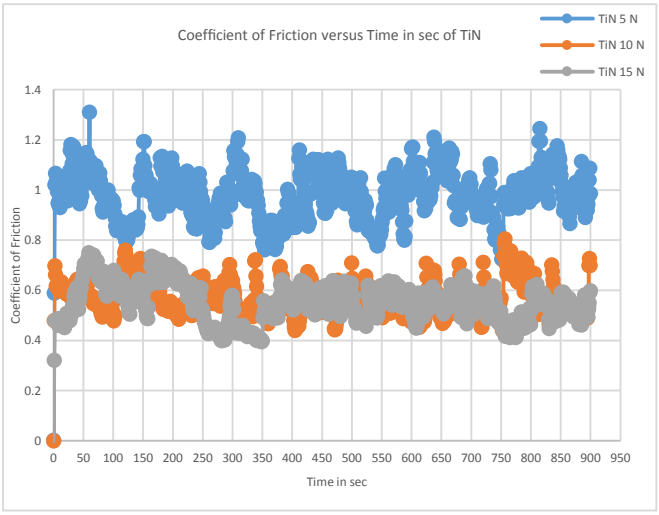

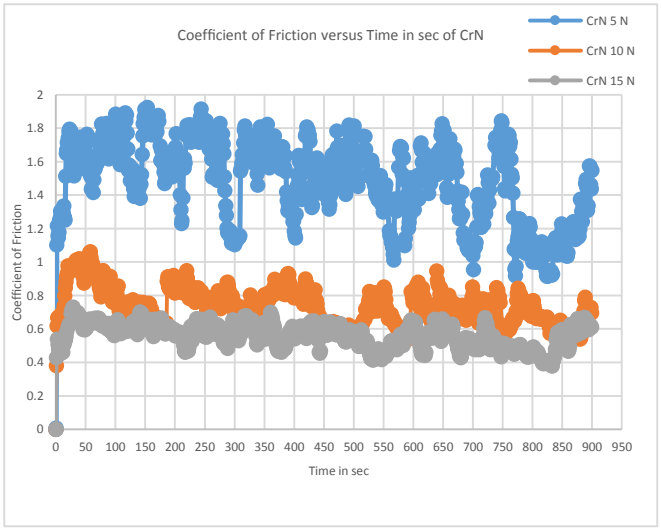

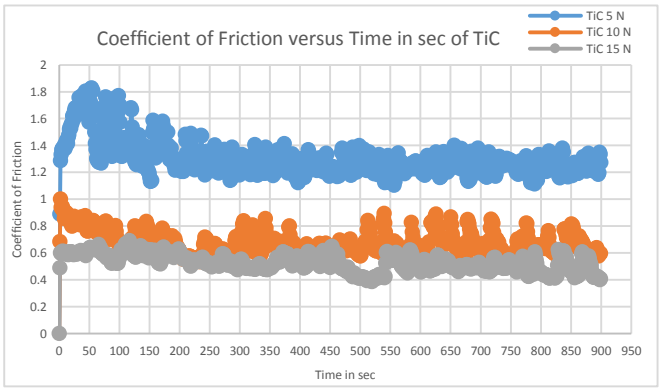

Graphs of Coefficient of Friction versus Time in sec

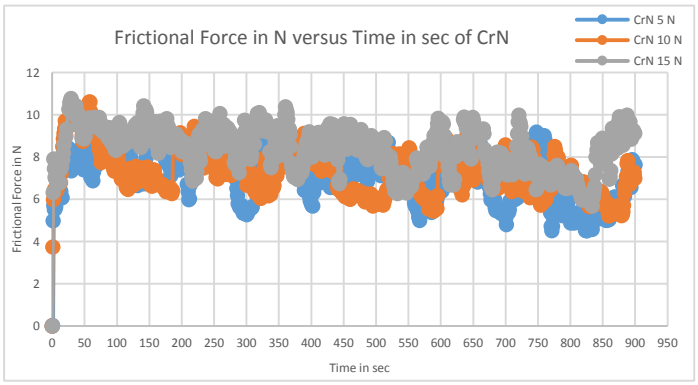

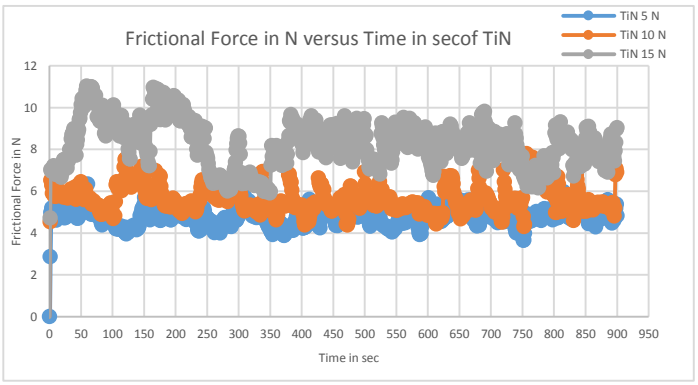

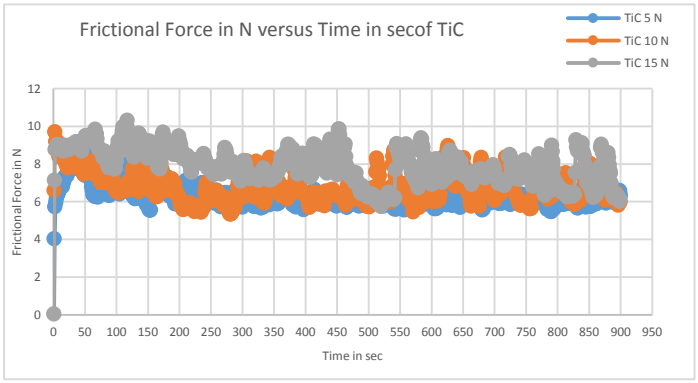

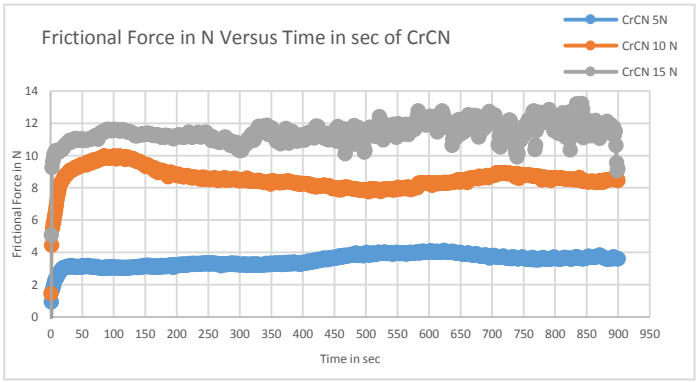

Frictional Force in N versus Time in sec

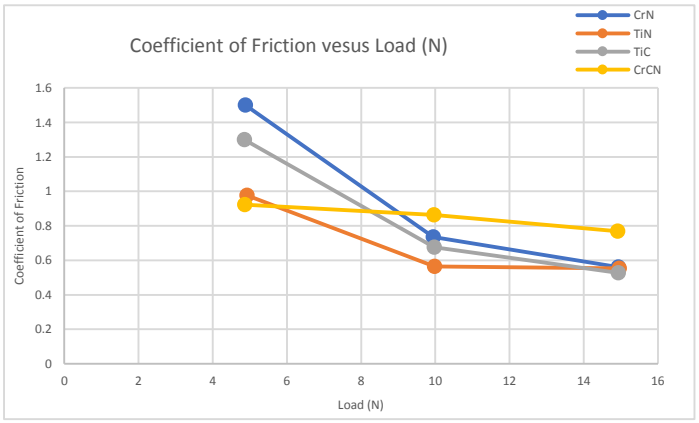

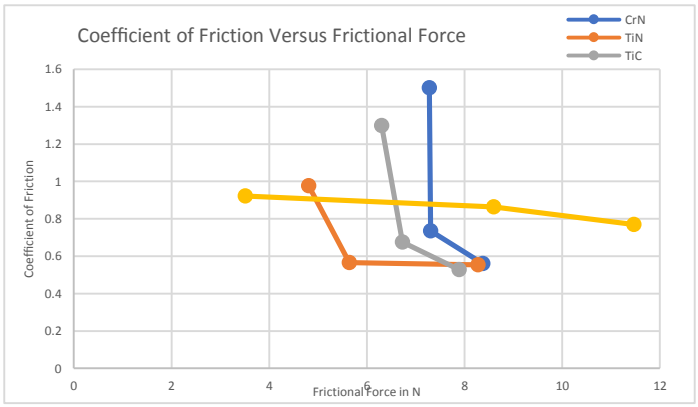

Average Coefficient of Friction versus Load (N)

Average Coefficient of Friction versus Frictional Force (N)

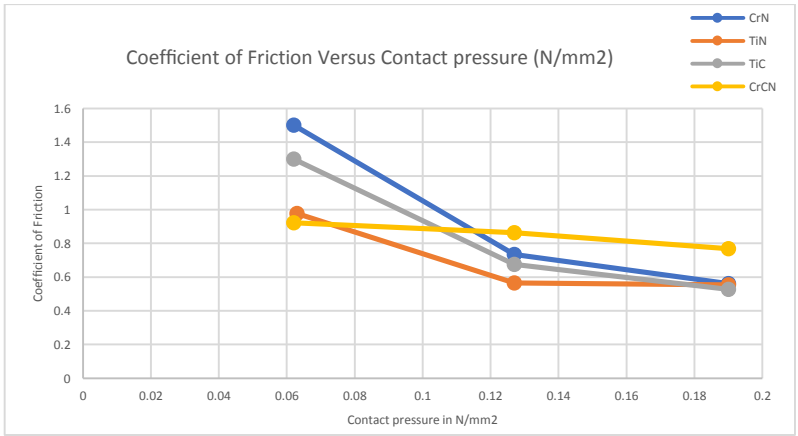

Average Coefficient of Friction Versus Contact pressure (N/mm²)

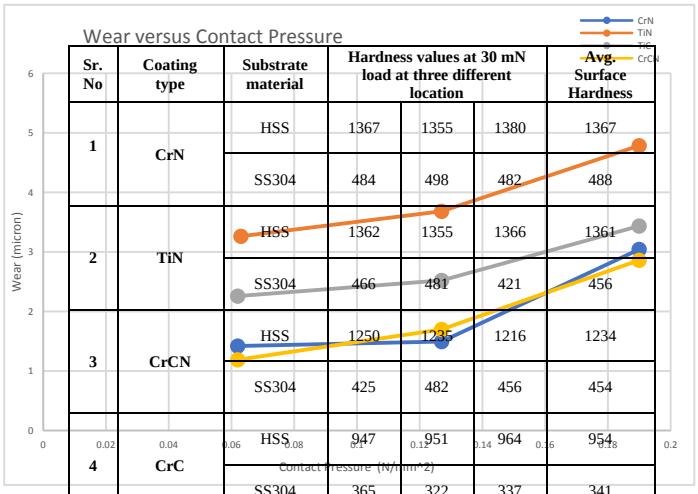

Sr. No	Coating type	Substrate material	Hardness values at 30 mN load at three different location			Avg. Surface Hardness
1	CrN	HSS	1367	1355	1380	1367
		SS304	484	498	482	488
2	TiN	HSS	1362	1355	1366	1361
		SS304	466	481	421	456
3	CrCN	HSS	1250	1235	1216	1234
		SS304	425	482	456	454
4	CrC	HSS	947	951	964	954
		SS304	365	322	337	341
5	CrN/ CrC	HSS	987	973	966	975
		SS304	547	556	567	557
6	TiN/CrC	HSS	895	858	873	875
		SS304	481	487	472	480
7	CrN/TiC	HSS	714	770	758	747
		SS304	656	670	660	662
8	M-CrN-16 layer	HSS	1261	1270	1265	1265
9	Uncoated: HSS	HSS	1010	995	1017	1007
10	Uncoated: SS304	SS304	266	263	268	265

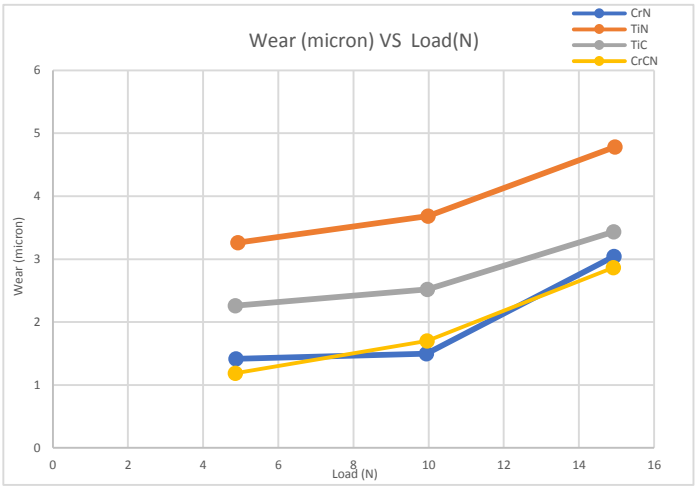

Wear versus Contact Pressure (N/mm²)
Wear versus Load (N)

Microhardness Test

In this study, the hardness of coatings was determined using Micro Vickers hardness testing machines (HM-200) at a load of 30 mN were used to avoid contributions and deformation of the substrate material which would yield false hardness values (i.e. hardness values below the true value). The diagonals of the indentation were measured using a metallographic microscope. These values were averaged by indenting at three different locations of coatings, and hardness was determined using a table of microhardness values. Irregularities in the surface condition and coating composition contributed to the many variations in the hardness data set. The microhardness analysis of various deposited coatings on high stainless steel and on stainless steel-304 is shown in the above table.

Microhardness analysis of various deposited coatings

The use of technologies like SEM and EDS, along with tools like Pin-on-Disc, further promote the accurate calculation and analysis of surface coatings and encourage surface engineering projects, pertaining to various industries, manufacturing units, and organizations. The varied tests on monolayer, bilayer, and multilayer coatings gave a wider and expansive look into each type of surface coating, enabling this study to get a finer understanding of the applicability of each coating. With the types of uses changing with the technological inkling, it became a necessity to develop newer methods to provide tool manufacturers with an acute understanding of how important the various features, like hardness and coefficients of friction, compile in the making of tools. It is not only the underlying material to be questioned but also surface engineering plays a vital role in supporting the lifespan of tools, their resistance to corrosion and various abrasive environments, and far-from-normal conditions, like heat, humidity, acidic and wet atmospheres. Each value brought us closer to knowing the intricate properties of monolayers like TiN, CrN, bilayers like CrN/TiC, TiN/TiC, CrN/CrC and TiN/CrC, and multilayers like M-CrN.

Conclusion

The present work evidently reports the possibility of defining the tribological properties of industrial engineering steel as per the requirements of the operation. It was conclusive that by regulating the substrate's hardness, the materials can be put to use across

industrial applications. Many such combinations give us better control to define the end properties of the coating structures and cater to the need of the application. Utilizing Pin-on-Disc testing and arriving at the coefficients of microhardness inched the study closer to understanding the contribution of various thin film coatings in the preparation of grade-A industrial tools and applications.

Acknowledgements

The author acknowledges the assistance received from Bhabha Atomic Research Centre (BARC), Mumbai, India and IPR (Gujrat) for the help in characterization, evaluation of samples and for their constant support. The author would also like to acknowledge Surface Modifications Pvt. Ltd., Vasai – Palghar, India for having rendered the experimental facilities for the present work.

References

1. E. Vancoille Mechanical et al. "properties of heat treated and worn PVD TiN, (Ti, A1)N, (Ti, Nb)N and Ti(C, N) coatings as measured by Nanoindentation." Thin Solid Fihns, 224 (1993) 168 176.

2. Mahesh R. Chavda et al. "Tribological Characterization of TiN Coatings prepared by Sputtering" Procedia Technology 23 (2016) 36 – 41.

3. C. Lorenzo-Martin et al. "Effect of microstructure and thickness on the friction and wear behavior of CrN coatings" Wear 302 (2013) 963–971.

4. Douglas E. Wolfe et al. "Nanolayer (Ti,Cr)N coatings for hard particle erosion resistance" Surface & Coatings Technology 205 (2011) 4569–4576.

5. Shinya Sasaki "Environmentally friendly tribology (Eco-tribology)" Journal of Mechanical Science and Technology 24 (2010) 67~71.

Paper-19

Dielectric and Mobility Profile of NADAC-ADC Co-Polymer

Neerja[1]

[1]Department of Physics, DAV College, Amritsar-143001, India

Abstract: We present here, the first report of dielectric studies, carrier mobility and underlying conduction mechanism of a newly developed co-polymer (NADAC-ADC) of N-allyloxycarbonyl diethanol-bis allylcarbonateamine (NADAC) and allyl diglycol carbonate (ADC). Admittance spectroscopy was carried out on NADAC-ADC over six orders of frequency at different bias voltage. Dielectric constant and carrier mobility of the polymer have been found to vary between 5.1 to 5.6 and 3.4 X 10^{-4} $cm^2V^{-1}s^{-1}$ to 9.8 X 10^{-4} cm^2 $V^{-1}s^{-1}$ respectively. The polymer showed a cross over from high loss behavior (Low Frequency Dispersion) to low loss behavior at high frequency. Spectroscopic variation of complex impedance, capacitance, complex electric modulus and Nyquist impedance plot are also being presented. The phase of complex admittance curve has been simulated to obtain an insight into the contribution of grains and grain boundaries overall impedance of the polymer. The conduction mechanism extracted from the AC conductivities of the polymer was found to be hopping in nature. Despite poor π-conjugation in the polymer structure, the exhibited values of carrier mobilities have been found to be impressive, from the perspective of their potential use as one of the active layers in multi-layer spectral splitting module of photovoltaic cells.

Introduction

In last few decades organic and polymeric materials have been extensively investigated for their potential applications in the field of photovoltaic cells[1-6], radiation dosimetry[7-10], organic light emitting diodes and other optoelectronic devices[11-13]. For device optimization and its control, the

knowledge of the fundamental material parameters like carrier mobility, complex dielectric function, complex admittance and their respective spectroscopic dependence on wide range of frequencies is extremely essential. Study of relative contribution of grains, grain boundaries and junctions to overall impedance and the range of frequencies where each contributor becomes significant, may lead to better insight into microscopic level understanding of conduction mechanism. In the present work, complete dielectric profiling of newly developed co-polymer NADAC-ADC[14] has been done. NADAC-ADC (fig. 1) is co-polymer of N-allyloxycarbonyl diethanol-bis allylcarbonateamine (NADAC) and allyl diglycol carbonate (ADC or commonly known as CR-39). The polymer reportedly exhibits significant applications in the field of radiation dosimetry, where the dielectric constant strongly affects the track registration ability of the material[15]; yet, no investigation has been reported to provide a complete dielectric profile of the NADAC-ADC. Apart from their applications in radiation dosimetry, the present study will help in exploring use of NADAC-ADC in photovoltaic and optoelectronic applications. Earlier reported optical investigations of NADAC-ADC exhibited its significant absorption in near UV region of solar spectrum. Further, this absorption band shows a red shift on gamma irradiation[15]. Thus, this ability to modulate absorption band of NADAC-ADC increases its potential to be used as one of the active layers of multi-layer photo voltaic cell module. Keeping this end objective in consideration, admittance spectroscopy of the NADAC-ADC has been done over six orders of frequency range to obtain all the key parameters.

Experimental Procedures

NADAC-ADC co-polymer was prepared in the laboratory, details of which were published earlier elsewhere[14]. The thickness of the film was measured using digital micrometer and was found to be (508 ± 5) µm. This self-standing polymer uniform film was investigated in the frequency range from 10 Hz to 10^6 Hz using Hioki 3532 LCR meter and Autolab NOVA 1.10.1.9 impedance analyzer at different bias voltages. The obtained admittance phase curves were simulated with mean square error less than one.

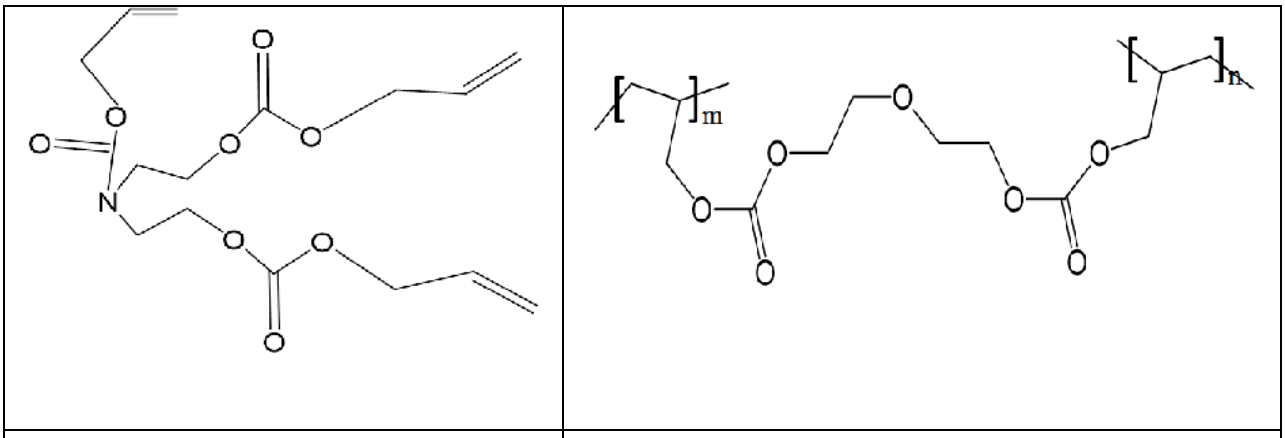

(a)	(b)

Figure 1: Monomers of (a) NADAC and (b) ADC polymer

Results and Discussions

Figure 2 (a) and (b) shows the variation of capacitance and dielectric constant of the NADAC-ADC polymeric self-standing film with frequency, at different bias voltages.

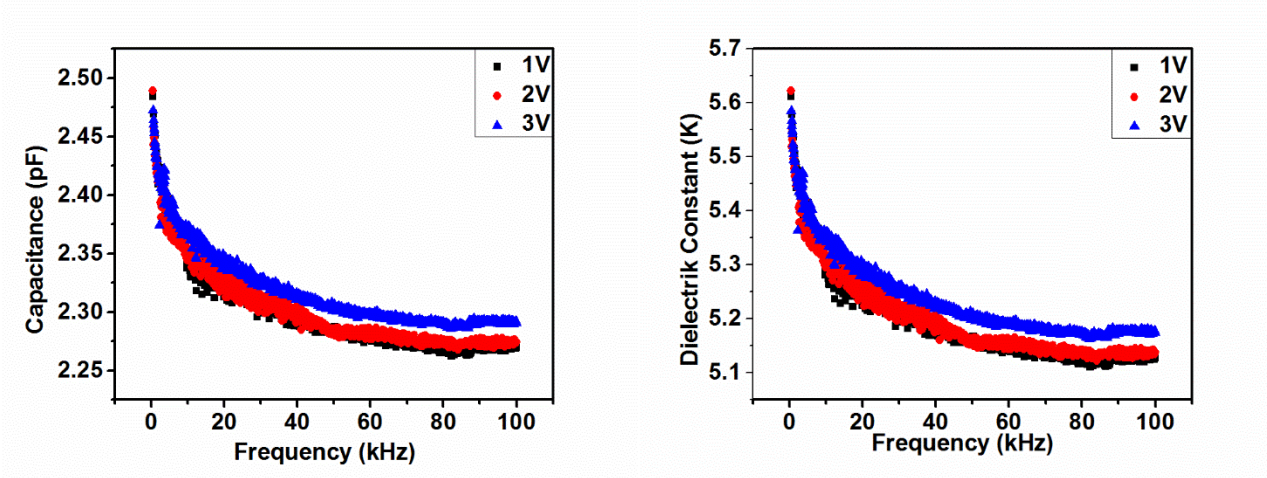

(a) (b)

Figure 2: Spectroscopic variation of (a) capacitance (b) dielectric constant of NADAC-ADC self-standing films

NADAC-ADC films show high capacitance and high dielectric constant at low frequencies however the both parameters show steep fall, attaining asymptotic values at higher frequencies. The capacitance of the self-standing films was found to fall from 2.5 pF to 2.25 pF. This behavior is well explained on the basis of Goswami and Goswami[16] equivalent circuit model. According to this model, at low frequency, the inherent dipoles tend to follow the oscillations of external bias but fail to do so at higher frequencies, thus, two terms contribute to the overall capacitance of the film (equation 1). The first component is a frequency independent term corresponding to the geometric capacitance of the film. The second component is a frequency dependent term due to the floating polarons in the oscillating external coulombian field.

$$C = C_{geo} + 1/\omega^2 R^2 C_{geo} \quad (1)$$

where R is temperature dependent resistive term. As the frequency of the external bias increases the contribution of the second term diminishes and the capacitance of the film acquires its asymptotic value (C_{geo}). The dielectric constant, the real part of complex dielectric function ($\varepsilon = \varepsilon' + i\varepsilon''$) of the NADAC-ADC polymer was determined using the relation $\varepsilon'=K=C\ d/A\varepsilon_0$, where A, d and ε_0 are effective area of the capacitor, film thickness and absolute permittivity of vacuum. The dielectric constant was found to lie in the range 5.1 to 5.6. The imaginary part of the complex dielectric function (ε'') shows a similar behavior over investigated frequency domain and is shown in figure 3(a).

The carrier mobilities play a crucial role in the performance of light harvesting devices, as the polarons generated by the incident light need to be transported to the electrodes before their self-annihilation. Therefore to explore the role of NADAC-ADC as one of the active layers in the multi-layer spectral splitting module of solar cells, carrier mobility of the film has been determined through admittance spectroscopy[17-21]. The complex admittance of the film is given by equation (2)

$$Y = G + iB \quad (2)$$

where G is conductance and B (= ω C) is susceptance of the film. The variation of frequency dependent capacitance gives a peak in the negative differential susceptance ($-\Delta B = \omega(C-C_{geo})$) versus frequency curve at the relaxation frequency of the carriers. The relaxation frequency is related to the transit time and the mobility of the carriers as

$\tau = 0.56/f_r$ and $\mu = d^2/V\tau$ (3)

where, f_r is the relaxation frequency corresponding to the peak in the negative differential susceptance curve, τ is the transit time, d is film thickness, V is the applied bias voltage and μ is the carrier mobility[22-24]. Figure 3(b) shows the variation of $-\Delta B$ with frequency at different bias voltage. The mobility of the charge carriers through the NADAC-ADC films has been found to lie in the range 3.3 X 10^{-4} $cm^2V^{-1}s^{-1}$ to 9.8 X 10^{-4} cm^2 $V^{-1}s^{-1}$ (Table I). The obtained values are comparable to reported values of carrier mobilities for many front running polymeric semiconductors materials being used in the field of light harvesting and optoelectronic devices (Table II).

Further, the dissipation factor (or loss tangent) was determined as a function of frequency for NADAC-ADC polymer film (Figure 4). Typically a dielectric material is said to be lossy if the tangent loss is more than 0.1 and is called low loss dielectric if tangent loss is less than 0.01[25]. As the frequency of the external bias increases, the field reversal and dipole reorientation do not occur in phase, leading to dipole relaxation and low loss behavior. The NADAC-ADC polymer clearly exhibited high loss in the low frequency region, often termed as low frequency dispersion (LFD). However, NADAC-ADC films showed a cross over from LFD to low loss behavior at higher frequency region confirming dipole relaxation phenomenon[25].

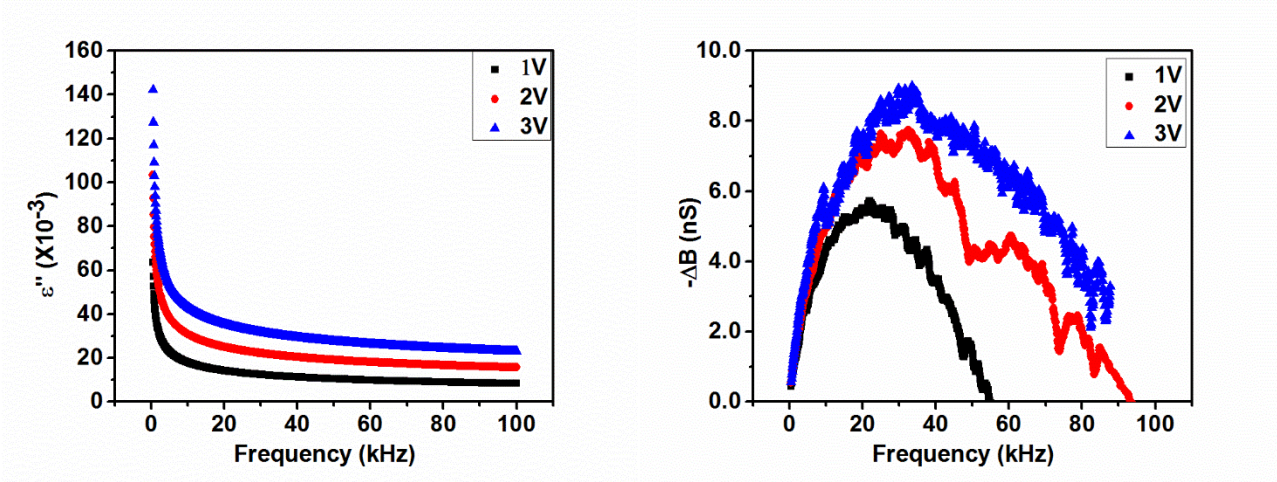

(a) (b)

Figure 3: Variation of (a) imaginary part of complex dielectric function (ε´´) and (b) negative

differential susceptance of NADAC-ADC film

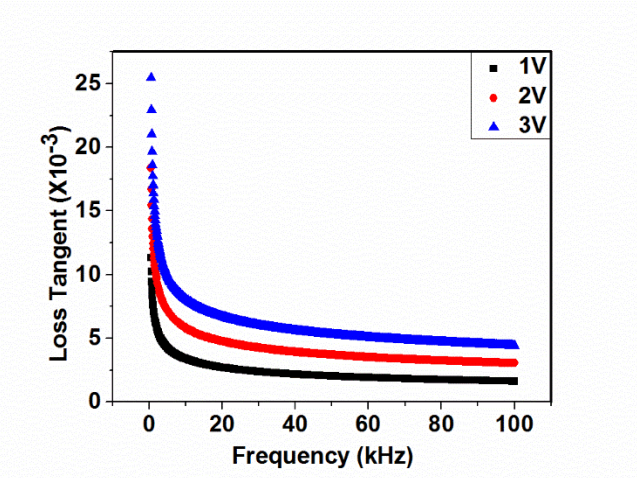

Figure 4 : Variation of loss tangent with frequency at constant bias voltage

To understand the nature of conduction mechanism through the polymer films its AC conductivities were measured at different bias voltages (Figure 5). NADAC-ADC film showed a plateau in the low frequency region and rising sharply at higher frequencies. This behavior is well explainable according to universal power law of AC conductivity of a material (equation 4).

$$\sigma = \sigma_0 + A\omega^n \qquad (4)$$

where σ is the AC conductivity at angular frequency ω, σ_0 is DC conductivity, A is conductivity pre-factor and 'n' is the exponent of the power law. The power law exponent gives information about the conduction mechanism through the material. In dielectric materials the electron and hole remain bound by coulombian forces and thus remain confined to a potential well. These confined carriers can tunnel through from one potential well to another and the phenomenon is often termed as charge hopping[26, 27]. The frequency of hops between these potential wells is given by the equation[28] (5).

$$f_{hop} = (\sigma_0/A)^{1/n} \qquad (5)$$

The AC conductivity curves (Figure 5) were fitted with equation (4) and the obtained parameters are reported in Table I. The DC conductivity and the power law exponent show an increase with

increase in the bias voltage. The values of 'n' obtained for NADAC-ADC film are less than one, which is typical for hopping nature of conduction mechanism. The obtained hopping frequencies are low due to poor conjugation in the polymer structure, leading to scarcity of hopping sites for the carriers, however it increases with increase in bias voltage.

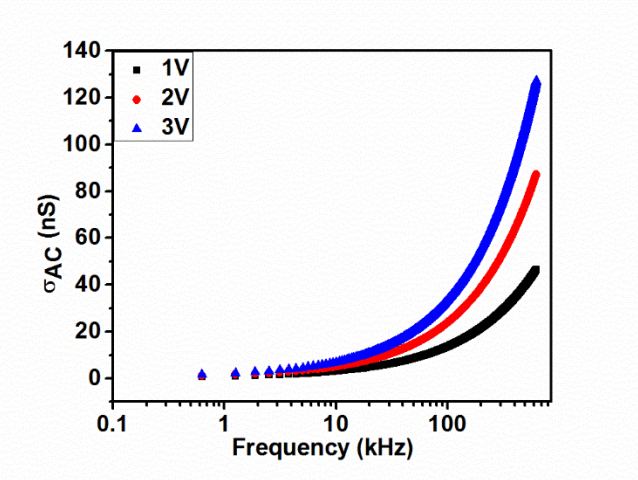

Figure 5: AC conductivities of NADAC-ADC polymer film at different constant bias voltage

Further, electric modulus M' and M'' have been calculated using equation (6) and (7)

$$M' = \varepsilon' / (\varepsilon'^2 + \varepsilon''^2) \quad (6)$$

$$M'' = \varepsilon'' / (\varepsilon'^2 + \varepsilon''^2) \quad (7)$$

Table I: Mobility, Conductivity parameters and hopping frequency for NADAC-ADC film

Bias Voltage ⟶ / Mobility and Conductivity Parameters ↓	1V	2V	3V
Mobility ($cm^2V^{-1}s^{-1}$)	3.3×10^{-4}	4.9×10^{-4}	9.8×10^{-4}
DC Conductivity σ_0 (S/m)	3.31×10^{-10}	6.73×10^{-10}	1.04×10^{-9}
Pre-factor (A)	1.83×10^{-11}	2.17×10^{-11}	2.51×10^{-11}
Exponent in Power Law (n)	0.68	0.72	0.74
Hopping Frequency (Hz)	70.6	117.9	153.3

Table II: Carrier mobilities of some other polymeric semiconductors currently being used in the field of light harvesting and optoelectronic devices.

Polymer	Carrier Mobility ($cm^2V^{-1}s^{-1}$)	Reference
PCBM	~ 10^{-3}	Yokohama et al.[29]
MDMO-PPV	~ 10^{-4}	Serap Gunes et al.[1]
P3HT	~ 10^{-1}	Sirringhaus et al.[30]
Spiro-CPDT	~ 10^{-6} to 10^{-3}	Wei-Jie Chi et al.[31]

Figure 6 shows the variation of M′ and M′′ with frequency at different bias voltages. M′ showed a steep rise in low frequency region reaffirming low frequency dispersion for the polymer film. No peak was observed in M′′ curve indicating long range conduction mechanism dominating hopping conduction in low frequency domain[32].

To estimate the contribution of grains and grain boundaries to the overall impedance of the NADAC-ADC films, a Nyquist plot between real part (Z′) and imaginary part (-Z′′) of the impedance was produced (Figure 7a). The Nyquist plot showed two semi circles with their centers above the real axis. The area under bigger semi-circle in the low frequency region indicates the contribution of the grains boundaries whereas the area under the smaller semi-circle indicates the contribution of grains to the overall impedance. The Nyquist plot indicates that there is not much contribution to the impedance from the interface formed by silver electrode on the polymer film. As the centers of the semi-circles lie above the real axis, it suggests there was an inherent phase difference between the series resistance and the impedance of the film which can be attributed to capacitance contribution of the grain boundaries. To further understand the contribution of various terms to Nyquist plot, the experimentally obtained phase of the complex admittance ($\phi = \arctan\left(\frac{Y''}{Y'}\right) = \arctan\left(\frac{\omega C}{G}\right)$) was simulated obtaining mean square error less than one (Figure 7b). From the developed equivalent circuit diagram by simulation (Figure 8), it is clear that at high frequencies of the external bias, the low impedance path is offered by the parallel capacitors (C1 and C2), leading to increase in imaginary component of Y. This mechanism is confirmed by a clear spur in the high frequency region of phase (ϕ) versus frequency curve.

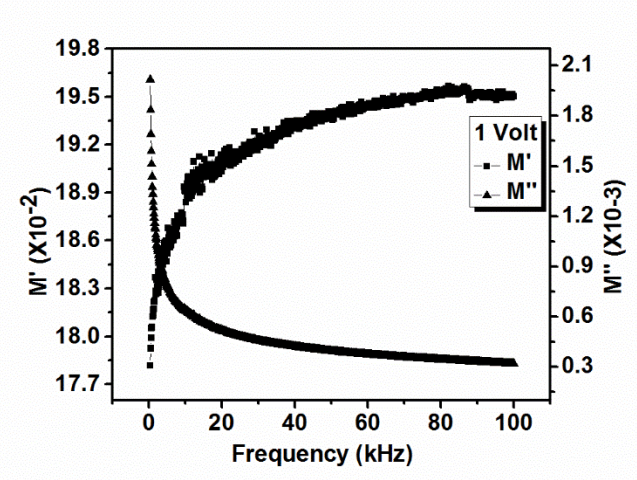

(a)

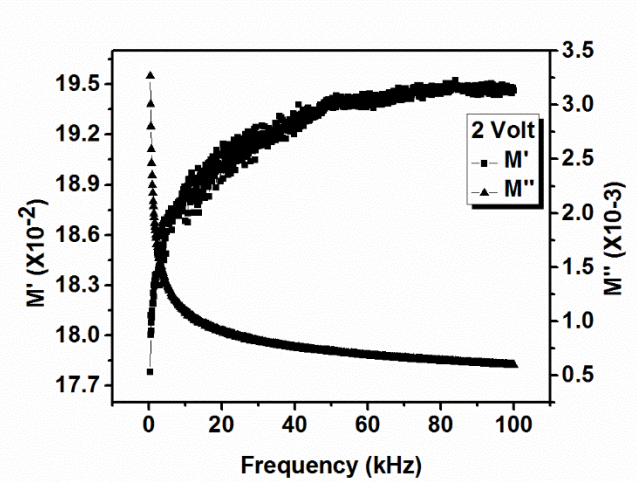

(b)

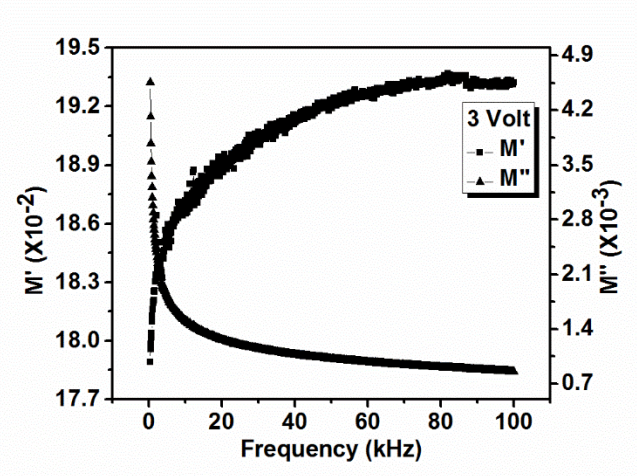

(c)

Figure 6 : Variation of electric Modulus M' and M'' with frequency at (a) 1V (b) 2V (c) 3V

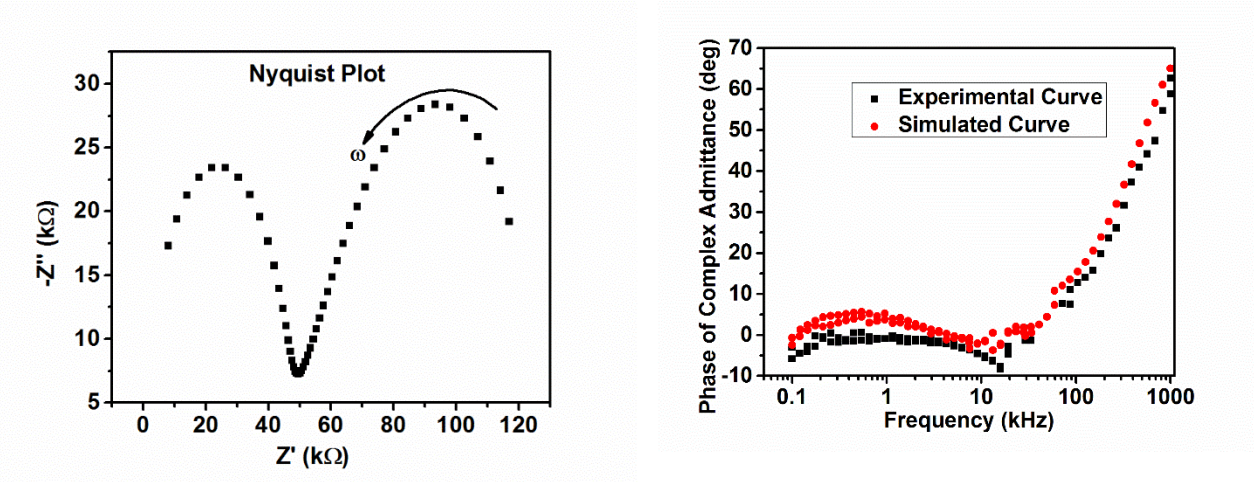

(a) (b)

Figure 7: (a) Nyquist plot and (b) experimental and simulated phase of complex admittance curve of NADAC-ADC polymer film with a spur in the high frequency domain

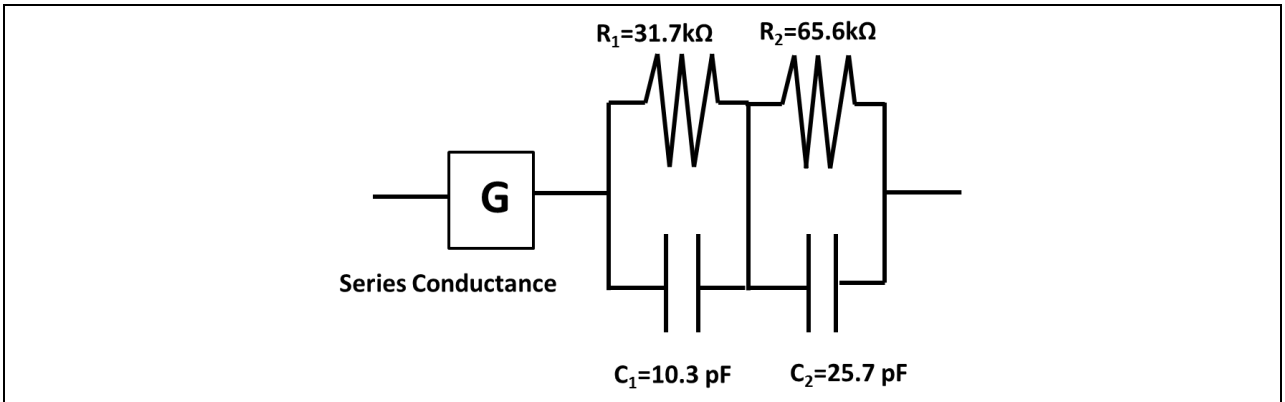

Figure 8: The equivalent circuit diagram for the NADAC-ADC film

Conclusions

In the present work, a complete dielectric profile of a co-polymer NADAC-ADC is being presented. The dielectric constant of the polymer was found to be lying in the range of 5.1 to 5.6. Despite poor π-conjugation in the polymer structure, polymer exhibited impressive carrier mobilities of the order of 10^{-3} $cm^2V^{-1}s^{-1}$. The AC conductivity curves indicated a hopping nature of conduction through the NADAC-ADC film. The film showed a cross over from high loss

behavior (low frequency dispersion) to low loss behavior, suggesting dielectric relaxation. The maximum hopping frequency has found to be of the order of 153 Hz. The low value of hopping frequency has been attributed to the scarcity of hopping sites in the polymer film due to poor π-conjugation. The lack of peak in electric modulus M′ and M′′ in the investigated frequency range is indicative of long range conduction in the low frequency domain. The Nyquist plot indicated that significant contribution to the film impedance was from the grain boundaries. The equivalent circuit developed from the simulation of phase of admittance curve indicated two R-C circuits with different time constants corresponding to contribution of grains and grain boundaries. At high frequencies the capacitive element exhibited its dominance by offering low impedance path, causing a clear spur in the phase curve.

Acknowledgement

One of the authors (Sameer Kalia) is thankful to University Grants Commission, New Delhi, for funding this research work (Reference Number 2015/TF/105) granting leave under its Faculty Development Program to carry out this research work and

Compliance with Ethical Standards

Conflict of Interest The authors declare that they have no conflict of interest.

References

1. S. Günes, H. Neugebauer and N. S. Sariciftci, Chemical Reviews **107** (4), 1324-1338 (2007).
2. Z. Zuo and Y. Li, Polymer Bulletin **68** (5), 1425-1467 (2012).
3. M. Shi, L. Fu, X. Hu, L. Zuo, D. Deng, J. Chen and H. Chen, Polymer Bulletin **68** (7), 1867-1877 (2012).
4. W. Liu, L. Qiu, W. Tang, L. Jiang, H. Peng, G. Chen, X. Xiao and Y. Zou, Polymer Bulletin **73** (2), 385-398 (2016).
5. Z. Al-Busaidi, C. Pearson, C. Groves and M. C. Petty, Solar Energy Materials and Solar Cells **160**, 101-106 (2017).
6. G. A. Buxton and N. Clarke, Physical Review B **74** (8), 085207 (2006).
7. S. J. Cho, W. T. Kim, Y. G. Ki, S. I. Kwon, S. Lee, S. Lim, J. S. Jang, B. H. Kwon and D. W. Kim, in *World Congress on Medical Physics and Biomedical Engineering 2006: August 27 – September 1, 2006 COEX Seoul, Korea "Imaging the Future Medicine"*, edited by R. Magjarevic and J. H. Nagel (Springer Berlin Heidelberg, Berlin, Heidelberg, 2007), pp. 1871-1872.
8. A. Mostaar, B. Hashemi, M. H. Zahmatkesh, S. M. R. Aghamiri and S. R. Mahdavi, in *World Congress on Medical Physics and Biomedical Engineering, September 7 - 12, 2009, Munich, Germany: Vol. 25/3 Radiation Protection and Dosimetry, Biological Effects of Radiation*, edited by O. Dössel and W. C. Schlegel (Springer Berlin Heidelberg, Berlin, Heidelberg, 2009), pp. 284-287.

9. M. El-Shahawy, A. Hussein and A. Tawansi, Journal of Materials Science **27** (24), 6605-6608 (1992).
10. P. C. Kalsi and C. Agarwal, Journal of Materials Science **43** (8), 2865-2868 (2008).
11. S. Chizu, T. Yoshiaki, Y. Takeshi, K. Makoto and D. Shuji, Science and Technology of Advanced Materials **15** (3), 034203 (2014).
12. Y. Xu, F. Zhang and X. Feng, Small **7** (10), 1338-1360 (2011).
13. H. Hrichi, K. Hriz, N. Jaballah, R. B. Chaâbane, O. Simonetti and M. Majdoub, Journal of Polymer Research **20** (9), 241 (2013).
14. A. A. A. Mascarenhas, R. V. Kolekar, P. C. Kalsi, A. Ramaswami, V. B. Joshi, S. G. Tilve and V. S. Nadkarni, Radiation Measurements **41** (1), 23-30 (2006).
15. V. Chavan, P. C. Kalsi and A. Mhatre, Journal of Radioanalytical and Nuclear Chemistry **287** (1), 273-276 (2011).
16. A. Goswami and A. P. Goswami, Thin Solid Films **16** (2), 175-185 (1973).
17. N. D. Nguyen, M. Schmeits and H. P. Loebl, Physical Review B **75** (7), 075307 (2007).
18. G. Jarosz and R. Signerski, Opto-Electronics Review **19** (4), 474 (2011).
19. K. K. Tsung and S. K. So, Journal of Applied Physics **106** (8), 083710 (2009).
20. D. C. Tripathi, A. K. Tripathi and Y. N. Mohapatra, Applied Physics Letters **98** (3), 033304 (2011).
21. S. Kalia, A. Mahajan, Neerja, A. K. Sharma, S. Kumar and R. K. Bedi, AIP Conference Proceedings **1728** (1), 020277 (2016).
22. M. Singh, A. Mahajan, R. K. Bedi and D. K. Aswal, Electronic Materials Letters **9** (1), 101-106 (2013).
23. M. Singh, A. Mahajan, N. Gupta and R. K. Bedi, Electronic Materials Letters **11** (1), 118-126 (2015).
24. P. Stallinga, in *Electrical Characterization of Organic Electronic Materials and Devices* (John Wiley & Sons, Ltd, 2009), pp. 45-64.
25. A. K. Jonscher, Journal of Molecular Liquids **86** (1–3), 259-268 (2000).
26. A. K. Jonscher, Nature **267** (5613), 673-679 (1977).
27. C. Groves, Reports on Progress in Physics **80** (2), 026502 (2017).
28. D. Chérif, B.-G. Maha, V. Francis, C. Rafik Ben, D. Joel and O. Hafedh Ben, Semiconductor Science and Technology **24** (10), 105007 (2009).
29. H. Yokoyama, E. J. Kramer, M. H. Rafailovich, J. Sokolov and S. A. Schwarz, Macromolecules **31** (25), 8826-8830 (1998).
30. H. Sirringhaus, N. Tessler and R. H. Friend, Science **280** (5370), 1741-1744 (1998).
31. W.-J. Chi, P.-P. Sun and Z.-S. Li, Physical Chemistry Chemical Physics **18** (39), 27073-27077 (2016).
32. A. Molak, M. Paluch, S. Pawlus, J. Klimontko, Z. Ujma and I. Gruszka, Journal of Physics D: Applied Physics **38** (9), 1450 (2005).

Paper-20

Induced Transient Current Measurements and Characteristics of Transducer by Squeezing Piezoelectric Substances

Abullais Nehal Ahmed
Dept. of Physics, J.A.T. Arts, Science and Commerce College (For Women),
Malegaon, Dist. Nashik, Maharashtra, India.

Abstract:

A transducer is an electrical device that is used to convert one form of energy into another form. There are various types of transducer like capacitive, inductive, and resistive and pressure transducer etc. Piezoelectric material is an example of pressure transducer. In which when we apply pressure on sides of crystal it will sense this mechanical energy and convert into electrical work. There are various applications of piezoelectric material for example piezo-accelerometer, energy harvesting, gas lighters, general quartz clock, buzzers etc.

Out of many piezoelectric crystals, using wet chemical method we synthesized sodium potassium tartarate or Rochelle salt (1). In chemical synthesis, we used many chemical compounds like potassium bitartarate, washing soda, sodium chloride, potassium bromide. By using these chemicals numbers of samples of Rochelle salt were successfully prepared. It shows millivolt when measured by digital multimeter.

The compound shows there is linear relationship between variation in physical quantities and generated electrical signal (i.e. variation in input and output). The piezoelectric transducer shows wide operating range so that it can be used for wide range of operation. The relationship between input and output for a transducer shows predictable over a long period of time. This ensures reliability of operation. The speed of response is directly depends on the measuring quantity, relative to the input.

Kewords: *piezoelectric crystals, accelerometer, multimeter, crystalline state, transducers etc.*

Introduction:

Potassium bitartrate is a colourless crystalline or white powdery solid with a pleasant, slightly acidic taste (1,2). The compound is a by-product of the fermentation of grape juice and, as such, may have been known to humans for as long as seven thousand years. An article in the different journal (3) reported some years ago that traces of the calcium salt of tartaric

acid, a cousin of potassium bitartrate, was found in remnants of a pottery jar in northern Iran dating to about 7,000 bce. Potassium bitartrate was used by ancient people in a wide range of household uses, from cooking and baking to cleaning. The true chemical nature of the substance long known as cream of tartar was determined in 1770 by the Swedish chemist Karl Wilhelm Scheele.

How it is made? Potassium bitartrate is made today by the process that has been used for centuries. Wine lees are treated with hot water, which dissolves the potassium bitartrate. The hot solution is then allowed to evaporate. As potassium bitartrate crystals form, they are removed and purified.

Common uses and Potential Hazards: The primary use of potassium bitartrate is in commercial food production and household cooking and baking. The compound is added to foods to stabilize egg whites after they have been beaten, to add body to a product, and to produce creamier textures for sugar-based foods. A small amount of potassium bitartrate also adds a pleasantly acidic taste to foods. The compound is found most commonly in baked goods, candies, crackers, confections, gelatines, puddings, jams and jellies, soft drinks, margarines, and frostings (2, 3). Some of the functions that potassium bitartrate performs in foods include:

- It acts as a leavening agent, causing a product to rise, in baked goods.
- It serves as an anticaking agent and stabilizer to thicken some food products.
- It prevents the crystallization of sugars when making candy and sugary syrups.
- It hides the harsh aftertaste and intensifies the flavours of some foods.
- It improves the colour of vegetables that have been boiled during preparation.

Chemical Reactions (KBr):

White melts without decomposition, it readily soluble in water (without hydrolysis), also it does not form crystalline hydrates, therefore is not soluble in concentrated hydrobromic acid. Typical reducing agent is

$2K + E_2 = 2KE$ (normal temperature : E = F , Cl , Br , I).

$2KI + E_2 = 2KE + I_2\downarrow$ (E = Cl , Br).

$2KBrO_3 = 2KBr + 3O_2$ (temperature > 434°C).

Chemical reactions with potassium bromide KBr:

KBr*(diluted)* $+ 6H_2O = [K(H_2O)_6] + Br^-$ (pH=7).

$2KBr$*(solid)* $+ H_2SO_4$*(10-50%conc., cold)* $= K_2SO_4 + 2HBr$

$2KBr$*(solid)* $+ 3H_2SO_4$*(conc.>50% , hot)* $= 2KHSO_4 + Br_2\uparrow + SO_2\uparrow + 2H_2O$

$2KBr + Cl_2 = 2KCl + Br_2\uparrow$*(boiling)*

$5KBr + 3H_2SO_4$*(diluted)* $+ KBrO_3 = 3Br_2 + 3K_2SO_4 + 3H_2O$

$2KBr + 2H_2SO_4$*(conc.)* $+ MnO_2 = Br_2 + K_2SO_4 + MnSO_4 + 2H_2O$*(boiling)*

$KBr + 3H_2O$*(hot)* $\rightarrow$ *Electrolysis* $\rightarrow$ $3H_2\uparrow$*(cathode)* $+ KBrO_3$*(anode)*

Similar reactions can be obtained with Sodium Chloride NaCl.

Synthesis of Pure Rochelle Salt:

For synthesis of pure Rochelle salt (4,5,6) or Sodium Potassium Tartarate, following chemical reaction occurred while preparing the substance or compounds.

- Cream of tartar (Potassium bitartarate),
- Washing soda (Sodium Carbonate),
- Tap water.

60ml water + 50grams cream of tartar + 50grams washing soda

$2C_4H_5KO_6 + Na_2CO_3 = 2KNaC_4H_4O_6 + CO_2 + H_2O$

2 cream of tartar + washing soda = 2 Rochelle salt + CO_2 + H_2O

Synthesis of Pure Rochelle Salt with KBr:

Further improving the induced electrical current within the substance or sensitivity of the piezoelectric material, we added potassium bromide in the synthesised of pure Rochelle salt (4,5,6) or Sodium Potassium Tartarate, following chemical reaction occurred while preparing the substance or compounds.

$2C_4H_5KO_6 + Na_2CO_3 + 2KBr = 2K_2NaC_4H_4O_6Br + CO_2 + H_2O$

2 cream of tartar + washing soda + 2 potassium bromide =2 Rochelle salt + CO_2 + H_2O

Synthesis of Pure Rochelle Salt with NaCl:

For improving the induced electrical current within the substance or sensitivity of the piezoelectric material, we added sodium chloride in the synthesised of pure Rochelle salt (4,5,6) or Sodium Potassium Tartarate, following chemical reaction occurred while preparing the substance or compounds.

$2C_4H_5KO_6 + Na_2CO_3 + 2NaCl = 2KNa_2C_4H_4O_6Cl + CO_2 + H_2O$

2 cream of tartar + washing soda + 2 sodium chloride = 2 Rochelle salt + CO_2 + H_2O

Experimental Details:

Sample-1: In 60ml water, we added 50grams cream of tartar and 50grams washing soda. In the preparation of crystal, addition of both chemicals shouldn't do simultaneously. After one hour when crystals start growing on the walls transfer contents (compound crystal) in metal container. In order to shape the crystal choose for example small circular shaped metal

container and place it in refrigerator for 12 to 15 hours, then take it out from refrigerator. Keep the temperature of the refrigerator 0 to 5^{o}C. Remove the crystal from the container and then keep it in between the electrodes that are connected to the digital multimeter. Apply or release the pressure on piezoelectric transducer. It shows 16.6mV readings in digital multimeter.

Sample-2: In 10ml water, we added 10grams cream of tartar, 2grams washing soda and 2grams of KBr. In the preparation of crystal, addition of both chemicals shouldn't do simultaneously. After place the container in refrigerator for 12 to 15 hours. Keep the temperature of the refrigerator 0 to 5^{o}C. Remove the crystal from the container and then keep it in between the electrodes that are connected to the digital multimeter. Apply or release the pressure on piezoelectric transducer. It shows 32mV readings in digital multimeter.

Sample-3: In 50ml water, we added 45grams cream of tartar, 30grams washing soda and 5grams NaCl. Once the synthesis completed and crystal is formed, put it in between the electrodes that are connected to the digital multimeter. Apply or release the pressure on piezoelectric transducer. It shows 45mV readings in digital multimeter.

Fig.(a)
Sample-1 (pure)

Fig.(b)
Sample-2 (with KBr)

Fig.(c)
Sample-3 (with NaCl)

Fig.: Sodium Potassium Tartarate Crystal, (Or E337; Seignette's salt; Rochelle salt.)

Results and Conclusions:

Thus from above experiments we say that the piezoelectric effect relates a shape change with voltage. If a voltage is applied to the non-polarized material a shape change occurs as the molecule reorganize to align in the electric field. This is known as electrostriction. Conversely, an electrical field is generated if mechanical force is applied to the material to change its shape. This is the piezoelectric effect. The piezoelectric effect was observed by conducting a number of experiments using Sodium Potassium Tartarate Crystal (7). The piezoelectric materials exhibit two crystalline forms, one form is ordered and this relates to the polarization of the molecule, and second form is disordered relates to the non-polarization of molecule. The polarization of molecules occurs in the crystal due to the compressive force and due to the force the molecules align induces voltage across the synthesized crystal as shown in above figure.

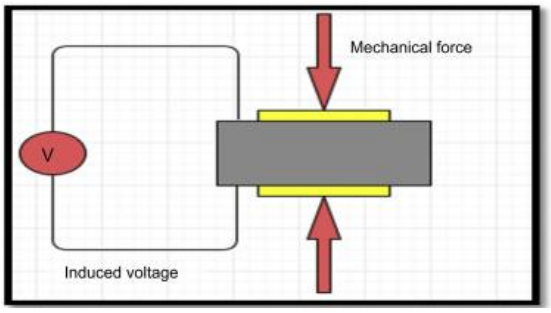

Similarly de-polarization of a molecules occurs in the crystal after releasing the compressive force and due to this the molecules dislocate induces voltage across the synthesizes (8) crystal were observed.

Piezoelectric materials are materials that produce a voltage when stress is applied. Since this effect also applies in the reverse manner, a voltage across the sample will produce stress within the sample as shown in figure were observed.

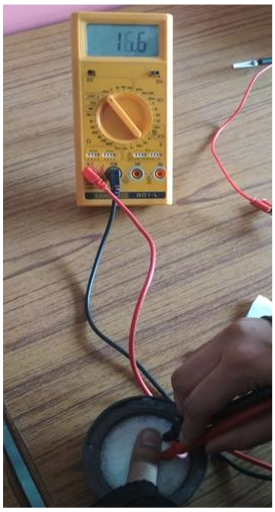

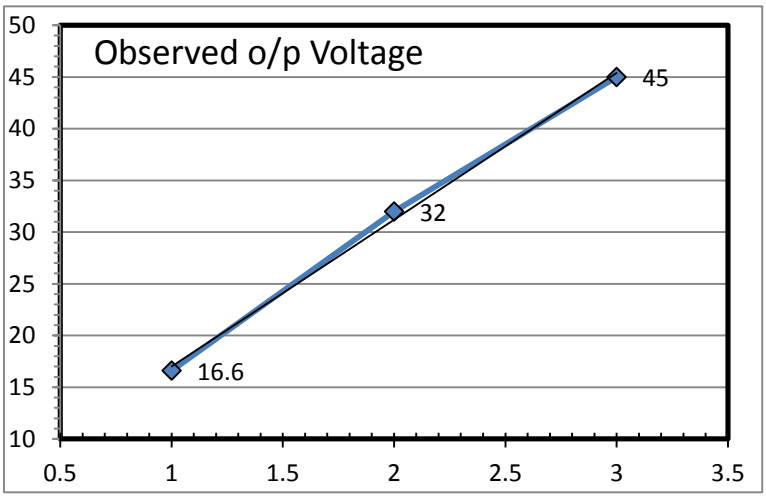

Uses and Applications:

- Potassium bitartrate can be used as a laxative for both humans and domestic animals.
- It is used in the processing of some metals, giving a coloured tinge to the final product.
- The compound is also an ingredient in products used to clean brass, copper, aluminium, and other metals.
- It is used in the chemical industry as a raw material for the preparation of other tartrate compounds.
- There are no known health hazards for potassium bitartrate except for the general overall caution given in the introduction that all chemicals in some concentrations can pose a hazard.
- Potassium bitartrate is thought to be one of the safest chemical compounds.

Reference:

1) Brewster, David, "Observations of the pyro-electricity of minerals". The Edinburgh Journal of Science. 1: 208–215
2) M.L. Wang, J.P. Lynch and H. Sohn, Eco-friendly materials for large area piezoelectronics: self-oriented Rochelle salt in wood, E Lemaire, C Ayela and A Atli, Sensor Technologies for Civil Infrastructures, Volume 1: Sensing Hardware and Data Collection Methods for Performance Assessment, Volume 55 in Woodhead Publishing Series in Electronic and Optical Materials, Edited by: Published 10 January 2018.
3) Lemaire E. et. al., Smart Materials and Structures, IOP Publishing Ltd., Smart Mater. Struct., Volume 27, Number 2 Citation 2018.
4) DOI: 10.13140/2.1.4242.0168, Piezoelectric Effect in Rochelle Salt, June 2011,
5) "SP-401 Skylab, Classroom in Space", "Rochelle Salt applications", NASA Retrieved 2009-06-06.
6) Lemaire, E., Ayela, C., Atli, A., Ferroelectrics-Physical Effects, Eco-friendly materials for large area piezo-electronics: self-oriented Rochelle salt in wood Show affiliations, Publication: Smart Materials and Structures, Volume 27, Issue 2, article id. 025005 (2018). Pub Date: February 2018, DOI: 10.1088/1361-665X/aaa209,
7) David R. Lide, ed. (2010), CRC Handbook of Chemistry and Physics (90th ed.), CRC Press, page number 4–83.
8) Fieser L. F., Fieser, M., Reagents for Organic Synthesis; Vol.-1, Wiley: New York - 1967, page number 983.